Digitized Theses

Digitized Special Collections

2009

NUMERICAL SIMULATION OF AERODYNAMIC AND ELECTROSTATIC EFFECTS IN A POWDER COATING FLUIDIZED SYSTEM

Mario Alberto Nunez
Western University

Follow this and additional works at: https://ir.lib.uwo.ca/digitizedtheses

NUMERICAL SIMULATION OF AERODYNAMIC AND ELECTROSTATIC EFFECTS IN A POWDER COATING FLUIDIZED SYSTEM

(Spine title: Numerical Simulation of a Powder Coating Fluidized System)

(Thesis format: Monograph)

by

Mario Alberto Nunez

Graduate Program in

Engineering Science

Department of Electrical and Computer Engineering

A thesis submitted in partial fulfillment

of the requirements for the degree of

Master of Engineering Science

The School of Graduate and Postdoctoral Studies

The University of Western Ontario

London, Ontario, Canada

Abstract

The work described in this thesis was carried out for a better understanding of the phenomena in an electrostatic fluidized bed for powder coating. The publications in different areas of science (Computer Science, Chemical Engineering and Electrical Engineering) have been of great help to obtain a final written computer code that combines novel computational methods which aim at simulating the physical effects that occur in any electrostatic fluidized system.

One of the main purposes of existing industrial fluidized beds is the coating of metallic pieces. The process to achieve this includes using insulating powder of a particle size appropriate for fluidization. The metallic piece to be coated has to be pre-heated substantially above the melting point of the powder coating material in order to obtain enough enthalpy to cure the required mass of coating insulation. Once this appropriate temperature is reached, the piece is dipped in the fluidized bed for the length of time necessary to acquire a uniform coating. This way of coating in industrial fluidized beds is very inefficient since energy is spent pre-heating the metallic piece and because usually once the dipped piece has been coated, it is placed in an oven again for a new heating period, to finally obtain a uniform surface coating. All these procedures involve substantial increases in energy costs.

A new method to obtain uniform powder coated pieces with minimal energy costs was thought of. This idea implies the electrification of the insulating powder particles. In this case if a cold metallic electrically connected to ground piece is dipped in a fluidized bed,

the electric field generated by the space charge in the bed will propel the charged particles towards the piece to be coated and remain attached to it. Once taken out of the fluidized bed, the charged particles remain attached (due to the Coulomb attraction force) while the piece is taken to the oven for curing.

In 2004, experiments were carried out at the Applied Electrostatic Research Centre (A.E.R.C.) at the University of Western Ontario. An experimental fluidized bed with powder particles was used which included a suction pump system. Through this suction system fluidized powder particles were sucked from the system, and forced to travel around a Teflon tube. Due to the difference of work functions the particles acquired a high positive charge. Furthermore, the particles were injected back into the system, increasing the total net charge of the system. Thus, so when a metallic electrically earthed piece was dipped, due to the Coulomb attraction forces between the charged powder particles in the system and the electrically earthed piece a good surface coating would be obtained. Results from these experiments showed that during injection the total net charge of the system increased for a certain period of time and then gradually decreased. It was concluded that the electrification (injection of highly positive charged particles) of the bed powder had to be carried out only during the time that the piece to be coated was dipped in the bed; otherwise a good coating was not possible. These unexplained findings are the basis for this thesis.

In this project, a numerical complex simulation of a fluidized system was performed, for a system with three different size particles (60 μm, 80 μm and 100 μm). Throughout this thesis snapshots of these particles' positions are shown to better visualize their trajectory

paths. After a certain period of time the system acquired a total net charge due to the tribocharging process, at this point a new set of highly positively charged particles (120 μm) was injected. It was expected that the total net charge of the system increases accordingly to the total charge of these new injected particles, however, the total net charge increased up to a certain level and then it seemed to fade away as first stated by the results of the A.E.R.C.'s experiments.

The simulations performed in this work tried to reproduce the conditions set in the experiments done in the A.E.R.C. (2004). One of the main achievements was the visualization of the trajectories of all the particles in the system. Appendix 1 presents snapshots of this visualization. Additionally, Chapter 6 shows other insightful results.

As mentioned earlier, one of the main objectives of this thesis was to find out why the most efficient coating occurred only when the metallic piece and the positive charged particles were dipped and injected simultaneously. Analyzing the video and graphs obtained the conclusion was that if the injection of charged particles had been done prior to the dipping of the metallic piece, part of the total net charge would have gradually discharged into the electrically earthed walls. Therefore, by the time the earthed metallic piece was dipped the total net charge of the system was not going to be as high as expected which consequently would have ended up in a poor coating.

Acknowledgments

I especially wish to thank Professor I. I. Inculet, my chief advisor, for his inspiration and guidance throughout this project. I would also like to my express my deepest gratitude to my co-supervisor Professor Colin Denniston for his excellent advice and discussions during this whole project.

I am grateful and would also like to acknowledge the other members of the research team; Dr. Maurice A. Bergogougnou and Dr. Kaz Adamiak for their contribution on my behalf.

I appreciate the cooperation and assistance received from various people at this Engineering School; faculty members, technicians, librarians, secretary office workers and custodians.

I am indebted to my beloved Crystal for her many hours spent giving me support and motivation.

Finalmente a mis papás Esperanza y Jorge que a pesar del tiempo y la distancia nunca me dejaron solo, y la aurora de su compañía siempre me abrazo. También un agradecimiento especial a mis incondicionales amigos Pablo, Abe y Bayron, los cuales con sus diferentes formas de ver las cosas me dieron los matices necesarios para dibujarme cada día, gracias por todo.

Table of Contents

List of Figures

List of Tables

Nomenclature

F_d	drag force, newton
F_g	gravitational force, newton
F_e	electrical force, newton
Q	electrical charge, coulomb
$\bar{E}$	electric field intensity, volt/meter
V	electric potential, volt
A	surface area, $meter^2$
ρ	charge density, $coulomb/meter^3$
$\emptyset$	work function, electron volt
ε_0	permittivity of free space, $coulomb^2/(newton - meter^2)$
ms	time, milisecond
μs	time, microsecond
mm	space, millimeter
μm	space, micrometer
ng	mass, nanogram

Chapter 1

Introduction and Objectives

1.1 General Background Information

Electrostatic powder coating is a technique that increases the effectiveness of the coating process compared to conventional methods. The fundamentals of this procedure are based on the use of electrically charged powder particles to cover an electrically earthed piece, thus taking advantage of the Coulomb attraction forces to increase the coating efficiency.

One of the basic methods of electrical charging is by friction and contact (tribocharging or tribo-electrification). When two materials surfaces are contacted there is an electronic charge transfer from one surface to the other, the material with the smaller work function will acquire a positive charge, on the other hand the material with the higher work function will acquire a negative charge. The work function could be dictated by the composition, size, and surface area, among other parameters of a material. When tribocharging is used in a powder coating process, the whole process is called tribo powder coating.

The electric field generated by the space charge in the fluidized bed will propel the charged particles towards the piece to be coated and remain attached to the piece forming a gradually increasing layer of coating. It is simple to notice that by increasing the space charge of the fluidized system, the Coulomb attraction force between the particles and metallic piece will increase too, this will lead to a more uniform and smoother coating.

This was the idea behind experiments done in the past in the Applied Electrostatic Research Center (A.E.R.C.) at The University of Western Ontario [71]. In these experiments, additional particles were highly charged prior to injection and then injected into the fluidized bed. It was thought that by doing this, the total net charge of the system would dramatically increase, thereby causing an increase in the electric field. The results obtained were inconsistent and for some unknown reason the total net charge of the system did not increase as expected.

1.2 Objectives

The objectives of this thesis are:

- Create a computer simulation of a fluidized process under the conditions of the A.E.R.C. experiments [71].

- Characterize the behavior of a bipolar charged powder inside a fluidized bed.

- Investigate the possible explanations of why the total net charge did not increase as expected and possible solutions to the problem.

- Compare to results obtained in past experiments done in the A.E.R.C. and suggest some ways to solve the problem.

This thesis is organized in such a way that in Chapter 2 we survey the literature relevant to our problem. Chapter 3 to Chapter 5 describes the simulations developed to solve the problem. Finally, chapter 6 contains the results and conclusions.

Chapter 2

Literature Review

This chapter will review pertinent literature on how contact and friction in particulate flow can cause the electrostatic charging of particles in nature. Additionally, a brief overview of the bipolarity of charges in fluidized systems is presented, and finally an introduction on computer simulation will be addressed.

2.1 Electrostatic Charging In Nature

Electrostatic charging in nature has been observed since ancient times and was attributed to super natural causes. In the last two centuries, due to the rapid advance in science, these once thought mystical events have been demystified.

Electrical sand storms, a scenario where harsh winds and sand happen to coexist in open spaces (mostly in deserts), are one of nature's amazing phenomenon. The pioneers of these studies [1] [2] [3] [4] realized that electric forces within the sand storms were very influential in the trajectories of sand particles. Schmidt et al. [5] observed that the electric field generated under moderated wind conditions was 160 kV/m. They also estimated that under moderate wind conditions the electrostatic force was equivalent in magnitude to the gravitational force.

The measurement of bulk electrical properties in a sand storm has been investigated by Freier [6] and Leach [7]. Iversen [8] simulated a snow drift in a wind tunnel using sand

and glass spheres. During this experiment he observed that cornices were formed in the intermediate downstream end of a drift, which he attributed to electrostatic forces that were formed due to tribo-electrification.

Also on the Martian surface it was determined that tribo-electrification has to be considered in future NASA explorations, since the effects can be harmful for different electronic equipment [9].

Another phenomenon in Nature that provokes great admiration is lightning that occurs in volcanic plumes. A volcanic eruption comes along with lightning and other electrical phenomena. Volcanic eruptions are comprised of fragments of solid material, normally disintegrated fragments of Silicate rock, in various forms and shapes, including crystals, glassy shards, and vesicular particles in a wide range of sizes. They also come accompanied by volcanic gases such as: CO_2, SO_2, N_2, H_2S, CO among others, and by droplets of condensed gases and water vapor [10]. One of the main reasons why electric charge builds up in those particles is particle-particle interaction within the plume (tribo-electrification).

2.2 Tribo-Electrification of Solids

When a multi-body solid system is fluidized, it can be understood that particles will collide with each other. These collisions inevitably lead to tribo-electrification of particles due to the continual cycle of contact and separation. In order to better understand this event, the theory of electron energies in materials must be first reviewed.

It is known, based on band structure theory that a specific material is only able to conduct if the outer electrons lie in a valence band that is partially empty. The highest filled energy level is called the Fermi Level and the energy required to move an electron from the top of the energy distribution to infinity is called the work function. In an insulator the valence band is filled and a wide energy gap lies above the valence band therefore it is unlikely that conduction will take place. However, impurity atoms in an insulator will provoke additional energy levels that may produce a small number of charge carriers.

Cutting a crystal to create a surface primarily requires breaking bonds thus creating so-called dangling bands which attract impurities. These electron energy levels associated with impurities are called surface states and exist at the surface of the particles. This is important with reference to powders because many of them are produced by a grinding process, which leads to a mix of impurities at the ground surface.

In this work two materials were considered in the fluidized system, electrically earthed metal walls (stainless steel), and insulating particles (polymers). Due to the collisions between particle-particle and particle-wall, a brief explanation of the different kinds of contacts has to be made. The following sub-sections offer a broad explanation of the events happening during these collisions.

2.2.1 Insulator - Metal Contact

The charge acquired by an insulator in contact with a metal exclusively depends on the nature of the insulator and the work function of the metal. For most of the organic

polymers, which are more frequently studied, the charge density obtained is normally in the range of 10^{-5} to 10^{-3} C/m^2 [11]. As it was said, contact electrification may be caused by very small concentration of impurities or surface defects.

The amount of charge transfer is independent of the time of contact [11] [12]. An increase in charge transfer with an increase of time can be attributed to an increase in area of contact.

For most insulators the charge density after contact with a metal is proportional to the metal work function [11] [12] [13]. Since the contact charge on the insulator depends on the metal work function, it is quite likely that the charge transfer is by electrons rather than surface ions [14]. This allows for an effective work function to be calculated for polymers [13] as shown in Table 2.1 (Davies, 1969 and Strella, 1970).

For an insulator the electron energies are a function of position, surface impurities, local atomic structure, and chemical nature of the material. Therefore the work function for an insulator is only an experimental quantity with no fundamental standard value from sample to sample [13].

2.2.2 Insulator - Insulator Contact

When two insulating particles come into close contact a charge transfer occurs between them. If the particles are made of different insulating material, using the convention that electrons pass from the insulator with the lower work function to the insulator with the

Table 2.1 Table of Work Function for Plastics Composed of Different Polymers [13]
(Taken from "Elect. principles, problems and applications", By J.A. Cross, p. 29, (1987))

Polymer Work Functions		
Work function (eV)		
Material	**Davies (1969)**	**Strella (1970)**
- PVC	4.85 0.20	
Polyimide	4.36 0.06	
Polycarbonate	4.26 0.13	4.80
PTFE	4.26 0.05	5.75
PET	4.25 0.10	
Polystyrene	4.22 0.07	
+ Nylon 66	4.08 0.06	4.30-4.54
- Teflon		5.75
Polychlorotrifluoethylene		5.30
Polychlorinated propylene		5.14
PVC		5.13
Polychlorinated ether		5.11
Poly-4-chlorostyrene		5.11
Poly-4-chloro-4-methoxy-styrene		5.02
Polysulphone		4.95
Polyepichlorohydrin		4.95
Polystyrene		4.90
Polyethylene		4.90
Polycarbonate		4.80
Polyethylene-vinyl acetate		4.79
Polymethylmethacrylate		4.68
Polyvinylacetate		4.38
Polyvinylbutyral		4.30
Ply-2-vinylpyridine-styrene		4.27
Nylon 66		4.30-4.54
+ Polyethylene oxide		3.95-4.50

higher work function, the amount and the sign of the transferred charge may be determined. Figure 2.1 demonstrates this case scenario.

From Figure 2.1 it can be observed that there are two density limits; one limit assumes a low density of surface states and the other limit assumes a high density of surface states. In the case of the low density limit, charge is exchanged from the material with the lower work function to the material with the higher work function. This happens until the work functions of both materials equilibrate at a common level. In the high density limit case the charge exchange increases the energy of the states of the material with the higher work function to that of the material with the lower work function so the effective Fermi levels of each are equal.

Now when the particles are made of similar materials, for example in the flow of sand in sand storms, tribo-electrification [15] [16] [17] is still produced. The charging of similar material particles was also observed in fluidized beds [18].

Tribocharging between similar materials is not well understood. The effect of two similar material particles colliding seems to produce a driving force for an electron transfer. Experiments have shown that when particles of similar material are fluidized, a bipolar charging occurs such that larger particles charge positively, smaller particles charge negatively [25] [26] [27] [28] [29] [30]. Additionally, tribocharging has a larger magnitude when the particle size distribution of the system has wide limits [31] [32].

At first glance, similar insulating materials may seem to have the same work function due to their similarity in composition. But most of the times insulators are not crystalline amorphous solids. Also, since two particles of the same material are not geometrically the same the work function between them will vary. If particles are analyzed from a microscopic level, we may find different properties from particle to particle, so no particle is exactly similar to any other. Changes in a particles' radius, on the number of surface impurities, the superficial shape of the particle, and many other details that at this point may not be known, will output the real work function for every single particle.

Schein et al. [33] [34] [35] derived the predicted charge to mass for insulator-insulator contacts from generalized results for metal-insulator contacts. It is important to note that the prediction of the charging on the basis of work function differences of the materials in contact could not explain the experimental findings that very fine particles charge negatively regardless of what material they have come in contact with [28].

2.3 Charge Bipolarity

Once tribocharging started being used in various industrial processes, more research was made to unfold all the details of this technique. By fundamental electron transfer theory it is thought that the only charge exchange is able to happen among dissimilar materials, but when similar particles are fluidized surprising results are obtained. The results show that there is a bipolarity of charge between similar materials. Ever since, different scientific investigations have proven a bipolarity of charge between similar materials' particles [25] [26] [27] [28] [29] [30], and also that tribo-electrification is larger in magnitude when
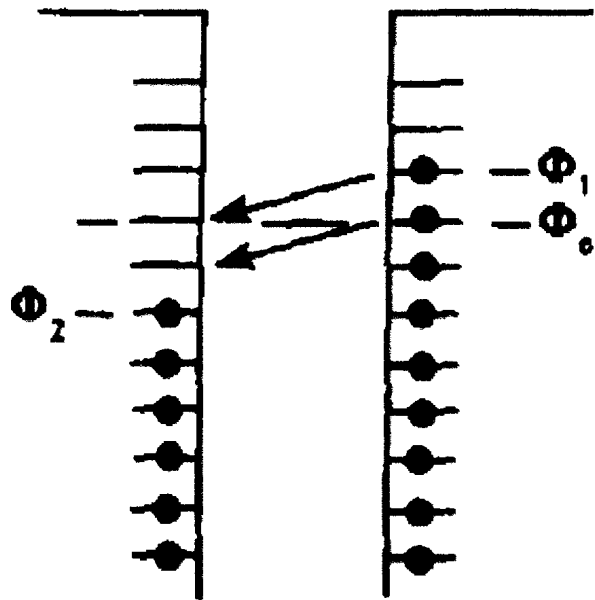
2.1a) Low Density Limit
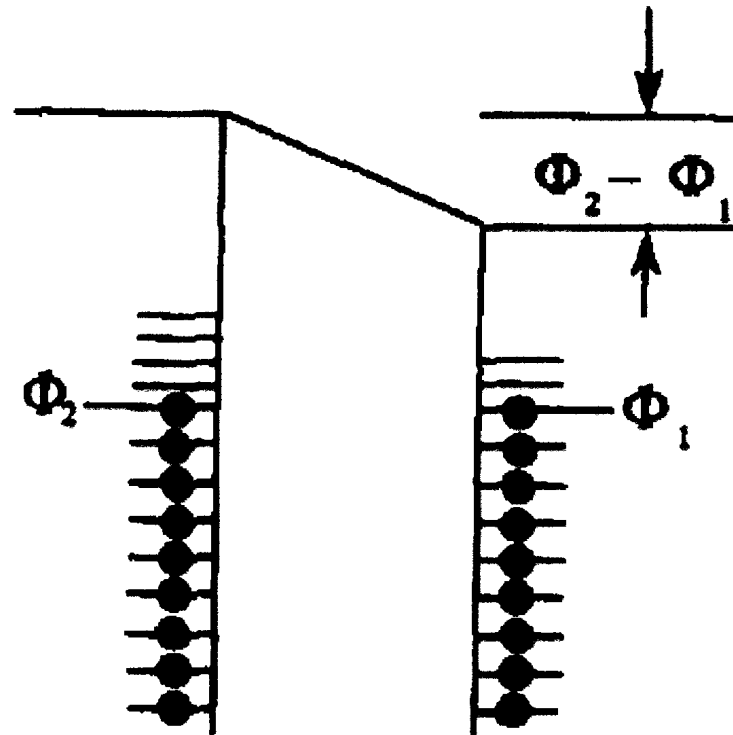
2.1b) High Density Limit

Figure 2.1 a) and 2.1 b) Schematic representation of the energy states for insulator-insulator contact charging. A dash represents a surface state, a dot indicates a filled surface state

Figure 2.1 Insulator - Insulator Contact Charging for Low and High Density Limits of Surface State Theory
(Taken from "Contact charging between insulators", By G.S.P. Castle, Journal of Electrostatics, Vol. 40&41, 1997, pg. 16)

the system has a broad particle size distribution [31] [32]. In the next paragraphs we will look at different experiments that were done to find out the polarity and net charge magnitudes of particles.

In the A.E.R.C., years of work were dedicated to this purpose [26] [28] [30]. Zhao and Inculet [28] built an innovative apparatus to measure particles' net charge. Since the total net charge of particles can change during handling, a sampling method was proposed to satisfactorily obtain the desired measurements without affecting the results. Figure 2.2 presents the specific device developed. A hollow round metallic tube was installed vertically through the center of the fluidized system and a series of holes were located in the tube's wall at different heights. Each hole was equipped with a plug, which could be opened or closed. While the holes were open, the powder sample entered the tube and dropped through the tube to the measurement device below. The device consists of a vertical array of Faraday pail sensors, which are used to measure the charge-to-mass ratio of the powder sample. An electrometer was connected to each Faraday pail, which measured the total net charge of each sample. After the charge reading was obtained the sample was weight to obtain the mass of the powder, hence the net charge-to-mass ratio of the given sample was able to be calculated and results of this experiment prove that bipolarity exists between similar powder particles.

Also in the past, pioneer numerical simulations were carried out and the outcomes of these simulations confirm this bipolarity between similar insulating particles [26]. In this simulation a model where any individual particle undergoes one collision per time interval was considered. The authors of this work [26] emphasized that the charge transfer
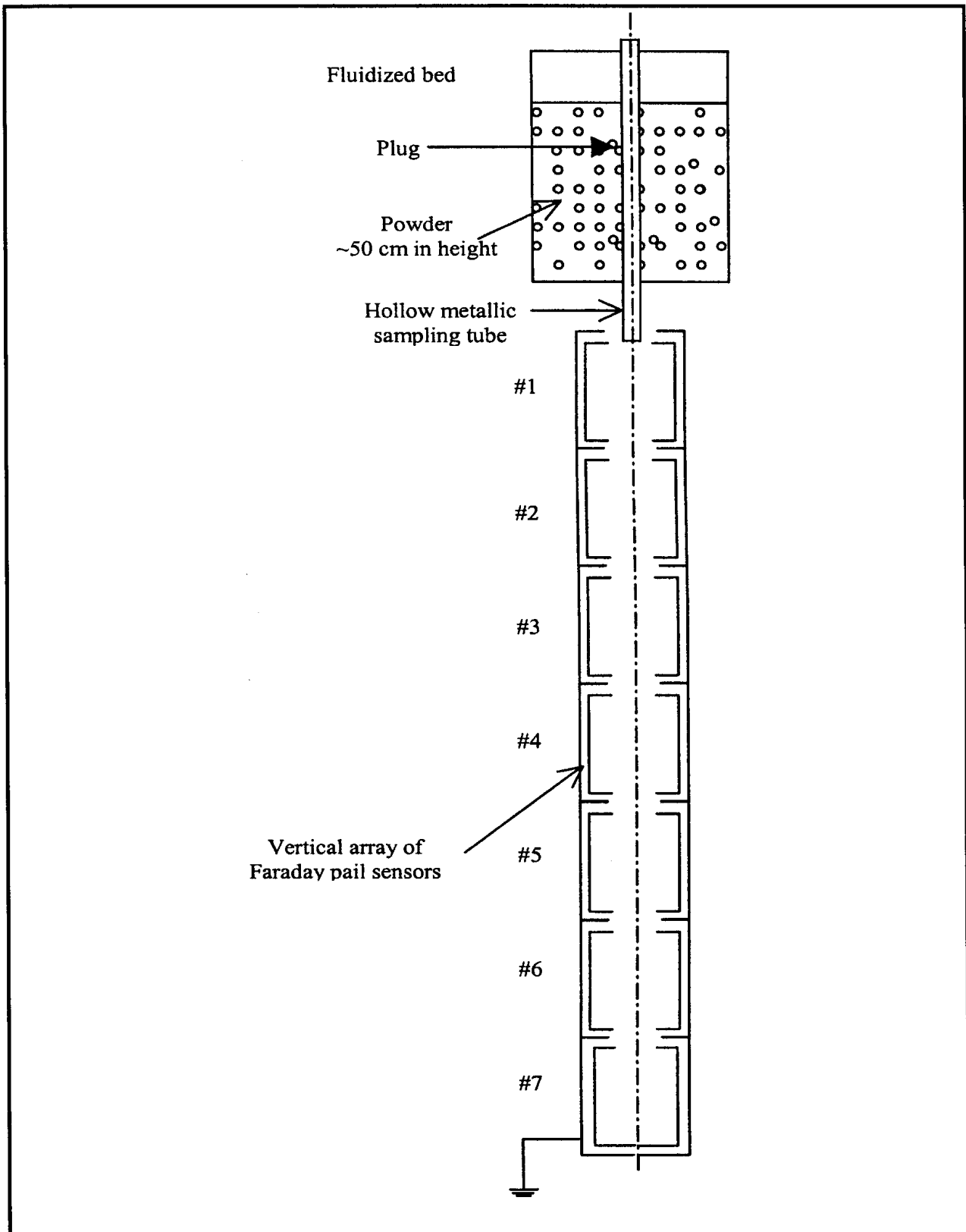
Figure 2.2 Device for Measuring Charge-to-Mass Ratio [28]
(Taken from "Bipolar charging in polydisperse polymer powders in industrial processes", By H. Zhao, G.S.P. Castle, I.I. Inculet, A.G. Bailey, IEEE Transactions Industrial Applications, vol. 39, issue 3, pp. 612-618, (2003))

depended on the work function of any insulating particle, and this work function value was directly proportional to the size of the particle. Computationally what the authors of this work did [26] was to equate the probability of collision between any two species of particles, so the average effect, in terms of charge, can then be obtained. No Aerodynamic or electrostatic effects on the trajectories of these particles was imposed during their simulations. This approach may not be the best option for this thesis since in the cases that the particles are larger than $1\mu m$ the work function variation is less than 0.01%, therefore, no noticeable variation on the charge per specie may be obtained. Table 2.3 shows the average charge per particle for 3 species of particles used in these computer simulations.

Table 2.2 Charge per Particle, 3 Different Sizes [26]
(Taken from "Charge exchange model of a disperse system of spherical powder particles", By F.S. Ali , I.I. Inculet, Journal of Electrostatics, vol. 45, p.139, (1998))

Radius (μm)	Average Charge per Particle (C)
20	-5.12E-13
40	-2.51E-13
60	+1.16E-12

Results obtained show that particles with a radius of 40 μm or less build, on average, a negative net charge and the particles with a radius of 60 μm build, on average, a positive net charge. Figure 2.3 graphs the outcomes of these simulations.

Another explanation of the reasons for this bipolarity between different size particles may be due to the manufacturing process of the different powders used in fluidized systems.
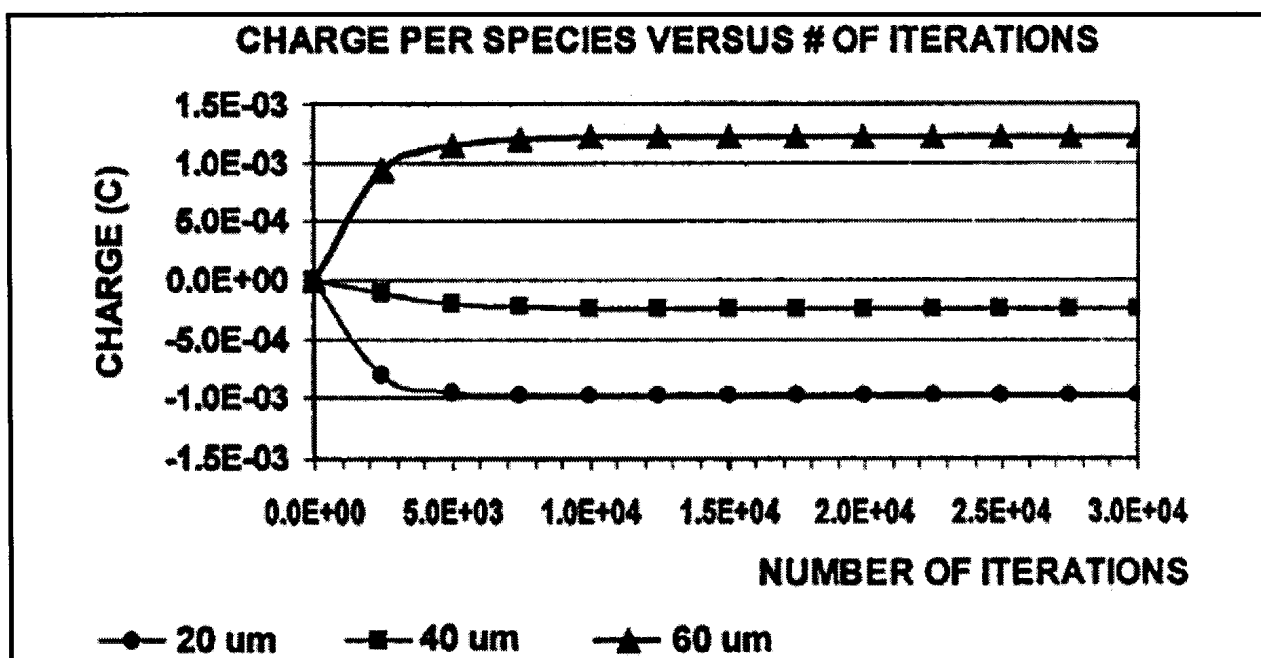
Figure 2.3 Simulation for three sizes of particles, results for each species charge [26]
(Taken from "Charge exchange model of a disperse system of spherical powder particles", By F.S. Ali , I.I. Inculet, Journal of Electrostatics, vol. 45, p.139, (1998))

The insulating particles used during fluidization are produced by the grinding of a bulk material to obtain the smaller size particles, the larger size particles are further ground thus the contact with the grinder is increased for smaller size particles. This may contribute to the small particles ending up with a rough/fractured surface. It has been shown that for similar crystalline materials the work function is proportional to the inverse of the surface roughness [36], thus rougher surfaces have a different work function compared to smoother surfaces. As explained above, a difference of work function propitiates electron transfer between particles. Up to our current scientific knowledge, all of these are just hypotheses, no exact reason to explain the bipolarity of charge has been accepted by the scientific community.

Another reasonable explanation that complements the idea of the previous paragraph was developed by Duff and Lacks [37], where they suggested that since particles have

different diameters, they will have different masses and speeds, since the average velocities vary inversely proportionally with the square root of the mass. Smaller particles move faster therefore undergoing more collisions, which in turn means more tribo-electrification due to this difference in work function. Smaller particles will gain more electrons acquiring a negative net charge, the opposite occurs with larger particles. Some other hypotheses of why this bipolarity may occur have been investigated by other authors [30] [34] [35]. Even though plenty of work has been done in this field, the reason why this bipolarity of charge among similar materials happens is still not well understood.

2.4 Computational Simulations

The development of digital computers and their application for solving scientific problems, has introduced what is called a "third methodology": computational simulations [38]. This is sometimes an alternative to the conventional ways to conduct research. In recent years computational simulations have had a deep impact in practically all fields of science [38] [39].

In physics, a computational simulation was introduced as a tool to reproduce a multi-body system in the early 50's, with the pioneering work of Metropolis et al. [40]. Later, results were obtained satisfactorily in the area of statistical classical mechanics, in particular with liquid simulations. These results gave credibility to computer simulations, extending its uses to different areas such as fluid flow physics, general relativity, plasma physics, and nuclear physics.

Now, thanks to the rapid increase of computer technology, which increases two times in computational capabilities every eighteen months, computational simulation has become an essential tool for research and development. Through the use of good computational models, not only can good results be obtained, but the freedom to vary different parameters of the simulation, allowing researchers to confirm existing theoretical models.

Any natural event can be reproduced in a digital computer with a prime requirement being that its behavior is governed by some partial differential equation (PDE). Therefore, in order to simulate a real event, these PDE's have to be solved for every unit of space and time. This crucial procedure of reproducing an event with infinite degrees of freedom would be impossible in current digital computers, however if discretization of space and time into specific intervals is done, the infinite becomes finite producing a discrete problem, and a solution using a computer becomes viable.

As mentioned in the introduction chapter, the simulation of a fluidized system under certain characteristics is one of the main objectives of this thesis. With the use of complex computer algorithms, a solution and explanation to our dilemmas can be obtained.

Chapter 3

Simulation Assumptions

This chapter will specify all of the assumptions made in the process of simulating a fluidized system. When performing experiments with industrial fluidized systems, different parameters had to be calibrated in order to obtain a desirable fluidization. When simulating this event in a digital computer, certain assumptions were made with the purpose of simplifying the simulation process. The assumptions made in this thesis were intended to be as close as possible to a real case scenario. From now on, this chapter will be referenced throughout this entire thesis, since it contains the key parameters for the simulations.

3.1 Simulation Characteristics

All of the code for the simulations was written in the C++ programming language, which was compiled using the g++ compiler and run on an Intel® Core™2 Quad Processor.

Since the real values used in experimental work can become overwhelming for a digital computer to process, all of the parameters used in this thesis were scaled to smaller computable values. The unit system used in this simulation was the Centimeter-Gram-Second system (CGS) and all of the values used were scaled to a sub-system of these units (micrometers (μm)-nanograms (ng)-microseconds (μs)) within the C++ code. Once final results were obtained, these values were scaled back and converted to their original units.

The fluidization container's geometry chosen for this project was cylindrical. The decision was made because this type of geometry avoids the hassles of the corner effect, which is caused when coating an object with corners; this effect is due to the concentration of electric field lines close to sharp edges.

In this project I intended to reproduce this cylindrical geometry as close as possible, for this purpose the boundary conditions chosen for axis x and y were periodic [48] which means that any particle that reaches and leaves the simulation domain through any of the edges of these axis will reappear on the other side. This technique is employed when trying to simulate large systems by modeling a small part that is far from its edge. Figure 3.1 presents a cubical box that is only periodic on the x and y axis.
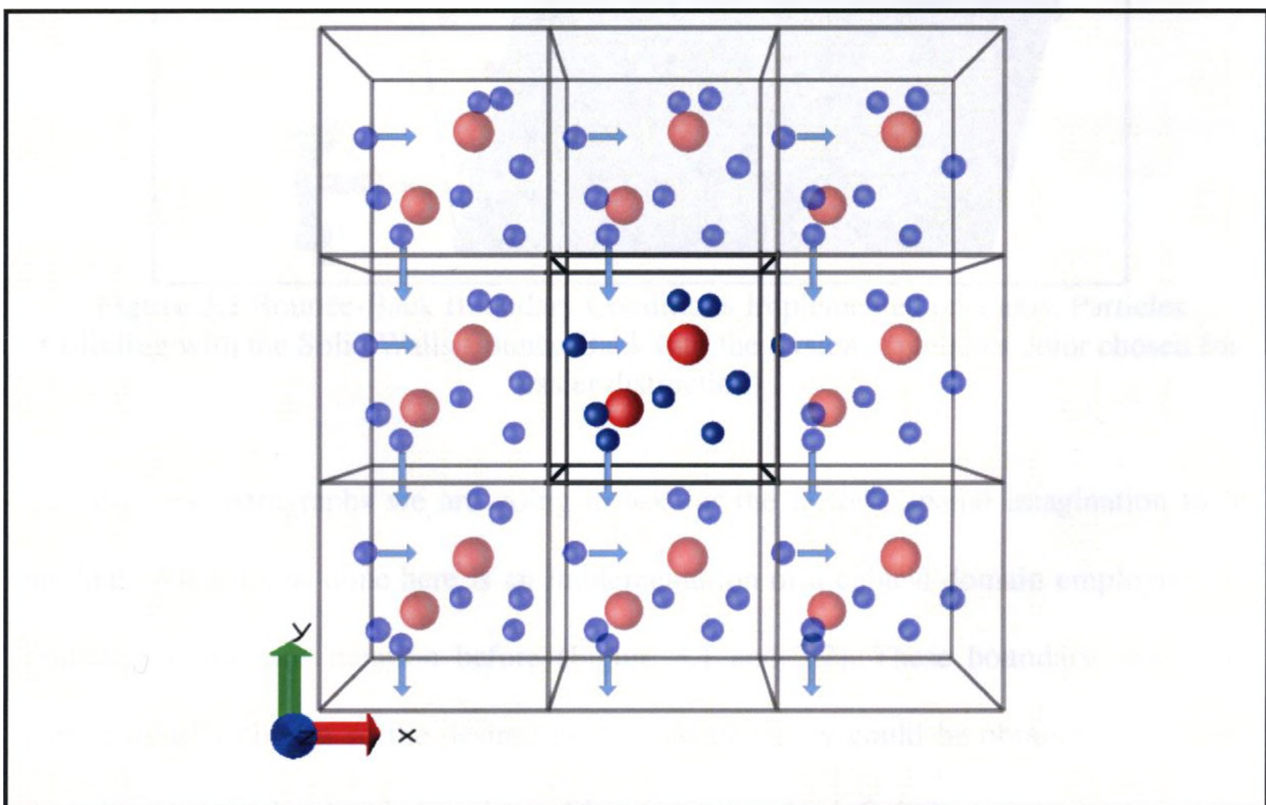
Figure 3.1 Periodic Boundary Conditions Implemented on x and y axis as a Repetition of Main Simulation Domain

On the other hand we had to simulate some sort of solid walls. For this the z axis was implemented as bounce-back (non-slip) [49] [50] boundary. In other words if the particles reach one of the ends (z axis), these will bounce-back into the system,Figure 3.2.
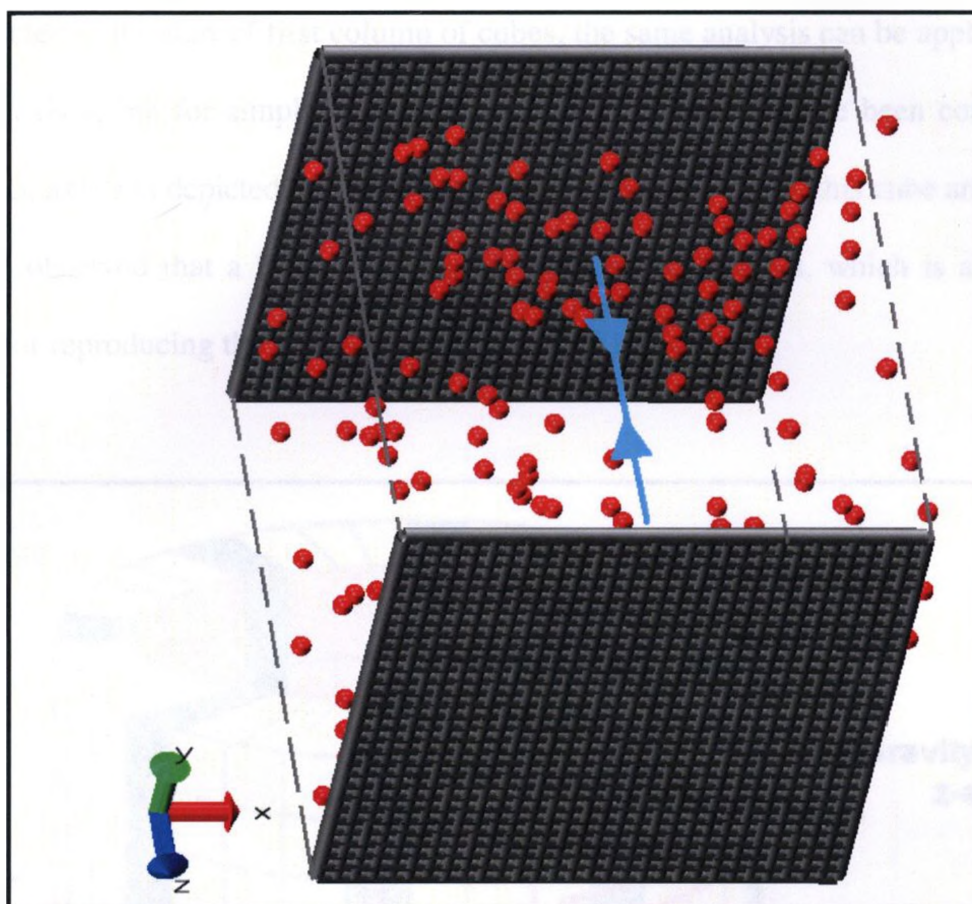

Figure 3.2 Bounce-Back Boundary Conditions Implemented on z axis, Particles Colliding with the Solid Walls Bounce-Back Into the System, (particles color chosen for easier distinction)

In these next paragraphs we are going to ask for the lector's spatial imagination to be applied. What it was done here is an implementation of a cubical domain employing the boundary conditions mention before (Figure 3.1 and 3.2). These boundary conditions were carefully chosen so the desired cylindrical geometry could be obtained. It is clear that the simulated cubical domain in Figure 3.1 can be infinitely repeated in the axis

where periodic conditions were declared, but for simplicity let's set an arbitrary finite number of simulation cubes, in Figure 3.3 the main simulation cube (Gray cube) is repeated 127 times, all these cubes were arrange in a way that a 32 x 4 wall is formed, then because of the periodicity of axis x and y, the end of the last column of cubes can be connected to the start of first column of cubes, the same analysis can be applied for the rows on axis y, but for simplicity only the edges of the x axis have been connected in Figure 3.3, axis z is depicted as two solid walls. As a final result of this cube arrangement it can be observed that a kind of concentric cylinder is obtained, which is a geometry suitable for reproducing the A.E.R.C. experiments [71].
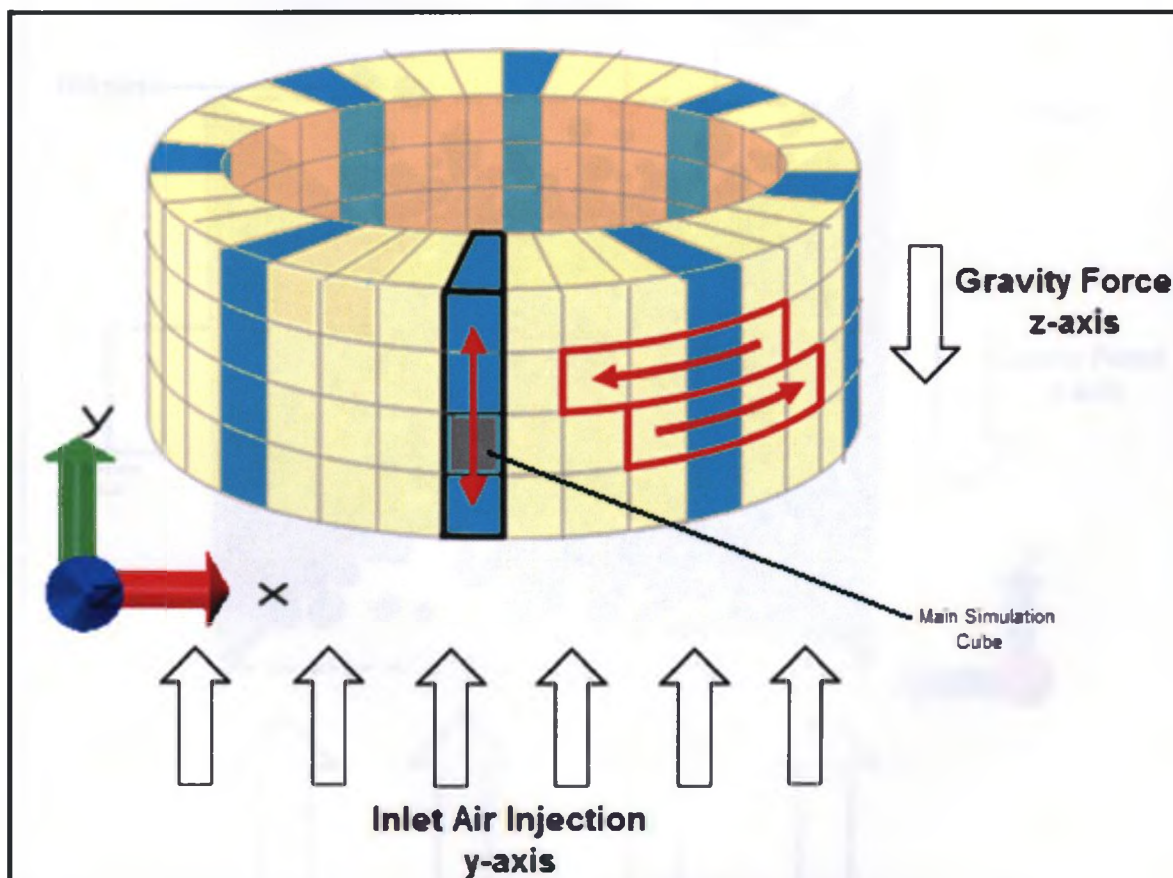
Figure 3.3 Simulation System Composed of a Collection of Milimetric Cubical Boxes Ensemble Together. Main Simulation Cube with Gray Shade Indicates the Simulated Cubical Box in this Project (Actual Size of Boxes in Figure are Much Larger than Normal). For Simplicity Cartesian Coordinates are employed in this Figure

There is no necessity to simulate the whole system, is just necessary to simulate a small part of it, in this case one of the simulation boxes (main simulation cube) should be enough to get an idea of the effects of the whole system. Figure 3.4 shows what goes on the main simulation cube. As we can see different size particles were suspended because of the fluid flow (air) injected from the bottom of the system, the solid walls were set to zero electric potential which simulated the electrically earthed walls used in past experiments. Furthermore, in order to increase the realism of the simulations, the force of gravity $(9.81 \frac{m}{s^2})$ was introduced in the y axis.
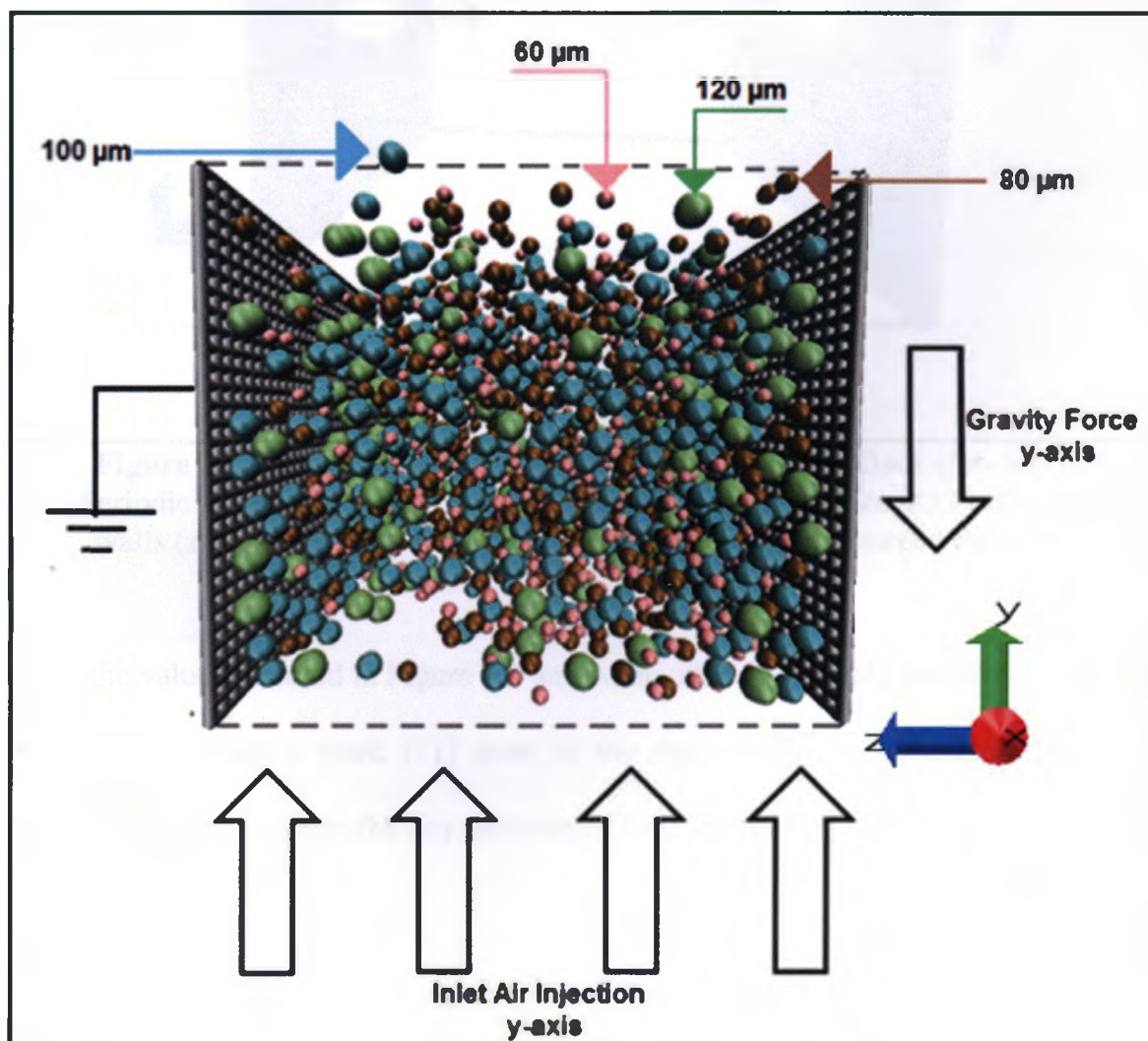
Figure 3.4 Main Parameters in Main Simulation Cube (Gray Box in Figure 3.3)

Also in this simulation an air inlet was located in the middle of each solid wall (Figure 3.5), at some point of the simulation this inlet flow was activated. This air flow entering the simulation domain carried unipolar charge particles, this intended to reproduce the experiment done in the A.E.R.C. [71].
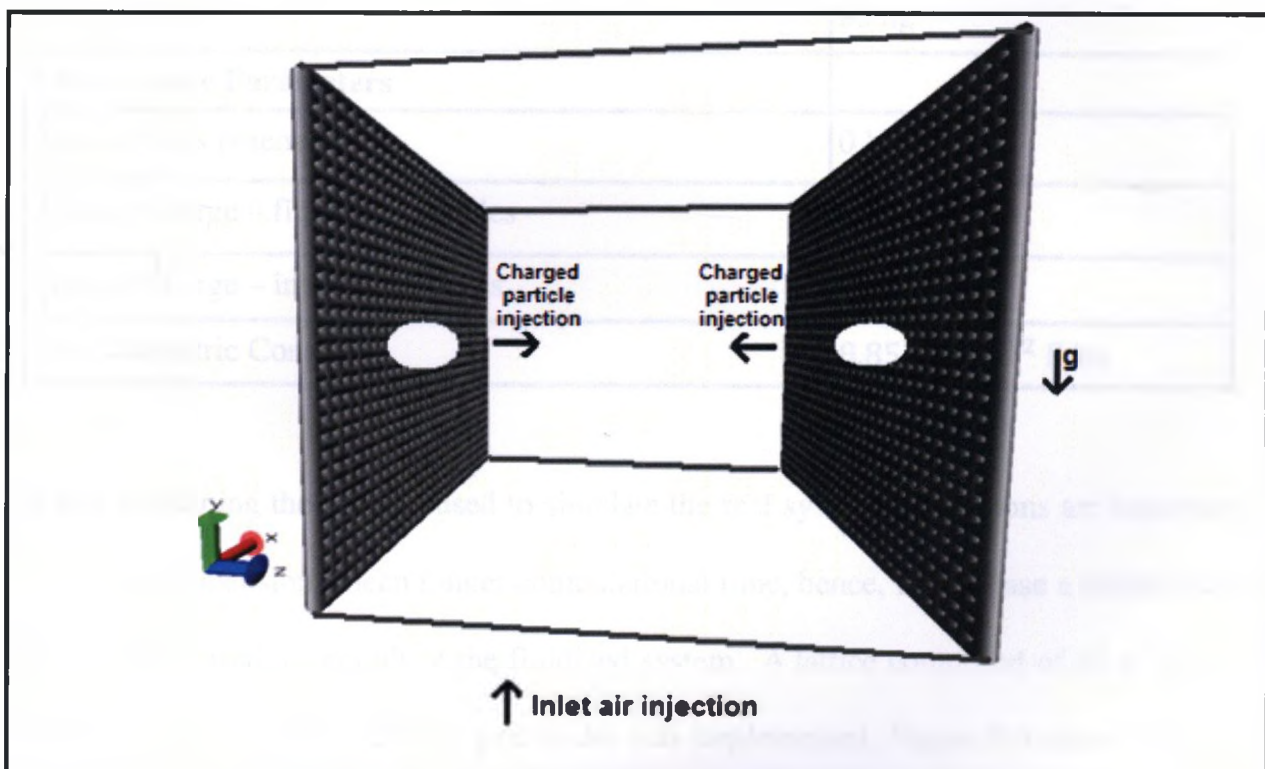

Figure 3.5 Boundary Conditions of the System, Bounce-Back (No-Slip) z Axis, Periodic Boundary Condition(x & y Axis), g Represents Gravity Force, Orifices at walls (z Axis) Indicate the Location of the Injection of Charged Particles

Most of the values pictured in Figure 3.4 and some other important parameters were taken from past experimental work [71] done in the Applied Electrostatic Research Center A.E.R.C. Table 3.1 presents the key parameters used in this simulation.

Table 3.1 Aerodynamic and Electrostatic Parameters

Aerodynamic Parameters	Metric system
Air Density	1.2 Kg/m^3
Air viscosity	17.9 $\eta \cdot (\mu Pa \cdot s)/m^3$
Inlet air-flow rate y-axis	$3.5 \cdot 10^{-3}$ m^3/s
Injection air-flow rate z-axis	$2.2 \cdot 10^{-3}$ m^3/s
Particle mass	85 ng
Electrostatic Parameters	
Solid Walls potential	0 V
Initial Charge – fluidized particles	0 C
Initial Charge – injected particles	10 e-14 C
Air Dielectric Constant	8.854×10^{-12} F/m

When explaining the domain used to simulate the real system, dimensions are important, and larger dimensions mean longer computational time, hence, in this case a miniaturized domain was used to reproduce the fluidized system. A lattice composed of 31 x 31 x 31 nodes forming a total of 29,791 grid nodes was implemented. Figure 3.6 shows the final simulation domain. These grid nodes are equally spaced, the distance between each node is 48 μm, multiplying the number of nodes by the value of the space between them results in the final domain dimensions of the lattice (1.488 x 1.488 x 1.488 mm). Since computers have to do lots of calculations when simulating these effects, the time steps between calculations should also be small, in this case every time step is equivalent to 48 μs.

Another important factor of these simulations is the geometrical characteristics of the particles. The shape of insulating particles is hard to define and since they were obtained

through a grinding process, the final shape they have is anything but spherical as commonly thought. Therefore, after discussing with my supervisors, the chosen geometry to simulate these particles was a truncated Icosahedron, which is composed by 60 vertices and 32 faces. Figure 3.7 shows the simulated geometry. In order to avoid any kind of complications when mentioning the particles throughout this thesis, simulated particles that are placed in the system prior to inflow injection will indistinctly be called fluidized or fluidization particles, and particles that are injected in the system at time step 10,000 (480 ms), will indistinctly be called injection or injected particles.
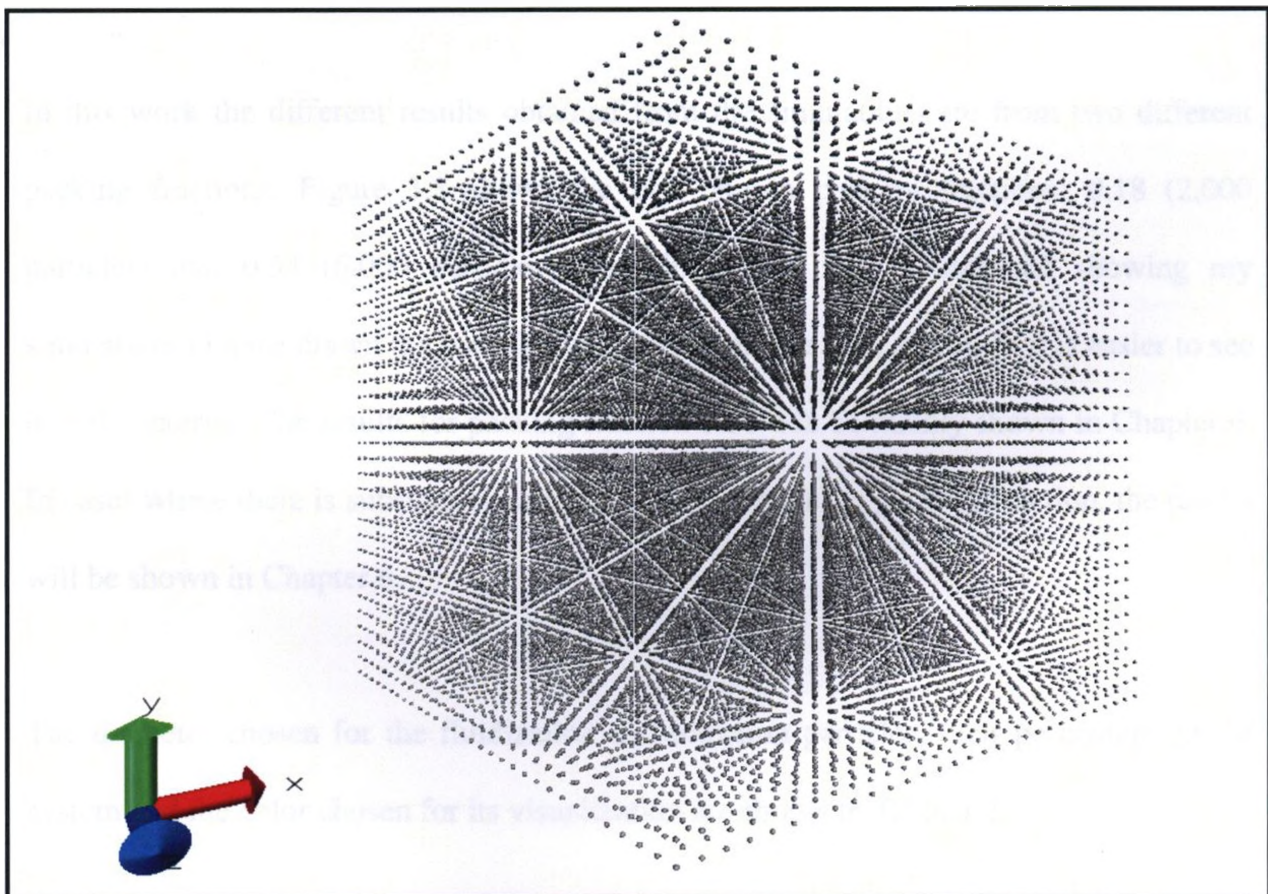
Figure 3.6 Discretization of the System in 29,791 Grid Nodes Forming the Simulation Domain

The simplification of problems is highly desired in the simulations of granular methods

where the particle sizes are small. All of the particles are assigned an equal mass value

(Table 3.1); therefore the typical particle velocities are independent of the particle size.
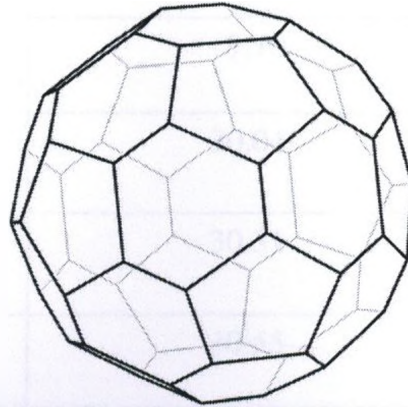
Figure 3.7 Simulated Particle Shape of a Truncated Icosahedron

In this work the different results obtained from the simulations are from two different

packing fractions. Figure 3.8 shows the two chosen packing fractions: 0.18 (2,000

particles) and 0.54 (6,000 particles).   In this figure (and subsequent showing my

simulations) I have drawn the particles with a smaller size than actual, so it is easier to see

into the interior. The results for packing fraction 0.18 will be mainly shown in Chapter 6.

In cases where there is substantial variation for the remaining packing fraction, the results

will be shown in Chapter 6.

The diameter chosen for the fluidization and injection particles, their percentage in the

system and the color chosen for its visualization are shown in Table 3.2.

The initial position for each particle is based on random placement inside the simulation

system. Figure 3.8 shows the initial particle configuration for the two different packing

fractions. In laboratory experiments, injection of charged particles started when the

tribocharging process had ceased. The same procedure is followed in this project.

Table 3.2 Parameters of the Fluidization and Injection Simulated Particles

Particle Diameter (µm)		Percentage (%) in System	Color of Particle
Injection particles	120	9.10	Lime green
Fluidized particles	100	30.04	Cyan
	80	30.31	Ochre
	60	30.55	Pink

At every time step new results for values such as velocity, density, and electric potential were obtained. Also within the computer code, different routines were used, these routines use the previous obtained results to equate a value for the x-y-z coordinates of every particle in the system. This means that after each time step, new values for particle's positioning in the domain were obtained. Also when reaching 15,000 time steps (720 ms), a text file was outputted containing all the values for all the parameters at every time step, then these values were scaled back to their original units of measurement for further analysis.
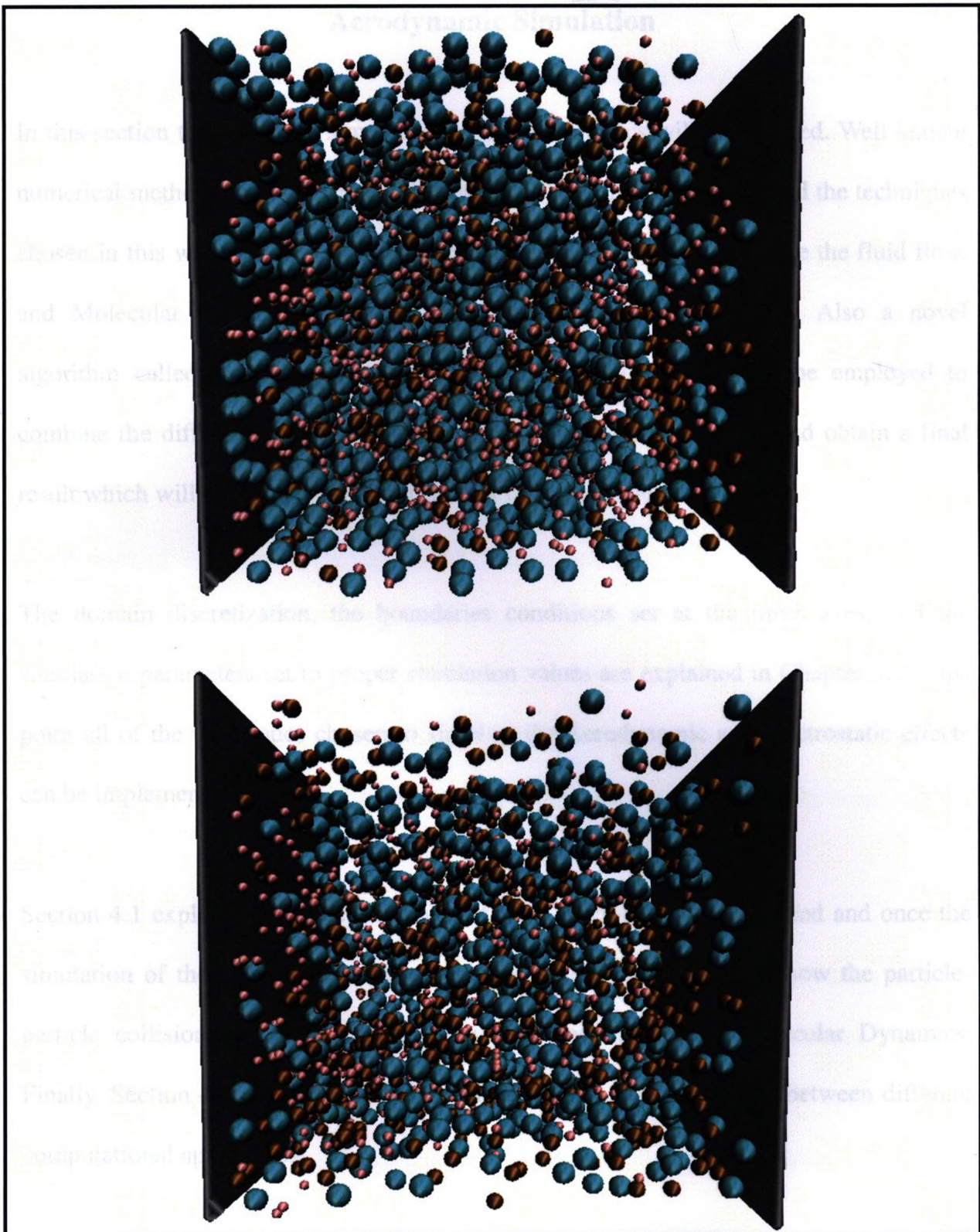
Figure 3.8 Packing Fractions: 6000 particles - 0.54 (Upper), 2000 particles - 0.18 (Lower), Presented at Time 0 ms

Chapter 4

Aerodynamic Simulation

In this section the computer simulations of fluid dynamics will be targeted. Well known numerical methods are used for simulating multiphase fluid dynamics, and the techniques chosen in this work are the Lattice-Boltzmann method (LBM) to simulate the fluid flow, and Molecular Dynamics (MD) to simulate the particle interaction. Also a novel algorithm called the Node Distribution Algorithm (NDA) [60] will be employed to combine the different outcomes at every time step of the simulation and obtain a final result which will determine the final behavior of the particle and fluid.

The domain discretization, the boundaries conditions set at the three axes, and the simulation parameters set to proper simulation values are explained in Chapter 3. At this point all of the techniques chosen to simulate the Aerodynamic and electrostatic effects can be implemented.

Section 4.1 explains the basic principles of the Lattice-Boltzmann method and once the simulation of the fluid flow has been achieved, Section 4.2 explains how the particle-particle collisions work by explaining a well known method, Molecular Dynamics. Finally, Section 4.3 presents a novel technique which allows coupling between different computational approaches.

4.1 Lattice - Boltzmann Methods (LBM)

Lattice-Boltzmann methods (LBM) are historically related to the Lattice-Gas Automata (LGA) method; In fact, the LBM was developed to avoid the inconveniences of the LGA methods. In 1989, Higuera and Jimenez [51] derived a Boltzmann equation for the distribution function of a LGA particle, and concluded that it was possible to use it as a viable method of simulation. Ever since, the Lattice-Boltzmann method has proven to be useful for the simulation of isothermal incompressible flows at low Reynolds numbers.

The Lattice-Boltzmann method simplifies Boltzmann's original concept. This is done by minimizing the possible number of particle positions and momentums, translating this continuum of values to a handful of discretized alternatives. In a three dimensional scenario a change in velocity or momentum is reduced for convenience to 15 directions, 3 magnitudes, and a single particle mass. In our 3-D case the model used it is known as D3Q15 because it has 3 dimensions and 15 velocities. There are also other models depending on the amount of dimensions and velocities. Table 4.1 presents some models [52].

For the sake of simplicity and without loss of generality, the Boltzmann equation with the Bhatnagar-Goss-Krook (BGK) approximation [53] is used in the following analysis. When a fluid using the LBM is being simulated, the movement at each lattice node is time dependent, this flux satisfies the following particle propagation equation:

$$F_i(x + e_i, t + \Delta t) = F_i(x, t) - \frac{\Delta t}{\tau}[F_i(x, t) - F_i^{eq}(x, t)] \qquad (4.1)$$

where F_i is the non-equilibrium distribution function, F_i^{eq} is the equilibrium distribution function, and e_i is the microscopic velocity at lattice node x at time t , respectively, and τ is the relaxation time which is a function of the fluid viscosity and Δt is the time step. By convention, units are chosen within the simulation so that $\Delta t = 1$ subscript i represents the lattice directions around the node (Figure 4.1).

The equilibrium distribution function (F_i^{eq}), was derived for various configuration models by He and Luo [54]:
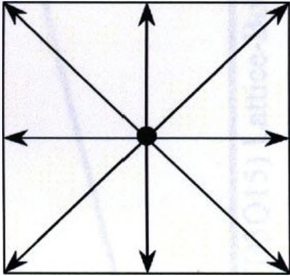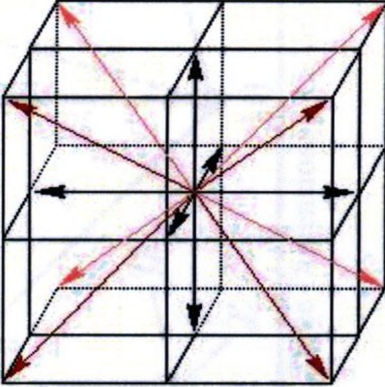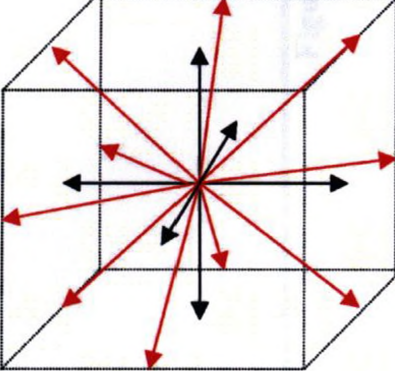
$$F_i^{eq} = w_i \cdot \rho \cdot \left[1 + 3 \left(\frac{e_i \cdot u}{c^2} \right) + \frac{9}{2} \cdot \left(\frac{e_i \cdot u}{c^4} \right)^2 - \frac{3}{2} \frac{u^2}{c^2} \right] \tag{4.2}$$

In this case ρ is the fluid density, w_i is the weight factor in the i_{th} direction, u is the macroscopic velocity of the nodes, and $c = \Delta x / \Delta t$, where Δx and Δt are the lattice constant and the time step size, respectively. Equation 4.2 is a particular choice that sets the pressure proportional to density, $P = \frac{1}{3} \frac{\Delta x^2}{\Delta t^2} \rho$.

Weight factors were derived by Wolf-Gladrow [55] and vary from model to model in LBM. For the D3Q15 model these values can be found in Table 4.1 among other model weight values. The distribution function at every direction is used to define the macroscopic density and momentum at a specific node:

$$\rho = \sum_{i=0}^{Q} F_i \tag{4.3}$$

Table 4.1 Properties of Commonly Implemented Lattice-Boltzmann Models
Note: Weight factors for [1] rest particle, [2] face-connected neighbours, and [3] edge-connected neighbours

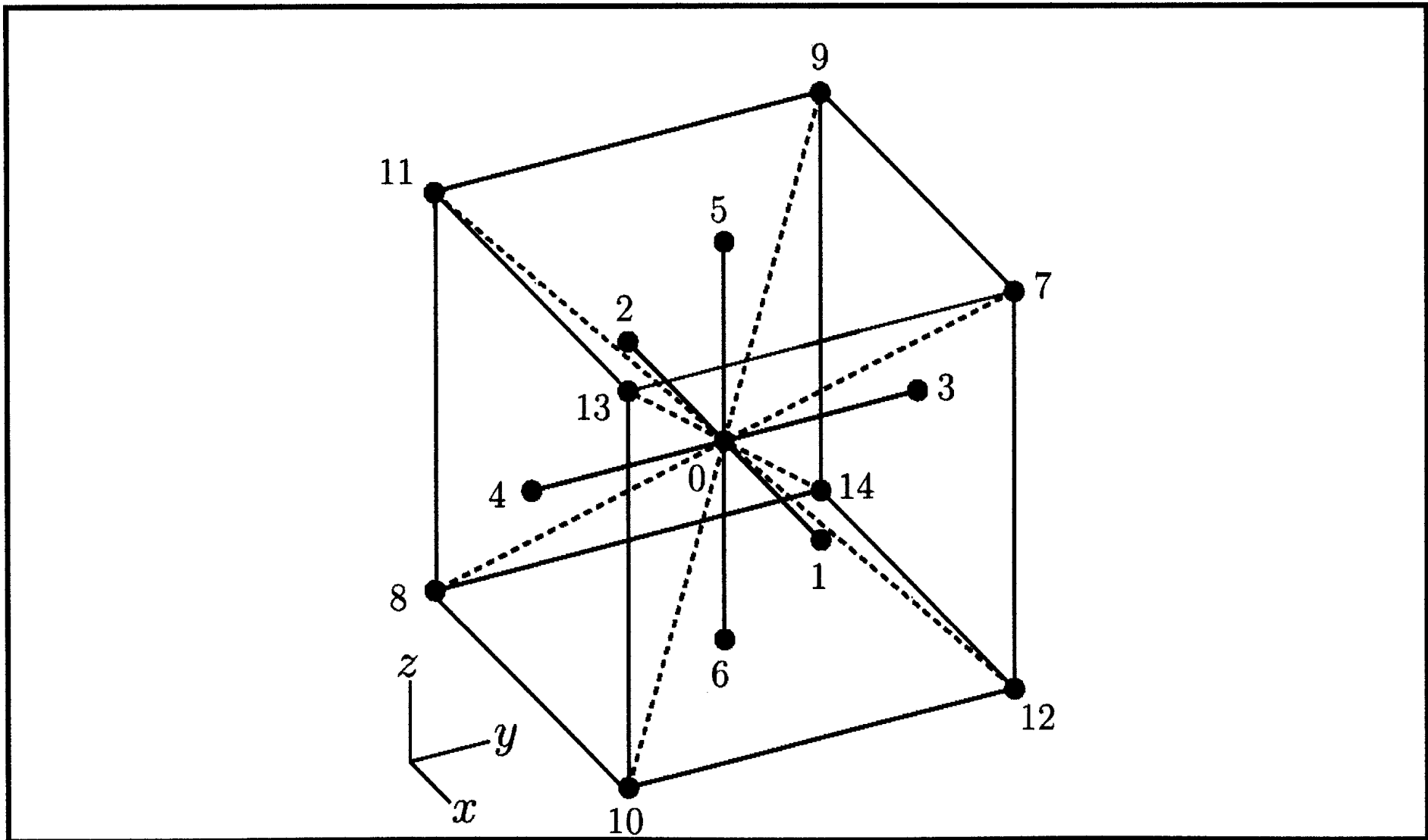| Model Name	Weight Factor	Velocity Directions
D1Q3	$4/6_{(1)}$	
D1Q5	$6/12_{(1)}$ $2/12_{(2)}$ $1/12_{(2)}$	
D2Q9	$16/36_{(1)}$ $4/36_{(2)}$ $1/6_{(3)}$	
D3Q15	$16/72_{(1)}$ $8/72_{(2)}$ $1/72_{(3)}$	
D3Q19	$12/36_{(1)}$ $2/36_{(2)}$ $1/6_{(3)}$	

Figure 4.1 Three Dimensions - 15 Velocities (D3Q15) Lattice-Boltzmann Model

$$U = \sum_{i=0}^{Q} [F_i . e_i] \qquad (4.4)$$

With the knowledge of the macroscopic density (ρ), the macroscopic velocity (u) at any specific node can be obtained by:

$$u = \frac{1}{\rho} \sum_{i=0}^{Q} [F_i . e_i] \qquad (4.5)$$

Once the values of macroscopic velocity and density have been determined they can be incorporated into Equation 4.2 to obtain F_i^{eq}, which means that a final solution to Equation 4.1 can be obtained, consequentially simulating an incompressible fluid flow.

4.2 The LBM for the Navier - Stokes Equation

None of the fundamentals employed in the numerical simulations of uncompressible fluid flow would make any sense if these methods would not obey specific rules of physics. In this case the Lattice-Boltzmann method is no exception to the rule.

When it comes to reproducing different kinds of fluid flows, the equation that rules this behavior is known as the Navier-Stokes equation. The Lattice-Boltzmann method is known for its effectiveness in modeling this governing equation of fluid flows. The following paragraphs show how the incompressible Navier-Stokes equation can be derived from Equation 4.1 in a three dimensional space; therefore proving that the

Lattice-Boltzmann method is a different way of approaching the same basic idea.

The derivation of the Navier-Stokes equation from the Lattice-Boltzmann approach starts by operating with Equations 4.1 and 4.2., Using Equations 4.3 and 4.4 with 4.2, it can be easily verified to see that:

$$\sum_i f_i^{eq} = \rho \tag{4.6}$$

$$\sum_i f_i^{eq} \cdot e_i = U \tag{4.7}$$

therefore it is straightforward to see that Equation 4.1 exactly conserves mass and momentum.

If we take Equation 4.1 and Taylor expanded, we get:

$$\sum_{n=1}^{\infty} (\Delta t)^n \left(\frac{\partial}{\partial t} + e_{i\alpha} \frac{\partial}{\partial x_\alpha} \right)^n F_i = -\frac{\Delta t}{\tau} (F_i - F_i^{eq}) \tag{4.8}$$

if we take Equation 4.8, and sum over i, (using Equations 4.6 and 4.7), it can be show that we obtain:

$$\frac{\partial \rho}{\partial t} + \frac{\partial}{\partial x_\alpha}(\rho \mu_\alpha) = 0$$

<div align="right">(4.9)</div>

on the other hand if we take Equation 4.8 and multiply it by e_i and sum over i, it can be show that we get:

$$\frac{\partial(\rho \vec{u})}{\partial t} + \nabla \cdot (\rho \vec{u}) = -\nabla P + \mathcal{V}\nabla^2 u + \mathcal{O}(M^3)$$

<div align="right">(4.10)</div>

where M is the lattice Mach number, $\frac{|u|}{c}$, $P = \frac{1}{3}\rho$ and finally $\mathcal{V} = (\frac{2\frac{\tau}{\Delta t}-1}{6})\frac{\Delta x^2}{\Delta t}$. As it can be noticed the Navier-Stokes equations (Equations 4.9 and 4.10), can be obtained from the Lattice-Boltzmann equations.

4.3 Molecular Dynamics (MD)

Using Lattice Boltzmann Method as the air flow simulator; a method to reproduce the particle-particle and particle-wall interaction was needed. Due to its simplicity of implementation and efficiency of computational time, the Molecular Dynamics (MD) [56] [57] method was chosen.

Molecular Dynamics is a common computer simulation technique that follows the time evolution of a set of interacting particles by integrating their equations of motion. When simulating any substance (solid, liquid, or gas), the most basic microscopic model is based in spherical particles or atoms that interact only with each other. Interactions at a

simplistic level happen between particles and are responsible for the two most important features of inter atomic force.

The first of these two forces is the resistance to compression, which means that when particles are at a close distance, there will be a repulsion force between them. Its physical origin is related to the Pauli principle, which states that: *"when the electronic clouds surrounding the atoms start to overlap, the energy of the system increases abruptly"*.

The second is the force which binds the particles together; this means that an attraction force will exist between the particles over the separation range due to the Van der Waals dispersion forces. The interactions between any pair of particles will only involve each pair independently, with other particles in the neighborhood having no effect on the force between them.

Potential functions that exhibit these characteristics can be adopted in order to simulate the interaction between two particles. The choice of function depends on what aspect of a real case scenario will be simulated. The selection must be done carefully to provide useful results.

The potential function employed in this research, is the Lennard-Jones potential (LJ) [58] [59]; and states that for a pair of particles i and j located at points r_i and r_j, the potential energy is:

$$u(r_{ij}) = 4\epsilon[(\frac{\sigma}{r_{ij}})^{12} - (\frac{\sigma}{r_{ij}})^6] \qquad r_{ij} \leq r_c \tag{4.11}$$

where two particles i and j located at different coordinates (r_i and r_j), are separated by distance $r_{ij} = r_i - r_j$. Also r_c is the cut-off distance, which in other words means distance where elastic collision starts. The other two parameters of the Leonard-Jones equation have specific and valuable meaning. The parameter ϵ governs the strength of the interaction, and σ represents the collision diameter.

The first part of Equation 4.11, describes a steep repulsive term at short ranges between particles ($\frac{1}{r^{12}}$), and the second part ($\frac{1}{r^6}$), which is originated from the Van der Waals dispersion forces, describes a smooth attraction term between the same two particles at long ranges. Figure 4.2 presents the L-J potential. In our case we need only repulsive forces so we cut-off the potential at its minimum.

At long ranges, there is an attractive force (negative potential) between the particles, if the distance between particles increases no attraction exists, therefore the L-J potential will be equal to zero. At short ranges, the force between particles increases abruptly causing repulsion between them (positive potential).

The great advantage of this technique is its simplicity to implement. Through this method, the simulation of classical multi-body systems can be achieved with ease simply by selecting a system with a finite number of solid particles and then solving Newton's

equation for each particle.
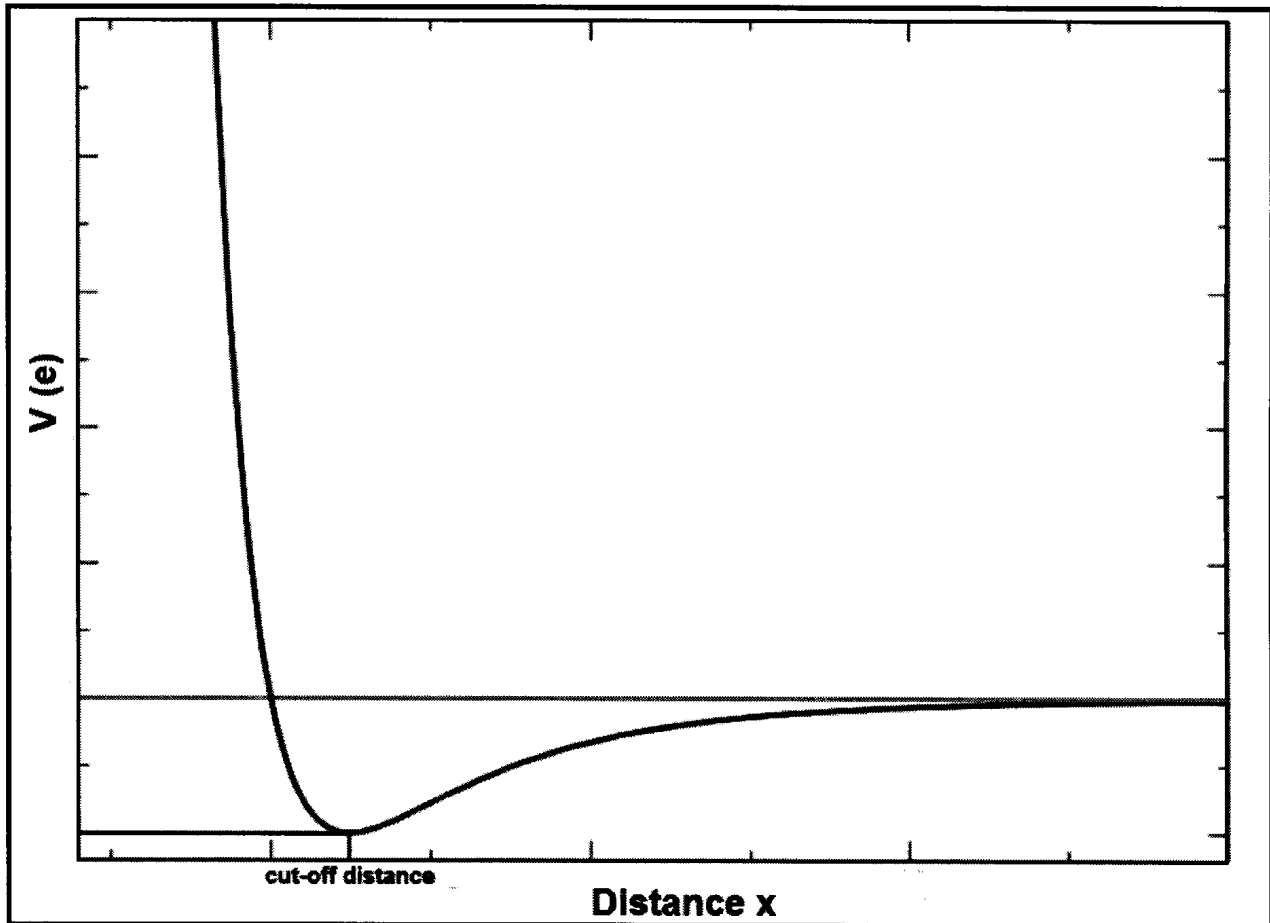
Figure 4.2 Lennard - Jones Potential V(e) Between Two Particles Separated by a Variable Distance x

4.4 Node Distribution Algorithm (NDA)

When simulating a multiphase flow, which has different packing fractions and densities, the necessity to interact with any number of components is a priority. In this thesis, two components are part of this flow. On one hand there is the fluid flow (air), and in the other, icosahedron-shaped moving particles. These two phases exert forces on each other affecting one another's behavior.

Once discretization has been done, we end up with a 3-D cubical lattice (Figure 3.2); as

mentioned before each point of the lattice is called a grid node. If we want to simulate a solid moving object in a fluid flow, we first define a number of nodes, which will be called surface nodes, these nodes play the role of the particle's surface. Figure 4.3 shows a particle's surface which contains 60 surface nodes which simulate a truncated icosahedron, reviewed in Figure 3.3.
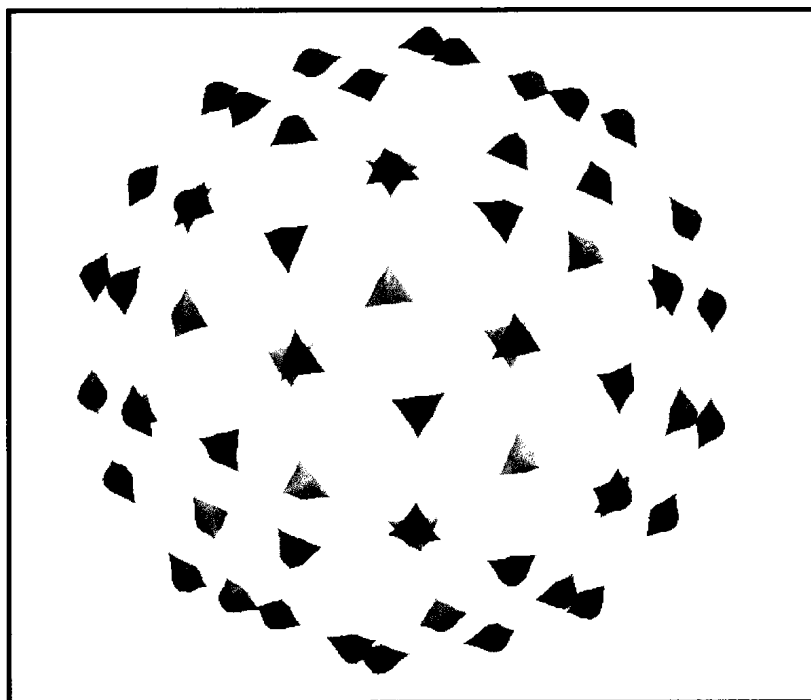
Figure 4.3 Surface Nodes (60) Located at the Surface of a Truncated Icosahedron (Solid Insulating Particle)

These surface nodes are then pixilated onto the lattice mesh. For simplicity, a 2-D case is shown as an example in Figure 4.4. To complete the interaction between these two phases, a weighed value is calculated for every surface node corresponding to every surrounding grid node. For example in Figure 4.4 for the surface node i, the calculated weight (ξ_{ij}) when j = P1 is $A1/dx^2$. By doing this, it is easy to observe that the values of the weights shift from zero (when they are at opposite sides) to one (when surface node

and grid node occupy the same place).

By using this logic, a weight number is calculated for every surface node taking their surrounding grid nodes as a reference. As the particles move through the fluid an interaction occurs between the two phases. The way this interaction is handled using NDA [60] is explained in the following analysis.

The surface node locations (r_i), are calculated having the center of mass as a reference of the moving solids. The velocity of each node is then calculated using $v_i = v + w \cdot r_i$, where v is the velocity of the center of mass of the solid, and w is the angular velocity of the solid. Applying the logic described in Figure 4.4, the i_{th} surface nodes have a certain weight value (ξ_{ij}), which is determined by the affected j_{th} grid node.

As mentioned before, the two way interaction starts by finding the local forces exerted on each grid node site j affected by the surface's node i:

$$F_{ij} = (v_i - u_j)\xi_{ij}\rho_j\gamma \qquad (4.12)$$

where u_j is the velocity of the fluid and ρ_j is the density of the fluid at the j_{th} grid node, and γ is the proportionality constant.

By using:

$$F_j = \sum_j F_{ij} \qquad (4.13)$$
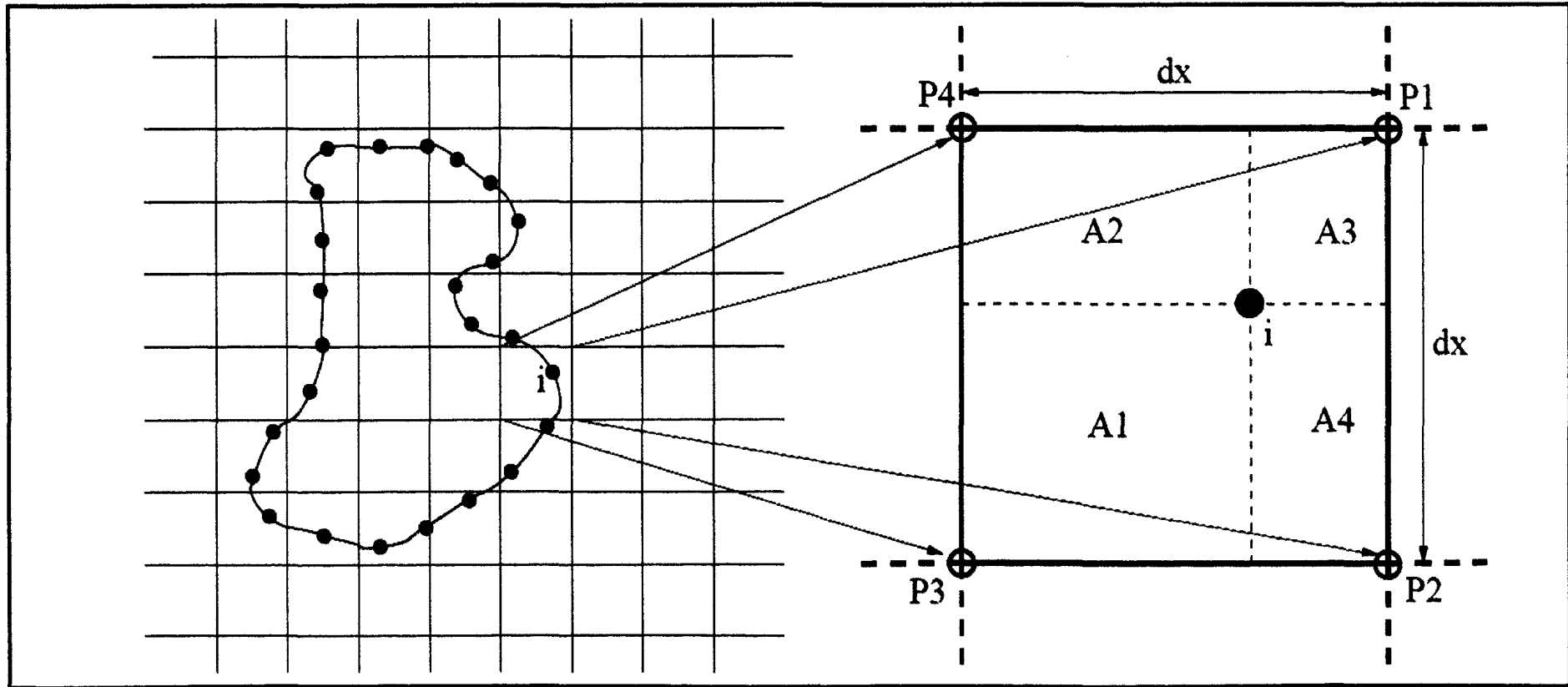
Figure 4.4 Single Node (Solid Circle) Placed Within the Fluid Mesh (Hollow Circles) [60]
(Taken from "Lattice Boltzmann simulations of colloidal Aerodynamics", By C.J. Smith and C. Denniston, under consideration for publication in Journal Fluid Mechanics, (2007))

the force at every local grid node affected by all the nearest surface nodes is obtained, this final force is then incorporated into Equation 4.3 and 4.4 to obtain a final density and velocity value at every grid point.

Similarly the forces exerted by the fluid onto every surface node are calculated using:

$$F_i = \sum_{j=1}^{8} F_{ij} \tag{4.14}$$

$$T_i = r_i \times F_i \tag{4.15}$$

Also the net forces and net torques that the fluid exerts on the particle's surface nodes are:

$$F = \sum_i^N \sum_j^8 F_{ij} \tag{4.16}$$

$$T = \sum_i^N \sum_j^8 T_{ij} \tag{4.17}$$

where N is the number of particle's surface nodes. As mentioned before, the grid nodes are used to simulate the fluid flow, hence a velocity value is known at every grid node.

In the case of particle-particle and particle-wall interactions, when two surface nodes of

different particles or particle-wall come closer than the MD cut-off distance, a repulsion force between these two surface nodes will be instantly generated (Figure 4.2). This provokes the particles to repeal each other, simulating an elastic collision.

Chapter 5

Electrostatic Simulation

This chapter presents the approaches taken to simulate the electrostatic effects. An introduction to electrostatic simulations is given in Section 5.1. Section 5.2 presents a novel technique to simulate tribocharging systems based on fundamentals of electric theory. Section 5.3 presents the steps taken to compute the electric potential. Once this value is obtained, simple calculations follow to obtain the overall electric field and the electric forces that are applied to every particle.

5.1 Electrostatic Simulation

When doing computer simulations of electrically charged systems, the data are obtained at every small period of time. These periods of time are also known as time steps. In this work a constantly moving system of charged particles is solved at every time step.

As mentioned in Chapter 2, when a particulate system is fluidized, particles tend to collide with each other and with the walls triggering a tribocharging process [25] [26] [27] [28] [29] [30]. The model chosen to reproduce the tribocharging process in this thesis is referred to as the trapped electron model [37].

Once the values of total net charge on every particle are known, the calculation of the values for the electrostatic potential is not a cumbersome procedure to solve since all of its principles are ruled by Poisson's equation (Equation 5.8). Employing a novel algorithm

[60], the total net charge of every moving charged particle can be easily discretized from all of its surface nodes into its surrounding grid nodes. Then, just a few steps are necessary to solve Poisson's equation and consequently find the electrical potential and electric field intensity of interest at any given grid node.

Vast research has been done in the simulation of particulate systems in various fluids [41] [42] [44] [45]. However, most work has only taken into account the trajectories of each particle due to the effects of fluid dynamics. Electrostatic forces were discarded due to their insignificance, which in later years was proven wrong [61] [62] [63]. Hence, the main motive for this project was not only to simulate the forces that the fluid exerted on the particle's paths but also to couple them with the electrostatics forces.

In the case of simulations in fluid dynamics, a review of the techniques used was given, but the electrostatic step only involves well-known calculations. The major concern was to determine the most efficient and economic C++ library to solve Poisson's equation.

5.2 Trapped Electron Model (TEM)

Through many years of experiments and research, Dr. I.I. Inculet and his team at the A.E.R.C [26] [27] [28] [30] often experimented with a variety of fluidized systems where similar material particles acquired a bipolar charge when fluidized.

Different models have been developed to try to explain these phenomena; each one of them taking into account different characteristics of the particles and their fluidization

process as the crucial ones for tribocharging [64] [65]. A novel simulation method known as the trapped electron model was chosen to simulate the tribocharging process within solid fluidized particles. This method was first implemented by Lowell and Truscott [66], and later used with satisfactory results by Duff and Lacks [37].

The principle for its implementation is based on the knowledge that similar insulating particles contained spatially localized electron states (traps) on their surface. Figure 5.1 shows this aspect of the technique (Lines represent empty high energy states, and dots represent occupied low energy states). These states are distributed over a range of energy and normally low energy states are occupied by electrons, and most high energy states are empty; however some electrons are located in high energy states.

These trapped electrons in high energy states have a permanent position since they are not able to make the transition to lower energy states within the same insulating particle. However, when two similar particles come into contact (Figure 5.1), each of them will have fewer electrons trapped in its high energy state. If during collision, an electron in a high energy state comes into close contact with a "trap" in a different low energy state particle, that electron would be transferred. Due to this electron transfer, the total net charge of every insulating particle will vary according to the number of transferred electrons.

Once an electron has been transferred to a low energy state, it will remain trapped there. It can be clearly noted that electrons only flow in one direction (high energy states → low energy states) but not the other way around.
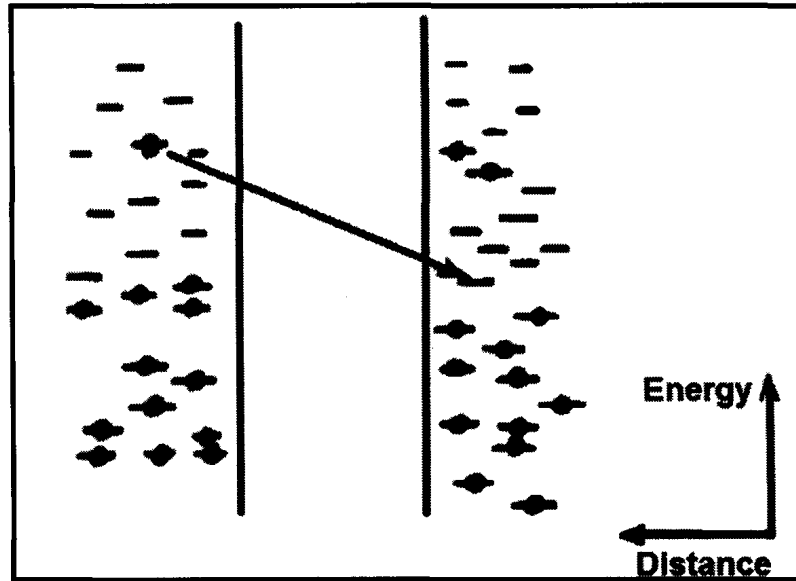
Figure 5.1 Non-Equilibrium Electron Distribution Between Similar Materials [66] (Taken from "Tribo-electrification of identical insulators", By J. Lowell and W.S. Truscott, Journal of Physics D: Applied Physics, vol. 19, pp. 1281-1298, (1986))

The implementation of this technique in our simulations starts by first locating the places that high energy state electrons are going to occupy; the location of these places are randomly chosen to reproduce the particle's electric properties as close to reality as possible. Since different size particles were used in the simulations, the number of high energy state electrons is directly proportional to the square of the particle's diameter. Initially (time = 0 ms) all particles have identical surface density (ρ_0) of trapped electrons in high energy states, and no captured electrons in low energy states:

$$n_{H_x}(t) = 4\pi\sigma^2\rho_0 \qquad \text{when} \quad t = 0 \qquad (5.1)$$

$$n_{L_x}(t) = 0 \qquad \text{when} \quad t = 0 \qquad (5.2)$$

where $n_{H_x}(t)$ and $n_{L_x}(t)$ are electrons trapped in high energy state and low energy state respectively; σ is the particle diameter ($4\pi\sigma^2$ is the surface area of a particle), and ρ_0 is the initial surface density of trapped electrons. The amount of electrons that can be captured in low energy states is higher than the initial quantity of electrons that initially were located in the high energy states. In this simulation the ratio chosen between the total number of low and high energy states was 5:1, this means that for every filled high energy state in a particle there are five empty energy states, these values were consistent with experiments done in the past [66].

Figure 5.2 illustrates how all the points have been randomly located and its location saved into a memory array.
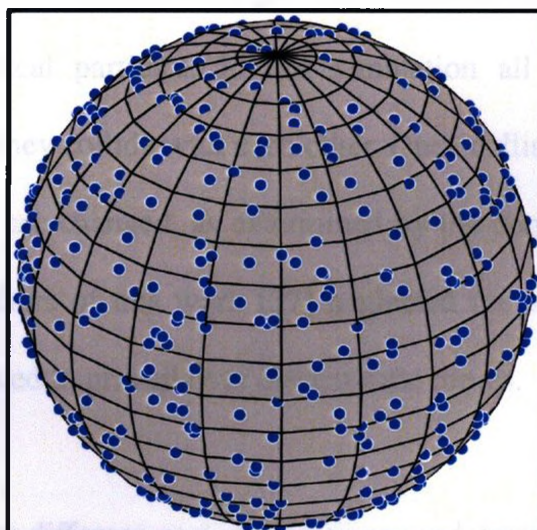
Figure 5.2 Localized Positions of Filled High Energy States (Blue Dots) and Empty Low Energy States (Gray Areas)

When a collision between particles A and B occurs, all the high energy state electrons of particle A that are within a cut-off distance ($d_{cut-off}$) of the point of collision, are transferred to low energy states of particle B and vice versa, this is how the electron

transfer process works.

Insulating particles have initially zero total net charge. Once the process is triggered, net charges can be developed due to the transfer of electrons. By applying the following formula the total net charge in every insulating particle can be obtained.

$$q_{(t)} = -\left(\left[n_{H_x}(t) + n_{L_x}(t)\right] - \left[n_{H_x}(0) + n_{L_x}(0)\right]\right) \qquad (5.3)$$

The negative sign in front of the equation accounts for the negative charge of an electron.

The results obtained by Duff and Lacks [37] were gratifying, and were used as a reference for this project. The authors of this work [37] simulated a scenario where charge transfer was possible due to electrons trapped in high energy states, which were released during collisions between identical particles. In this simulation all the particles moved at constant velocities, until they collide with each other. Once collision occurs, the velocities of the colliding particles are changed, as determined by the conservation laws of energy and momentum. The authors of this work [37] neglected the electrostatic effects, since inertial forces were assumed to prevail over electrostatic forces.

Figure 5.3 shows the three different packing fractions used during these simulations [37], which are 0.044, 0.25 and 0.55, the particles colored red are the ones that after simulation acquired a negative net charge, and the particles colored blue positive net charge. At first glance, most of the larger particles have a positive net charge and most of the smaller particles have a negative net charge after simulation.
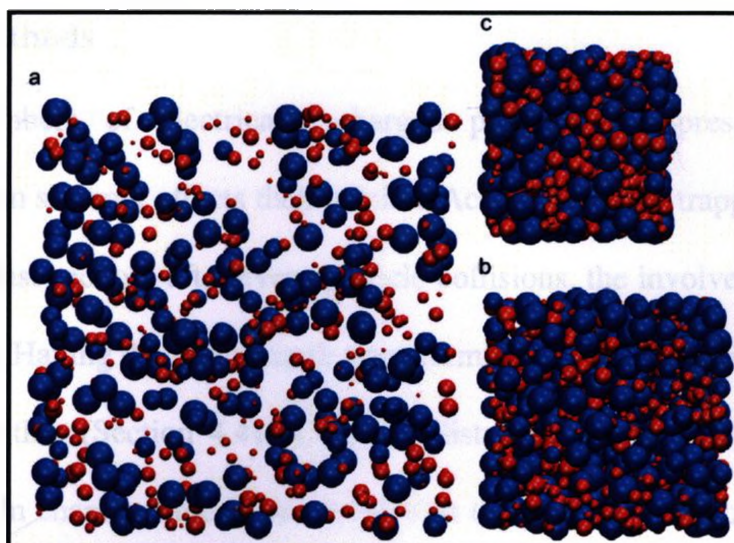
Figure 5.3 Snapshots of the System at the End of Simulations, at Packing Fractions (a) 0.044, (b) 0.25, and (c) 0.55 [37]
(Taken from "Particle dynamics simulations of triboelectric charging in granular insulator systems", By N. Duff and D.J. Lacks, Journal of Electrostatics, vol. 66, pp.51-57, (2008))

Figure 5.4 shows a clearer view of this phenomenon, where particle charge (dimensionless form) as a function of particle diameter is shown for the three different packing fractions. As it can be noticed the smaller particles tend to charge negatively as opposed to the larger particles.
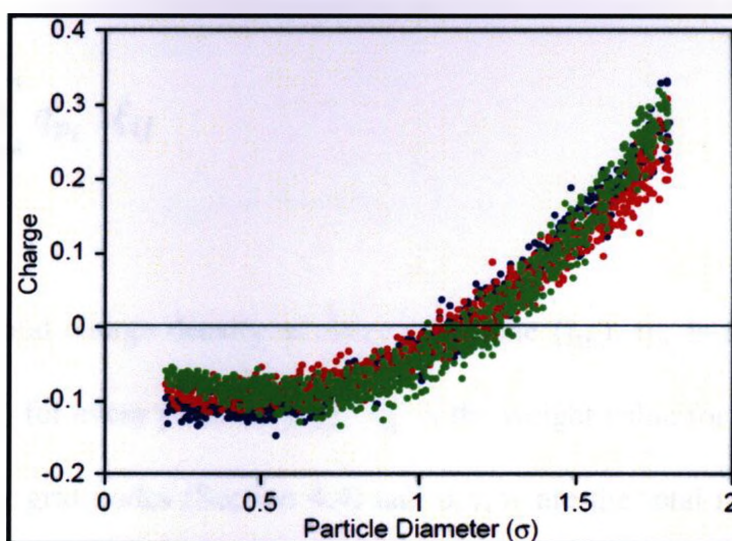
Figure 5.4 Particle Charge as a Function of Particle Diameter, Packing Fractions of 0.044, 0.25, and 0.55 are Shown as Blue, Red and Green Symbols, Respectively [37]
(Taken from "Particle dynamics simulations of triboelectric charging in granular insulator systems", By N. Duff and D.J. Lacks, Journal of Electrostatics, vol. 66, pp.51-57, (2008))

5.3 Spectral Methods

When large numbers of electrically charged particles are present, their mutual repulsion/attraction strongly affects their motion. According to the trapped electron model explained in the last section, after every particle collisions, the involved particle acquires a total net charge. Having the lattice mesh predetermined by the fluid simulation, the node distribution algorithm (Section 4.4) is used to distribute the volume charge density to every grid node. In chapter three it was stated that the particle's surface is reproduced by surface nodes, also the total net charge of every particle can be considered equivalent to a point charge, so to interpolate the total net charge of every particle into their surrounding grid nodes, the next measurements have been taken.

The total net charge of every particle is divided by the number of surface nodes (60 surface nodes), this is done in order to obtain a uniform surface charge at every particle, and then the total charge in every grid node is equated using:

$$\rho_j = \sum_p^u \sum_i^v \sum_j^w q_{p_i} \cdot \xi_{ij} \tag{5.4}$$

where ρ_j is the total charge density at every grid node (j_{th}), q_{p_i} is the charge of every surface node (i_{th}) for every particle (p_{th}), ξ_{ij} is the weight value for every surface node to its surrounding grid nodes (Section 4.4) and u, v, w are the total number of particles, surface nodes, and grid nodes respectively. Once the charge density for every grid node has been obtained and under the assumption that permittivity ε throughout the system is

constant, Poisson's equation (Equation 5.8) can be solved easily.

According to a subset of Maxwell's equations customized for electrostatics:

$$\nabla.\vec{D} = \rho \qquad (5.5)$$

$$\nabla x\,\vec{E} = 0 \qquad (5.6)$$

where ρ is the charge density, $\vec{D}$ is the electric displacement field, and $\vec{E}$ is the electric field. From electrostatic theory is well known that $\vec{E}$ is:

$$\vec{E} = -\nabla\emptyset \qquad (5.7)$$

where $\emptyset$ is the electric potential.

By solving Equations 5.5, 5.6 and 5.7, Poisson's equation can be obtained as follows:

$$\nabla^2\emptyset = -\frac{\rho}{\varepsilon} \qquad (5.8)$$

where ε is the air permittivity. Once Poisson's equation has been solved for any given value of charge density and permittivity, the equated result will be the value of the electric

potential $\emptyset$. As observed in Equation 5.7, by solving the gradient of the electric potential

$\emptyset$, the value of the electric field $\vec{E}$ can be obtained.

The technique used to deal with the Poisson's equation at every grid node is called the Spectral method [67] [68] and involves the use of the Fast Fourier Transform (FFT). There are a few FFT algorithms that can be used, some of them are well documented some are not, while some are for commercial use only. The Spectral method library chosen for this project is FFTW [69], which is a free well documented library for C++.

The fundamentals on how this mathematical process works are shown as follows. Poisson's equation is a clear example of an elliptic partial differential equation, FFT can be used to solve these kind of equations in multiple dimensions. The three dimensional Poisson's equation can also be written in this format:

$$\left(\frac{\partial^2}{\partial x^2} + \frac{\partial^2}{\partial y^2} + \frac{\partial^2}{\partial z^2}\right) \emptyset(x,y,z) \approx$$

$$\frac{1}{\Delta^2}\left[\emptyset_{j+1,k,l} + \emptyset_{j-1,k,l} + \emptyset_{j,k+1,l} + \emptyset_{j,k-1,l} + \emptyset_{j,k,l+1} + \emptyset_{j,k,l-1} - 6\emptyset_{j,k,l}\right]$$

$$=> -\frac{\rho_{j,k,l}}{\varepsilon} \tag{5.9}$$

where Δ is the spacing between grid nodes, $\emptyset$ is the electric potential, ρ is the charge density, and ε is the permittivity constant of air. The domain has an N x N x N grid of points (Figure 3.2), every grid node has a specific equated charge density value $\rho_{j,k,l}$.

In order to proceed with a solution, boundary conditions must be specified. The appropriate boundary condition determines the appropriate type of Fourier transformation to solve the problem. Some boundary condition will require a sine transformation to solve it (Dirichlet Boundary Conditions), others may require a cosine (Neumann boundary condition) or exponential (periodic boundary condition) transformation. In the case of this work, periodic boundary conditions are applied to the mentioned domain to obtain a final solution. An extra step is taken for properly simulating the fact that the solid walls in the z axis are earthed, this extra step will be explained later in this chapter.

The discrete Fourier transformation is a linear operation, so it can be applied separately in the x, y, and z axis, regardless in which order the transformations are done. The 3-D Fourier coefficients are given by:

$$\tilde{\phi}_{m,n,p} = \frac{1}{N^{\frac{3}{2}}} \sum_{j=0}^{N-1} \sum_{k=0}^{N-1} \sum_{l=0}^{N-1} W^{mj+nk+pl} \phi_{j,k,l} \tag{5.10}$$

$$\tilde{\rho}_{m,n,p} = \frac{1}{N^{\frac{3}{2}}} \sum_{j=0}^{N-1} \sum_{k=0}^{N-1} \sum_{l=0}^{N-1} W^{mj+nk+pl} \rho_{j,k,l} \tag{5.11}$$

their inverse transforms are:

$$\phi_{j,k,l} = \frac{1}{N^{\frac{3}{2}}} \sum_{m=0}^{N-1} \sum_{n=0}^{N-1} \sum_{p=0}^{N-1} W^{-jm-kn-lp} \tilde{\phi}_{m,n,p} \tag{5.12}$$

$$\rho_{j,k,l} = \frac{1}{N^{\frac{3}{2}}} \sum_{m=0}^{N-1} \sum_{n=0}^{N-1} \sum_{p=0}^{N-1} W^{-jm-kn-lp} \, \tilde{\rho}_{m,n,p} \qquad (5.13)$$

For simplicity W was chosen to replace $e^{i\frac{2\pi}{N}}$. Inputting these expressions into the discretized equation and equating coefficients of $W^{-mj-nk-pl}$ results in:

$$\frac{1}{\Delta^2}[W^m + W^{-m} + W^n + W^{-n} + W^p + W^{-p} - 6]\tilde{\emptyset}_{m,n,p} = -\tilde{\rho}_{m,n,p} \qquad (5.14)$$

this is solved for:

$$\tilde{\emptyset}_{m,n,p} = \frac{\Delta^2 \tilde{\rho}_{m,n,p}}{6 - W^m - W^{-m} - W^n - W^{-n} - W^p - W^{-p}} \qquad (5.15)$$

then applying the inverse Fourier transformation the electric potential can be obtained, which is the final solution for Poisson's equation at every discrete grid node. Substituting this value into Equation 5.7 the electric field at every grid point can be calculated.

5.4 Simulation of Zero Potential Walls (Earthed Walls)

When a system is fluidized, the container that holds the particles normally has a potential of zero, which in other words means that the container is earthed. Since an exact reproduction of this case scenario is desired, the solid walls on the z axis are set to zero

potential. This is done by implementing the image charge method [70], where a particle of equal but opposite charge is placed at opposite sides from the solid walls. This technique is widely used in electrostatic problems. Figure 5.3 shows a 2-D example for a particle with charge q located at a distance "a" from the wall.

To complete the task in this thesis, each simulated particle has its own image charge located in the opposite side of the solid walls (z axis), to finally solve the problem by using spectral methods, explained previously. Image charges for both walls are implemented by creating one image of the box in the z-direction and then applying periodic boundary conditions over 2.Lz (box + image), where Lz is the domain value in the z direction.
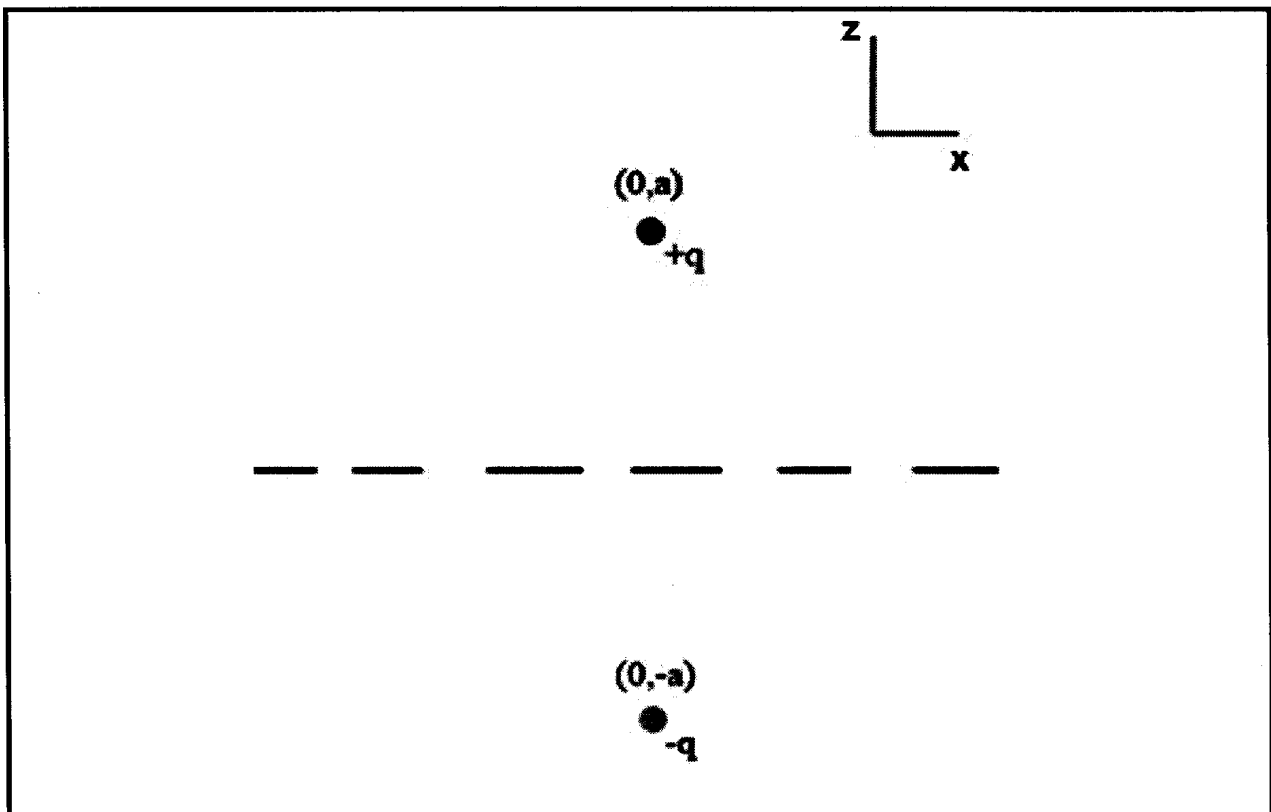
Figure 5.5 Image Charge Method Apply to a Particle Located a Distance (a) from the z Axis with Charge (q)

5.5 Electrostatic Force

The next step is to calculate the electric force exerted on every particle. In order to do so, the total net charge is divided between the numbers of surface nodes (Figure 4.3); consequently the total net charge of the particle is uniformly distributed between the surface nodes.

As mentioned in Section 4.4, each surface node has a weight that correspond to its surrounding grid nodes, applying this logic a weight value is obtained for each surface-grid node combination (ξ_{ij}), hence the electric field at every surface node can be obtained:

$$E_i = E_j \xi_{ij} \tag{5.16}$$

where E_j is the electric field at every grid node, and E_i is the electric field at every surface node from every particle, once the electric field intensity at every surface node is obtained, the next formula is applied to obtain the electric force applied to every surface node from every particle.

$$\sum_{i=0}^{SN} F_{e_i} = E_i \, q_i \tag{5.17}$$

where q_i is the electric charge at every surface node, F_{e_i} is the electric force at every surface node, and SN is the total number of surface nodes per particle. All of these forces per particle are algebraically added to obtain a final resultant electric force. To obtain the

final total force in every particle a simple mathematical procedure is done:

$$F_{tot} = F_D + F_e \qquad (5.18)$$

Equation 5.18 indicates that the electric force (F_e) is algebraically added to the drag force (F_D) to obtain a final total force (F_{tot}), this final force dictates the particles' trajectories.

5.6 Routine Demonstration

A demonstration that the simulation of the electrostatic process used in this thesis works is shown here. One way to do it is by locating 961 positively charged particles, and having 961 negatively charged particles located on the opposite side (image charge), this configuration imitates a parallel plate capacitor. All the original values in this demonstration were scaled, so a digital computer could easily handle the multiple calculations, therefore, these scaled values have no units. The distance between plates is 30 (along z axis) and the area of each plate is 900. Figure 5.6 shows this arrangement of particles. The charge per particle (injected particles) was chosen to be 10 e-14 Coulombs, once this value is scaled for proper computation it becomes 2.6; standard textbook calculations to obtain the values for the capacitance (C), the electric potential (V) and the electric field Intensity (E), are:

$$C = \varepsilon_0 \frac{A}{d} = 1 \times \frac{900}{30} = 30 \qquad V = \frac{Q}{C} = \frac{961 \times 2.6}{30} = 83.3 \qquad E = \frac{V}{d} = \frac{83.3}{30} = 2.7$$
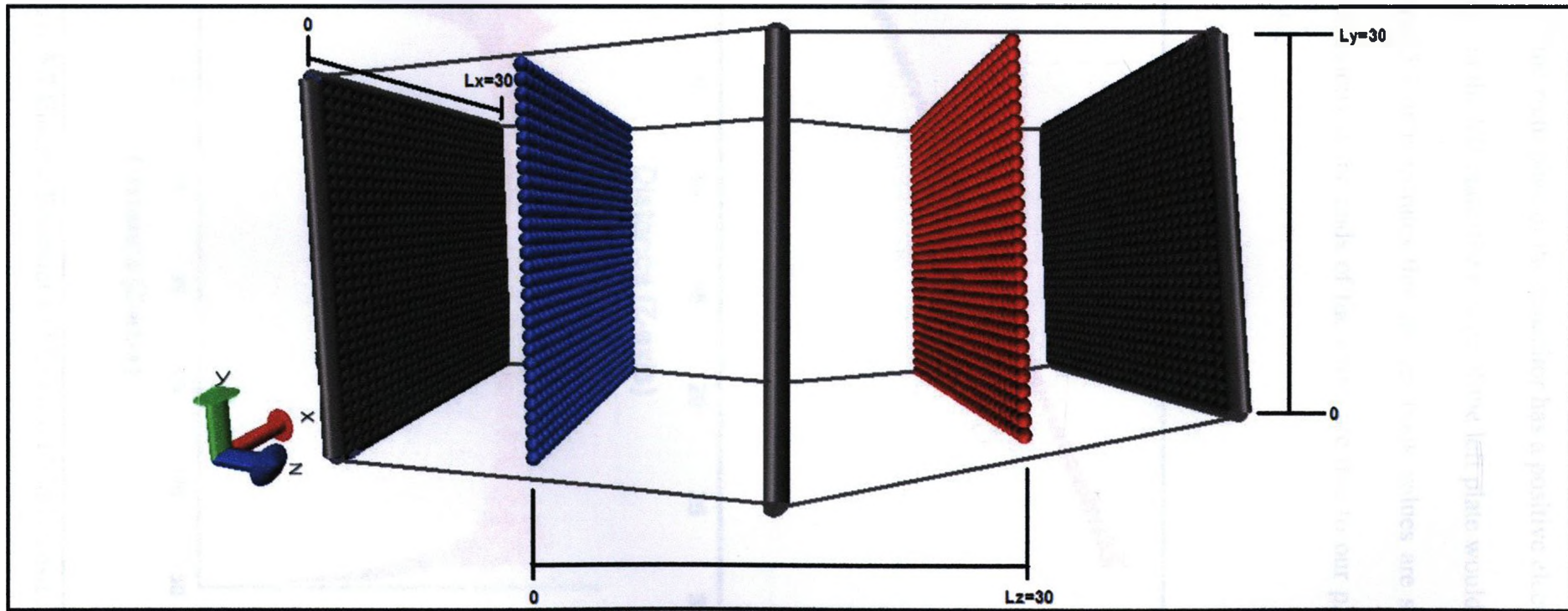
Figure 5.6 Positive Charged Particles – 961 (Red-Right) and Their Respective Negative Image Charge (Blue-Left) Enclosed in a Periodic simulation Domain (Left-Center-Right Grey Walls)

From Figure 5.6 the right plate of the capacitor has a positive electric charge, using image charge particles on the left plate, the charge of the left plate would be similar but opposite in value. Figure 5.7 demonstrates that the textbook values are similar to the simulated values. The deviations at the ends of the curve are due to our plate being composed of discrete particles.
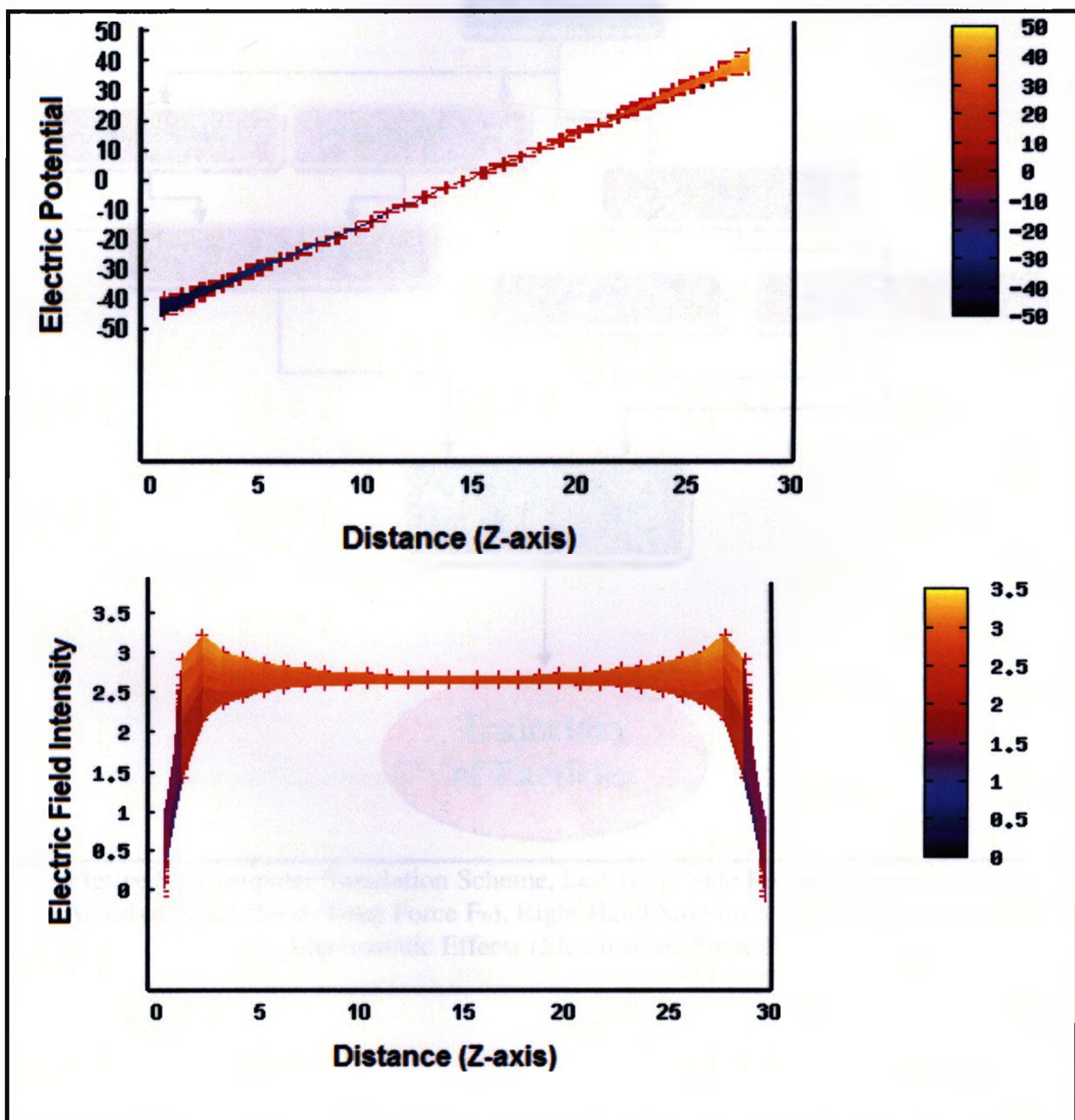
Figure 5.7 Electric Potential and Electric Field Intensity Along z axis

5.7 Computer Simulation Scheme

At every time step, the results of the aerodynamic and electrostatic effects were obtained, then a series of calculations were done to obtain final results of all of the particles 3-D coordinates. Figure 5.8 show how the computer simulation scheme was organized.
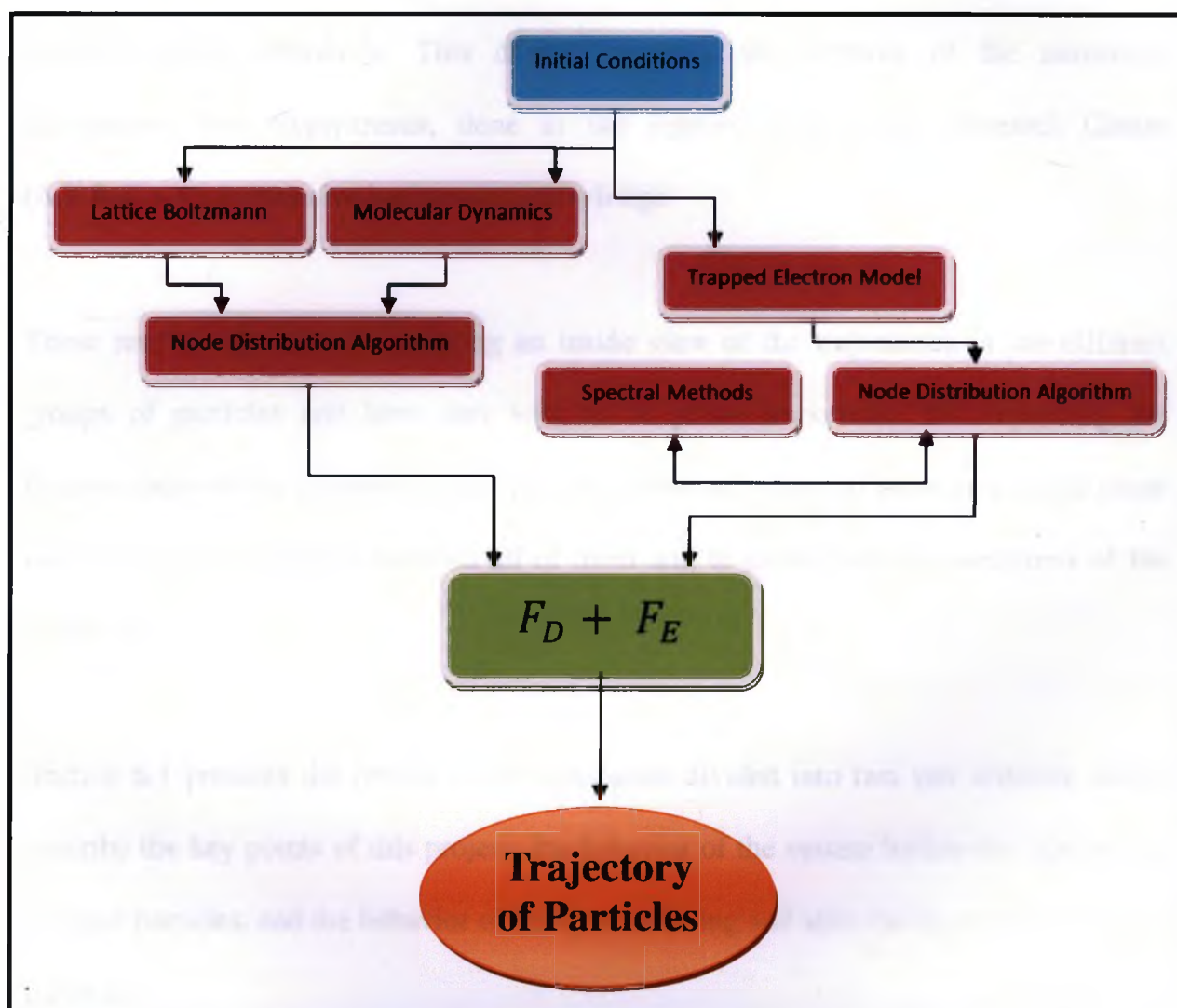
Figure 5.7 Computer Simulation Scheme, Left Hand Side Involves Simulation for Aerodynamic Effects (Drag Force F_D), Right Hand Side Involves Simulation of the Electrostatic Effects (Electrostatic Force F_E)

Chapter 6

Results and Conclusions

The purpose of writing a customized computer code is to simulate the fluidized system process with specific parameters, something that under commercial software is not always possible and/or affordable. This chapter presents the outcome of the numerical simulations. Past experiments, done in the Applied Electrostatic Research Center (A.E.R.C.), give extensive background knowledge.

These results were aimed at getting an inside view of the trajectories of the different groups of particles and how they will be of prime importance for explaining the disappearance of the injected charge. Thus it is emphasized not to focus on a single graph but to see the connection between all of them and to understand the usefulness of the whole idea.

Section 6.1 presents the results of the simulation divided into two sub sections, which describe the key points of this project; the behavior of the system before the injection of charged particles, and the behavior of the system during and after the injection of charged particles.

Section 6.2 shows the results of previous experimental work done in 2004 at the A.E.R.C., and finally Sections 6.3 and 6.4 present the conclusions and future recommendations.

6.1 Simulation Results

This section presents the results regarding various aspects of the simulation. The figures that will be shown throughout this section can be analyzed independently. However grouped together, each graph will represent something that relates to the main idea. The main purpose of this project was to find out why, after the injection of charged particles, the system does not acquire the expected net charge. With this motive in mind all of the information presented here should be connected to solve this quest.

As a reminder from Chapter 3 the different particles in the system are identified as fluidized or fluidization particles, which include the 60, 80, and 100 μm particles and the particles that are injected into the system are identified as injected particles which have a diameter of 120 μm.

All simulations start at time step 0 (0 ms). After 10,000 time steps (480 ms) injection of particles begins, this is done in groups of 8 particles every 20 time steps (.96 ms), which takes 500 time steps (24 ms) for all the particles to get injected into the system. After injection is done at about 10,500 time steps (504 ms), the simulation continues to run until it reaches 15,000 time steps (720 ms), at which point simulations are halted and results are obtained.

In summary the simulations are divided into two main stages: prior to injection, from 0-480 ms, and during/after injection, from 480 - 720 ms. The results are organized in a way that these two key moments during the simulation are well defined and explained in the

next two sub sections.

6.1.1 Prior to Injection (0 – 480 ms)

Once the different boundary conditions have been set for each axis and the particles have been located in the system, the fluidization of the system begins. As previously mentioned, in order for this to occur, an adequate air flow has to be injected from the bottom of the system (y axis). As this air injection increases, it reaches a specific value when the pressure drop across the system is enough to cancel out the effects of gravity (F_g), which causes the particles to levitate.

After this levitation, the particles start to circulate in the simulation domain. Movement of the particles is slowly noticed. In this circulation process the particles slowly begin colliding against each other at various frequencies as well as some particles collide against the walls, this collision process triggers a charge transfer which, as mentioned in Chapter 5, is simulated by the charge transfer model [37].

Prior to the initialization of the particle collision process and therefore charge transfer, it has to be stated that the electron distribution per area on the surfaces of all the particles is the same (Section 5.2). In other words, for an enclosed space of particle's surface the same amount of electrons is inhabitated. This means that larger particles have a larger surface thus having more electrons than those of the smaller particles. Figure 6.1 shows the various electron numbers for two different size particles, and the dots at the surface represent the number of high energy state electrons.
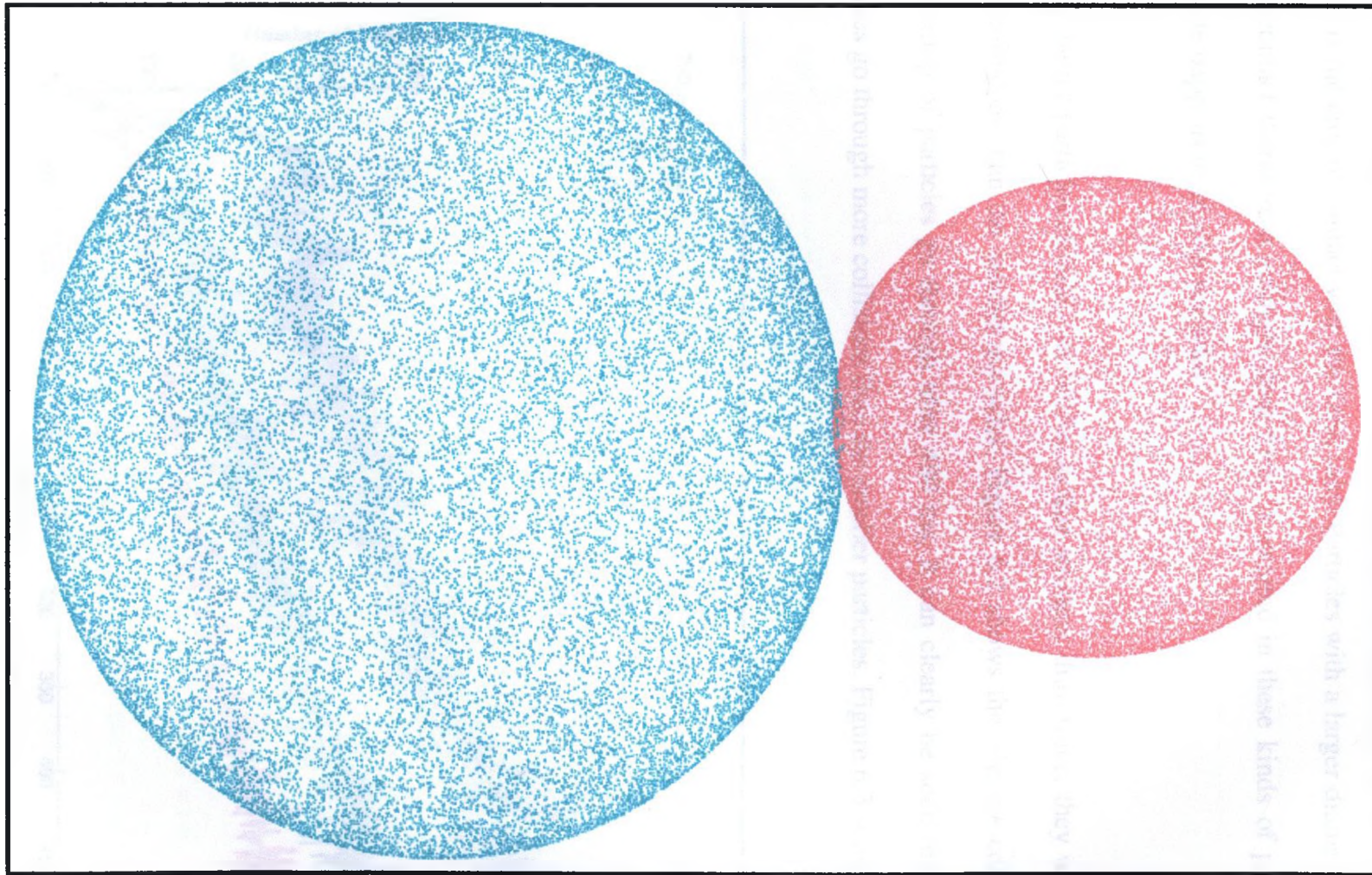
Figure 6.1 Area of Contact of Particles with Different Diameters

Recalling the information reviewed in Chapter 4, the fluid flow has an effect on the trajectories of all the particles, the main parameter that defines how fast or slow a particle moves is the area of contact with the fluid (air). Particles with a larger diameter will have more contact therefore a stronger drag force is exerted in these kinds of particles, the opposite happens to smaller particles.

As the larger particles circulate more due to this stronger drag force, they will undergo more collisions than the smaller particles. Figure 6.2 shows the average collisions that each group of particles go through after 480 ms. It can clearly be seen that the larger particles go through more collisions than the smaller particles. Figure 6.3 shows the
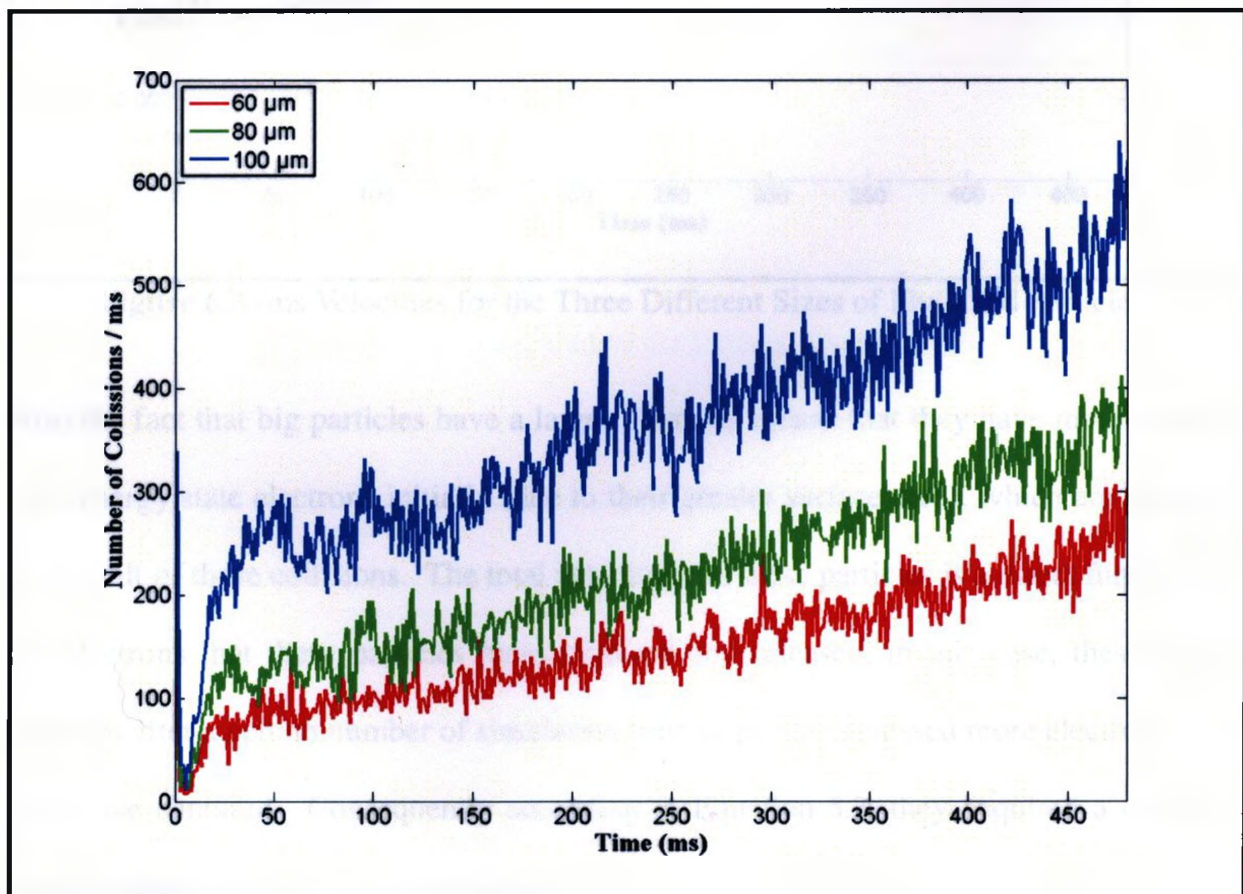
Figure 6.2 Number of Collisions for the Three Different Sizes of Fluidized Particles

rms velocity of every group of fluidized particles. As stated, the larger particles move faster due to their larger surface area conversely the smaller particles move slower.
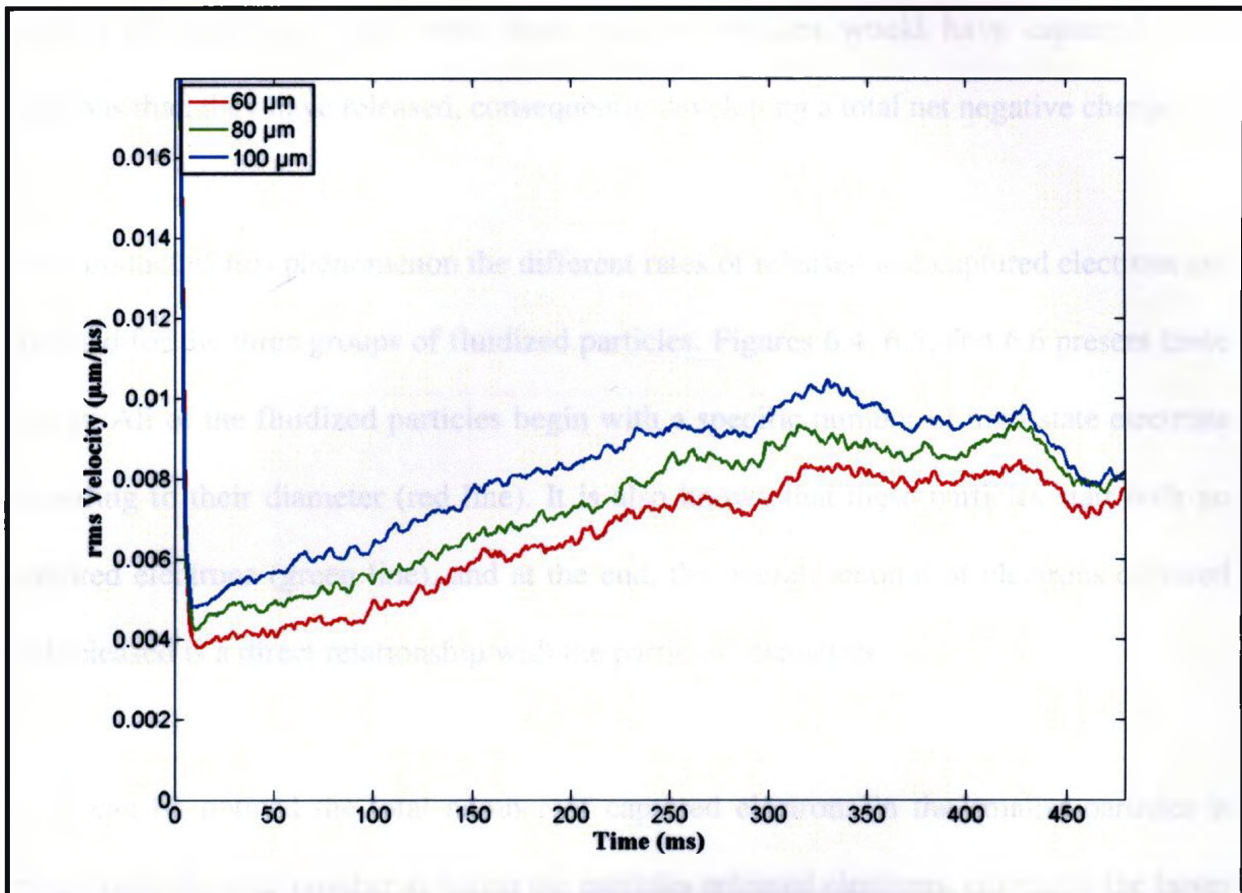
Figure 6.3 rms Velocities for the Three Different Sizes of Fluidized Particles

Also the fact that big particles have a larger diameter means that they have more trapped high energy state electrons initially (due to their greater surface area), which are released as a result of these collisions. The total net charge in these particles is a direct function of the electrons that these particles have captured and released, in this case, these larger particles after a certain number of simulation time steps have released more electrons than they have captured. Consequently according to Equation 5.3, they acquired a total net positive charge.

Conversely the smaller particles do not undergo as many collisions as the larger particles (Figure 6.2), and its smaller diameter indicates that they initially have less high energy state electrons on their surface (Figure 6.1), which in the end means that after a certain number of simulation time steps, these smaller particles would have captured more electrons than they have released, consequently developing a total net negative charge.

As a product of this phenomenon the different rates of released and captured electrons are obtained for the three groups of fluidized particles. Figures 6.4, 6.5, and 6.6 present these results. All of the fluidized particles begin with a specific number of high state electrons according to their diameter (red line). It is also known that these particles start with no captured electrons (green line), and at the end, the overall amount of electrons captured and released is a direct relationship with the particles' diameters.

As it can be noticed the total number of captured electrons in the smaller particles is higher than the total number at which the particles released electrons; contrarily the larger particles released more electrons compared to the total number of electrons they captured. These differences in numbers are what make up the final total net charge of every species of particles. These results obtained from the tribocharging process agree with previous work done by Duff and Lacks [26].

Information gathered for the figures shown above was taken at exactly 480 ms, this specific time was chosen because at that point, complete tribocharging was reached, resulting in smaller and larger particles charging negatively and positively respectively.
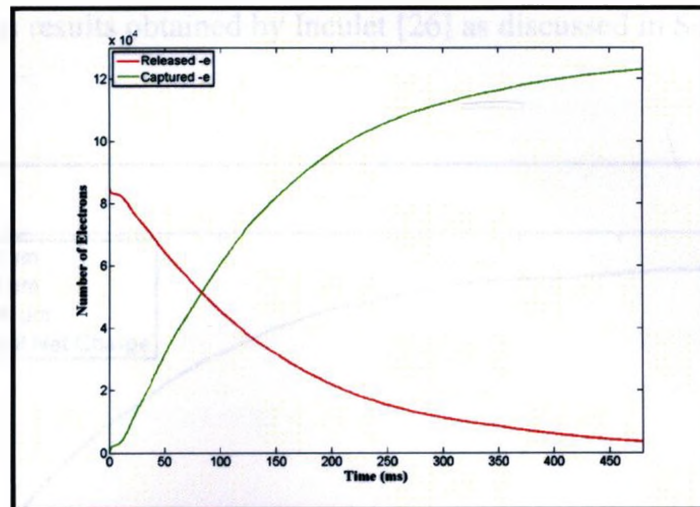
Figure 6.4 60 μm Particles, Red Line - Released Electrons from High Energy States
Green Line - Captured Electrons in Low Energy States
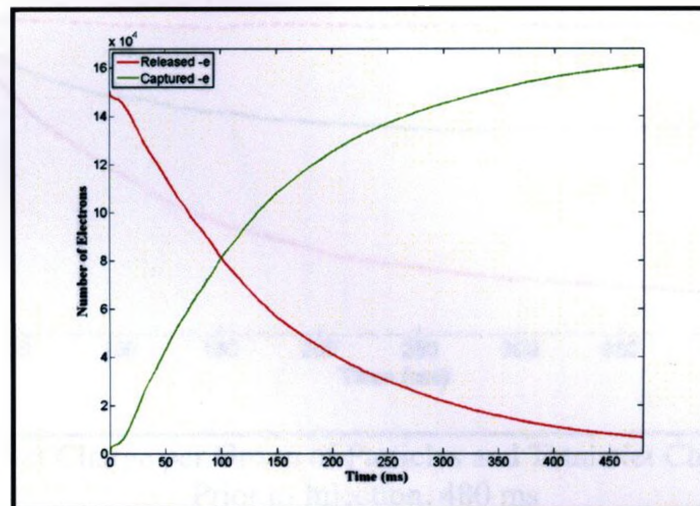
Figure 6.5 80 μm Particles, Red Line - Released Electrons from High Energy States
Green Line - Captured Electrons in Low Energy States
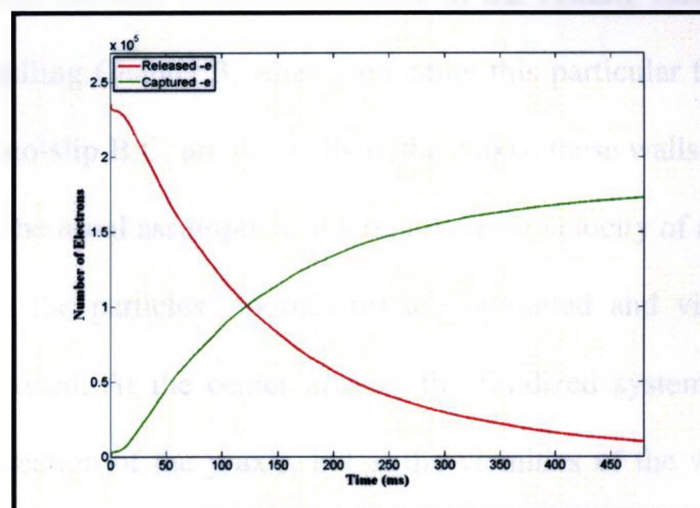
Figure 6.6 100 μm Particles, Red Line - Released Electrons from High Energy States
Green Line - Captured Electrons in Low Energy States

Figure 6.7 confirms results obtained by Inculet [26] as discussed in Section 2.3.
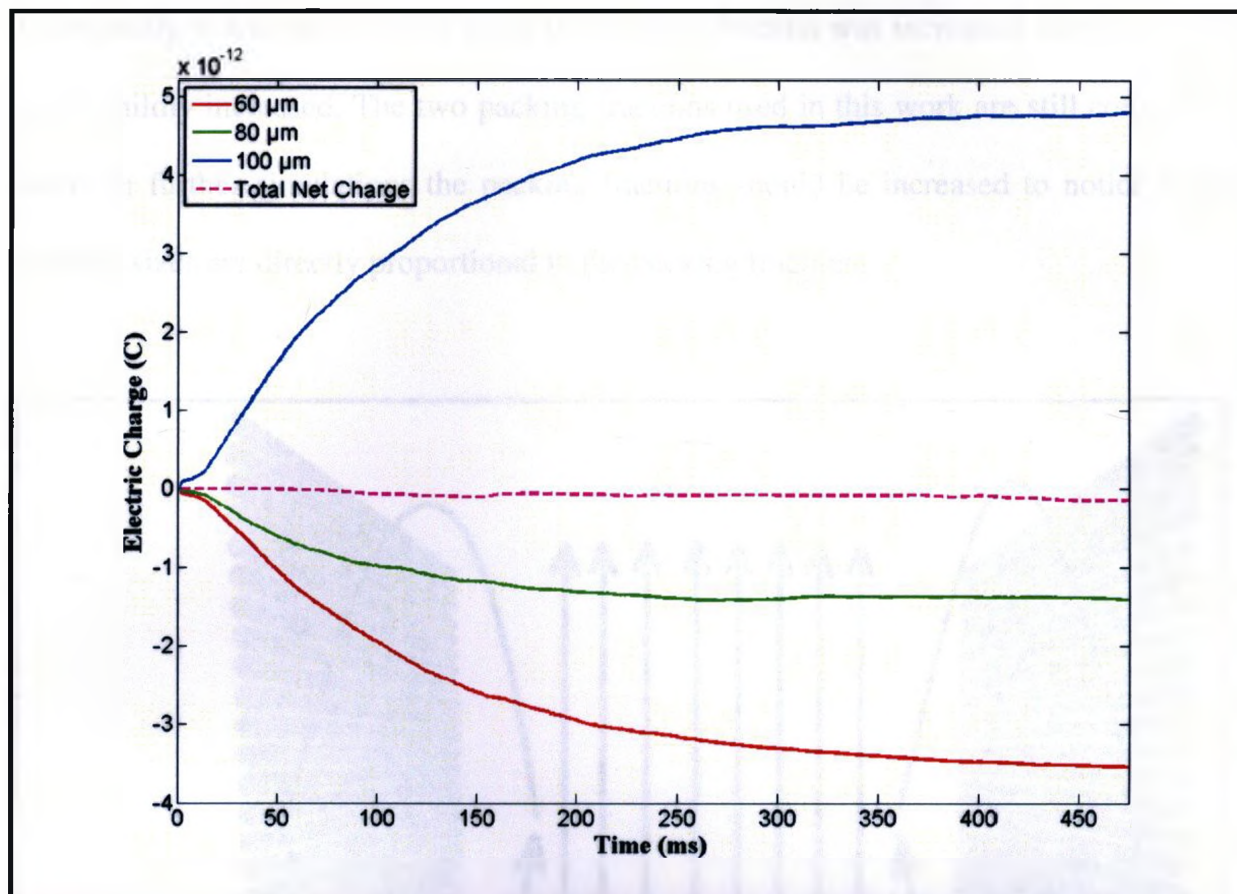
Figure 6.7 Total Net Charge per Group of Particles and Total Net Charge of the System, Prior to Injection, 480 ms

Tribocharging is not the only process occurring in the system, other events are taking place as well. Recalling Chapter 3, when simulating this particular fluidized system, the only bounce-back no-slip B.C. are the walls in the z axis, these walls exert a resistance to the fluid flow and the usual assumption of a relative zero velocity of a fluid next to a wall is assumed. When the particles' coordinates are outputted and visualized, a peculiar phenomenon is noticed. At the center area of the fluidized system, a laminar flow is observed in the direction of the y axis, but at the vicinities of the walls (z axis) this so called resistance effect is noticeable, making the particles close to it to re-circulate in

some sort of vortex near the walls. Figure 6.8 shows a sketch of the flows inside the system. When no particles are present in the simulations, a parabolic flow is perceived. Additionally, it was noticed that when the packing fraction was increased, the size of the vortex mildly increased. The two packing fractions used in this work are still considered dilute. In further simulations the packing fractions should be increased to notice if the vortexes sizes are directly proportional to the packing fractions.
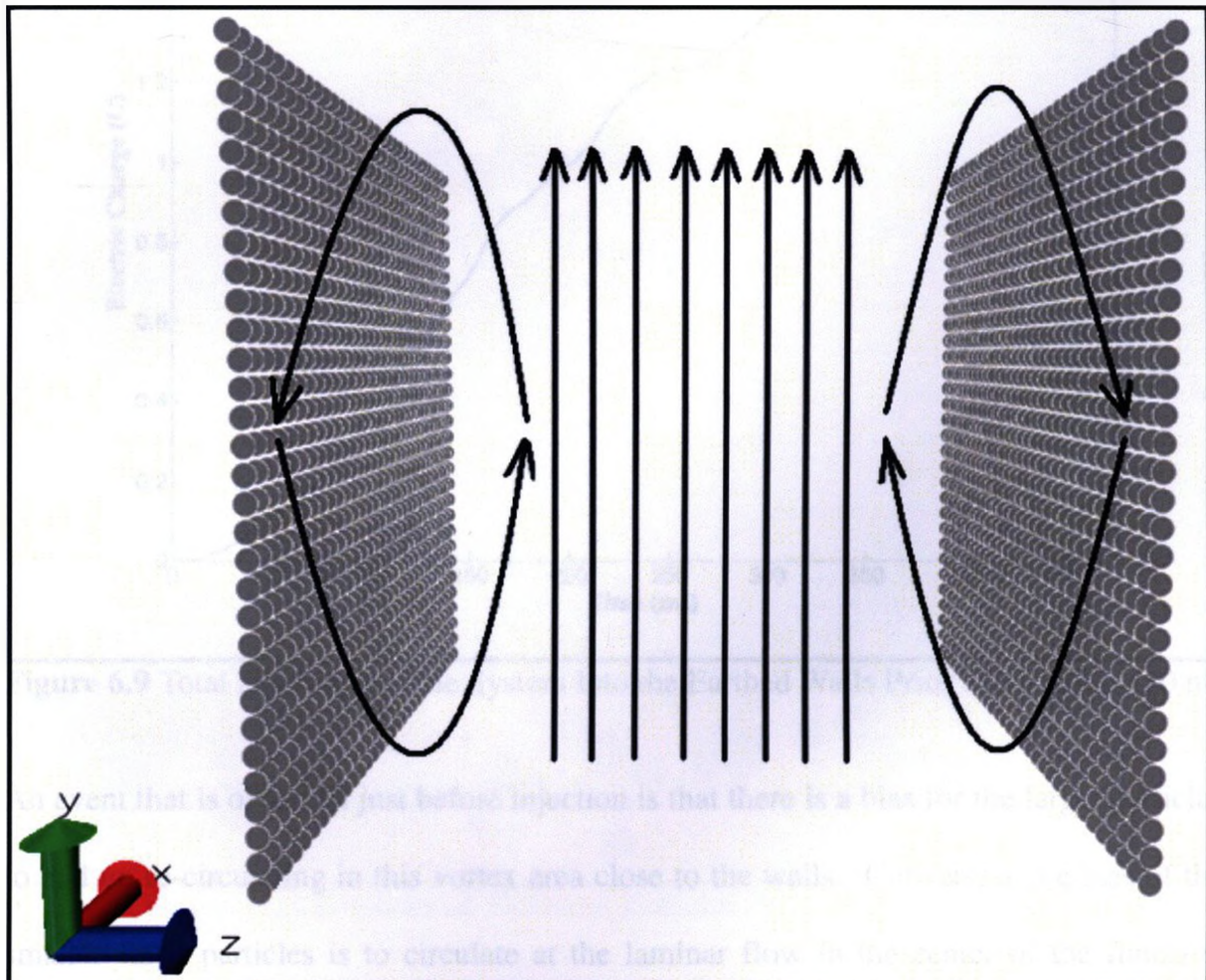
Figure 6.8 Three Flow Areas in the System, Two vortices near the walls, Laminar Flow in The Center of the System

Some of the particles that are trapped in this vortex area may come in contact with the earthed walls, which in turn means that they may eventually discharge. Figure 6.9 shows

the overall discharging of the system into the walls. It can be observed that at the start, very little discharging on the walls occurs; as time evolves more particles reach the walls, hence the discharge increases.
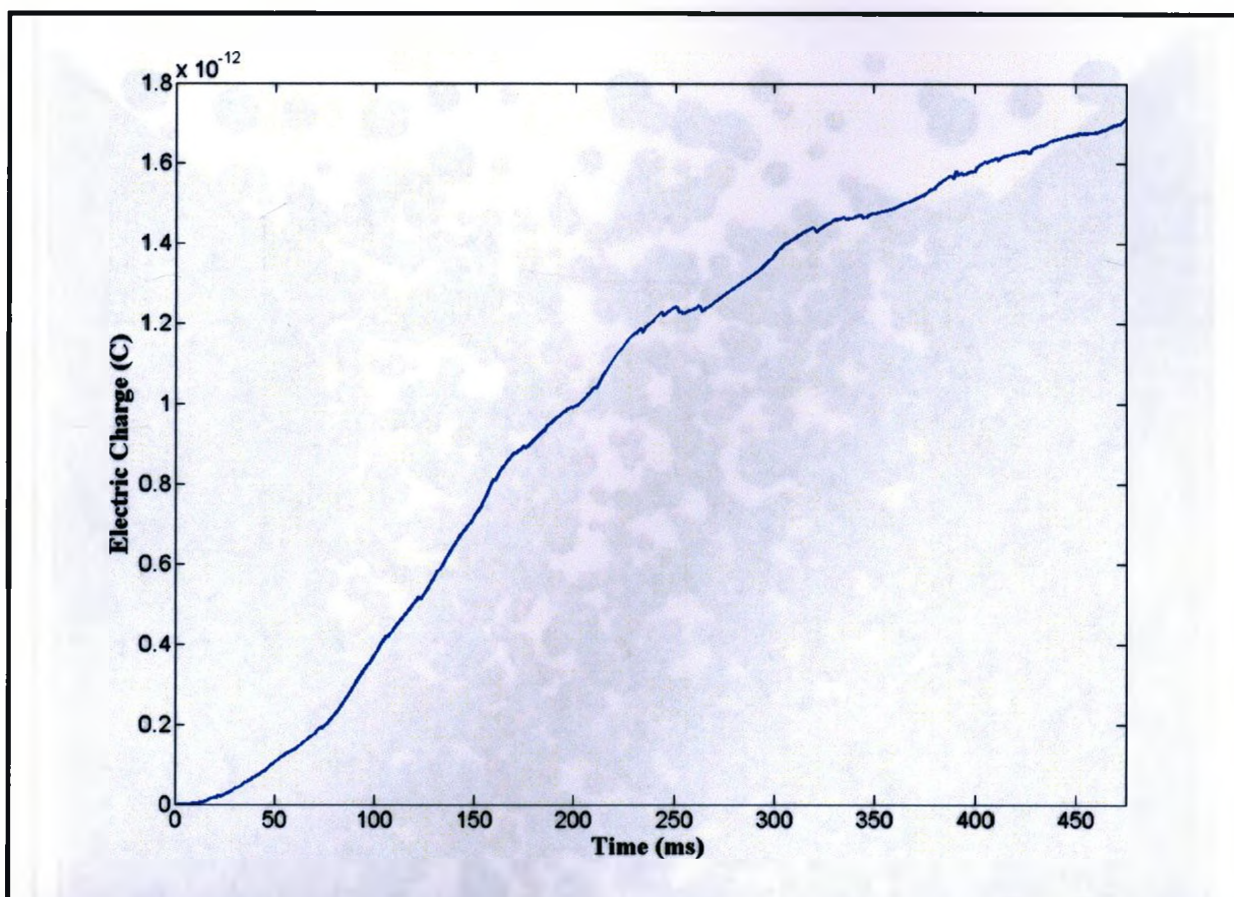
Figure 6.9 Total Discharge of the System Into the Earthed Walls Prior to Injection,480 ms

An event that is observed just before injection is that there is a bias for the larger particles to end up re-circulating in this vortex area close to the walls. Conversely the bias of the smaller sized particles is to circulate at the laminar flow in the center of the fluidized system. Figure 6.10 illustrates this particular phenomenon.

Recapitulating, up to this stage all the events have been explained in depth: after 480 ms all the fluidized particles are fully tribocharged, since the system has a uniform particle

size distribution, the amount of net positive charge is almost equal to the amount of net

negative charge, consequently they cancel each other out. Figure 6.7 shows the total net

charge of system is insignificant up to this point in time. Also at this stage it has been
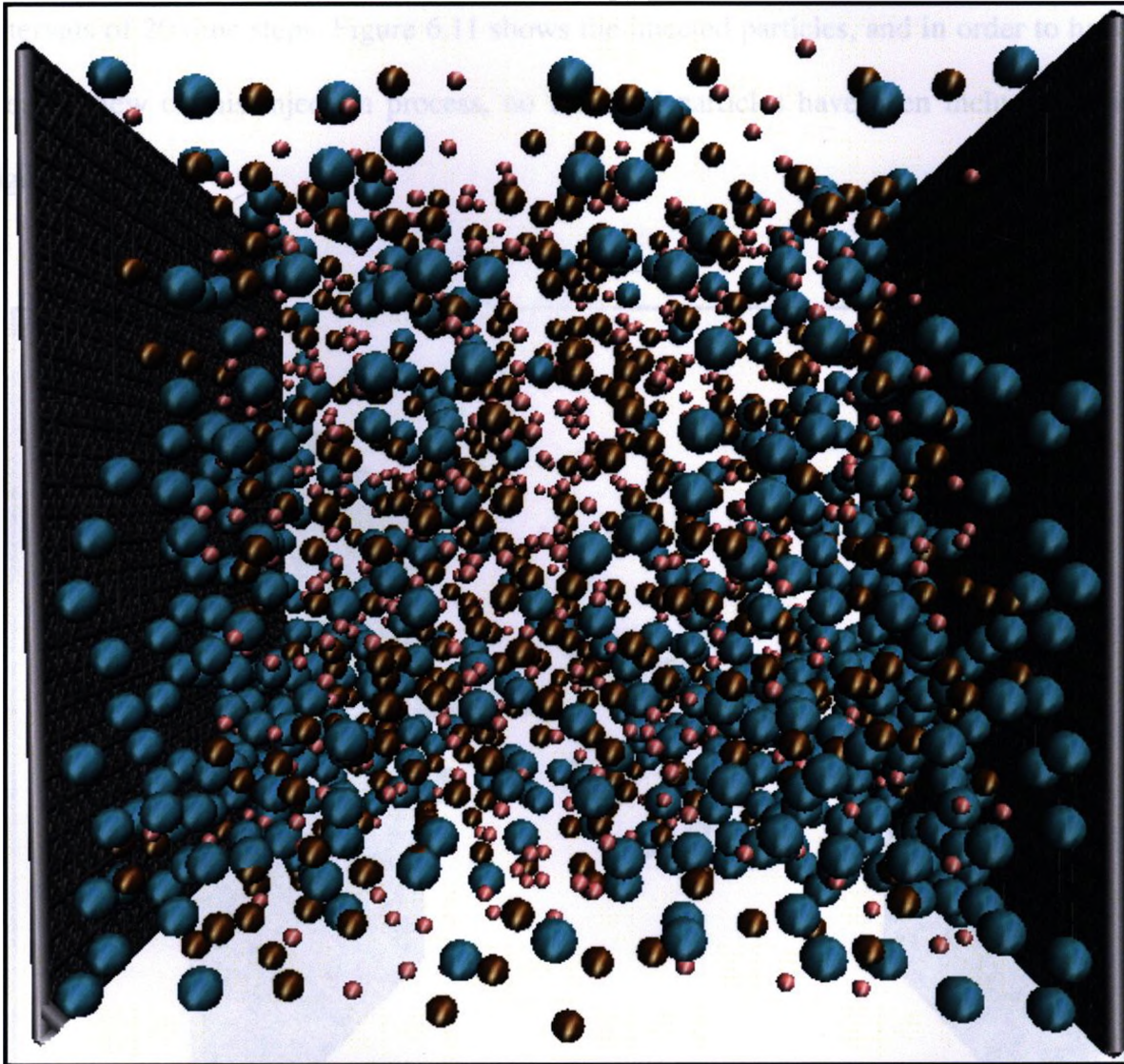
Figure 6.10 Positions of Fluidized Particles Prior to Injection, 480 ms

observed that the majority of larger particles (positive charge) and a minority of smaller

particles (negative charge) wander around in either one of the two vortex areas near the

walls. In the laminar flow area most of the smaller particles flow passively along the y

axis.

6.1.2 During and After Injection (480 – 720 ms)

A larger diameter size of particles (120 μm) with a net positive charge of 10 e-14 C each, are simulated for the injection process. The injection is done through the sides of the solid walls (z axis). For convenience, this is done in groups of 4 particles on both sides at intervals of 20 time steps. Figure 6.11 shows the injected particles, and in order to have a clearer view of this injection process, no fluidized particles have been included in this figure.
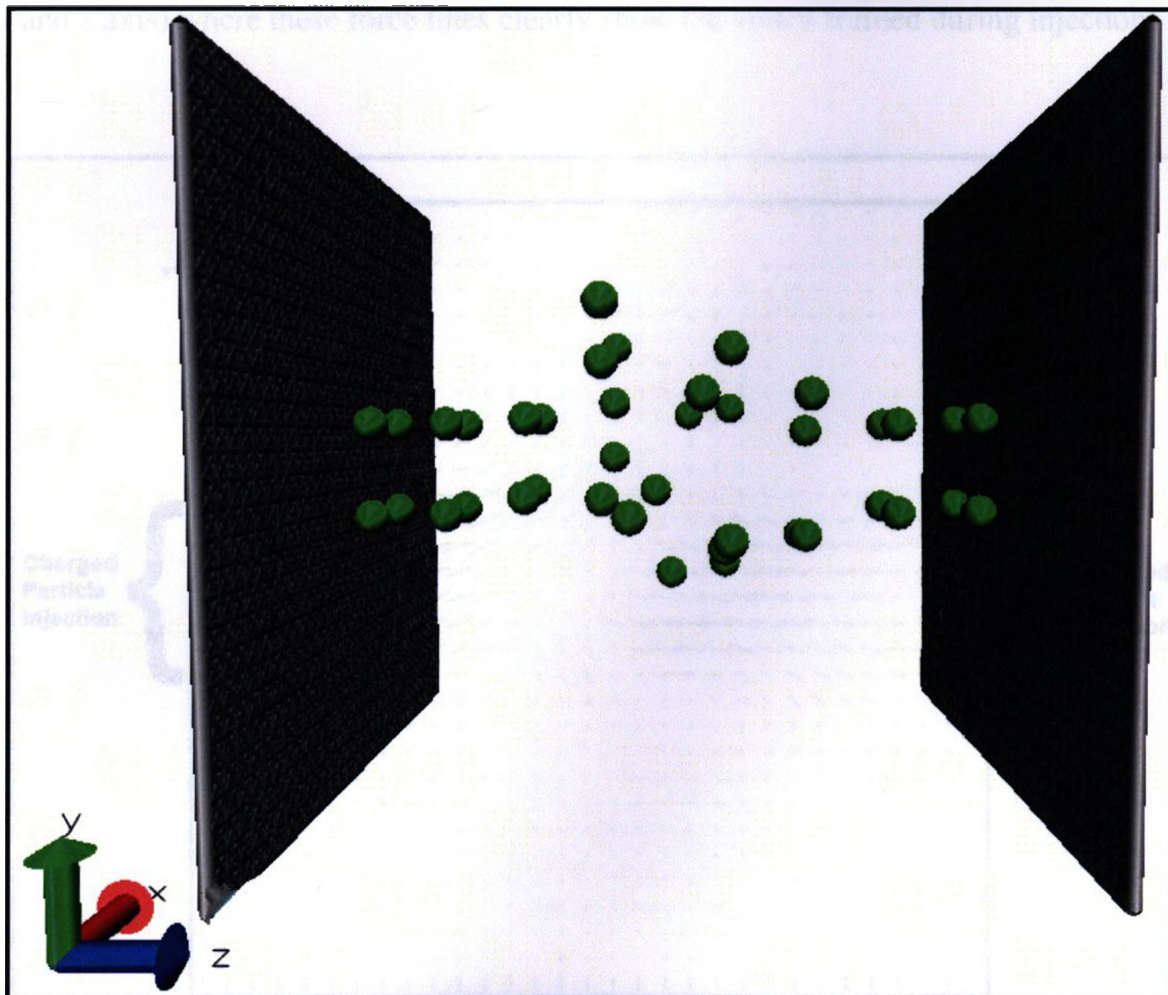
Figure 6.11 Injection of Positively Charged Particles Through each Side of the Walls

For the injection process, the injected particle speed and the air speed injection inlet

values were carefully calibrated to cause the injected particles to reach the middle of the system. As the injection of positively charged particle increases, the total net charge of the system increases significantly. Consequently the electric field inside the system also increases, becoming stronger near the walls. Appendix 1 shows a set of graphs that output the particles' positions, electric field, and electric potential of the system.

In the meantime this injected air flow will produce another vortex effect in the vicinities of the walls this time perpendicular to the y axis. Figure 6.12 shows the force lines in 2-D (y and z axis) where these force lines clearly show the vortex formed during injection.
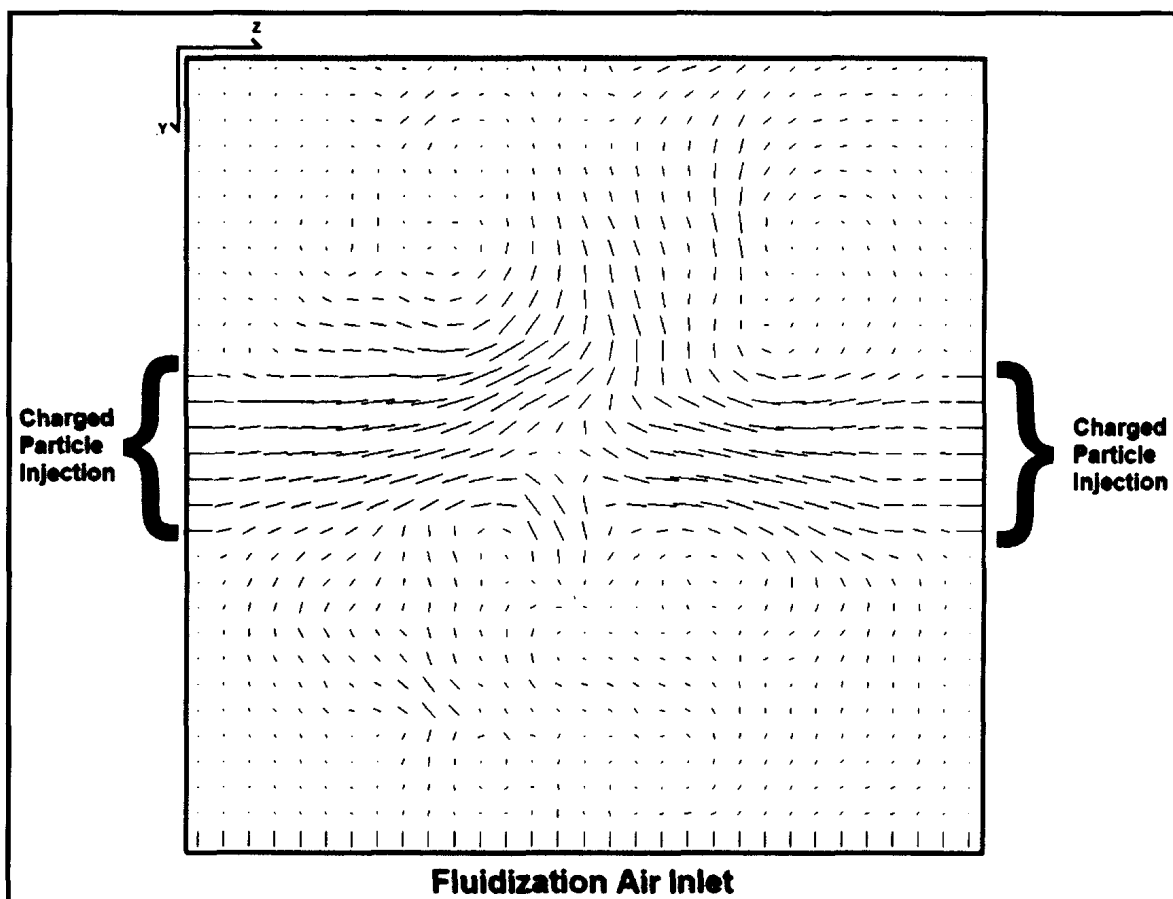
Figure 6.12 Vortex Located in the Surroundings of the Injection Orifices (z Axis), Cross-Section at x=15 (Centre)

These two effects: the increase of the positive electric field near the walls and the perpendicular vortex effect, are responsible for getting the particles that were previously near the walls (mostly the positively charged particles) to be pushed into the walls by the flow as the walls attract them, respectively. Figure 6.13 shows how this can be better understood by graphing the change of the net charge for every particle group in the moment of injection.
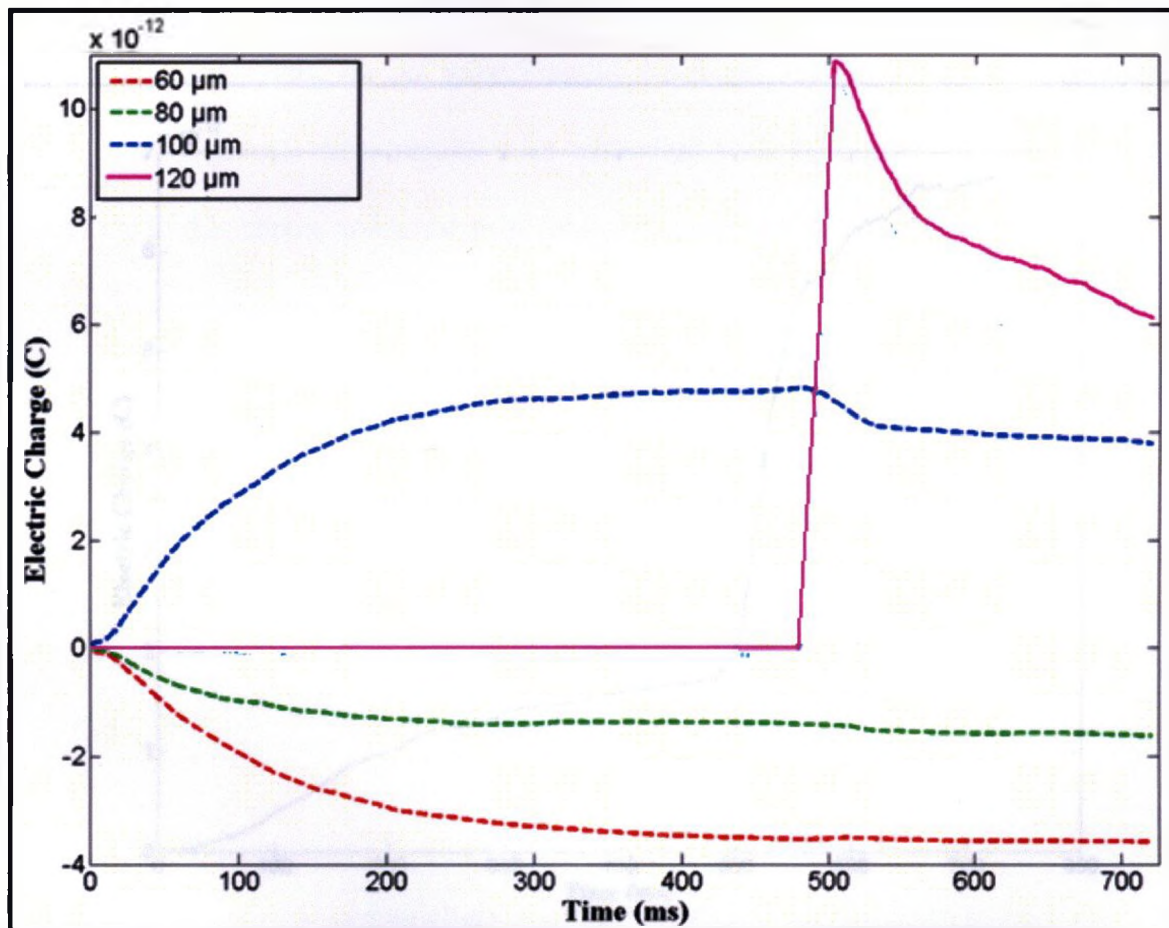
Figure 6.13 Average Total Net Charge Per Group of Particles, and Total Net Charge of the System

It can be observed that as soon as the injection starts, the total net charge of the larger particles drastically drops, while the total net charge of the smaller particles which were higher in the middle of the system, did not undergo any major changes, this confirms that

most of the particles that were wandering near the walls were larger particles and as soon as they got attached to the walls they started discharging. Figure 6.14 shows how the discharging process into the earthed walls drastically increases almost right after injection starts. Looking closely at Figure 6.13, it can be noticed that when injection commenced (time 480 ms) there was an instant total net charge drop on all the groups of particles. The algebraic addition of all the charge drops account for the discharging into the walls pictured in Figure 6.14.
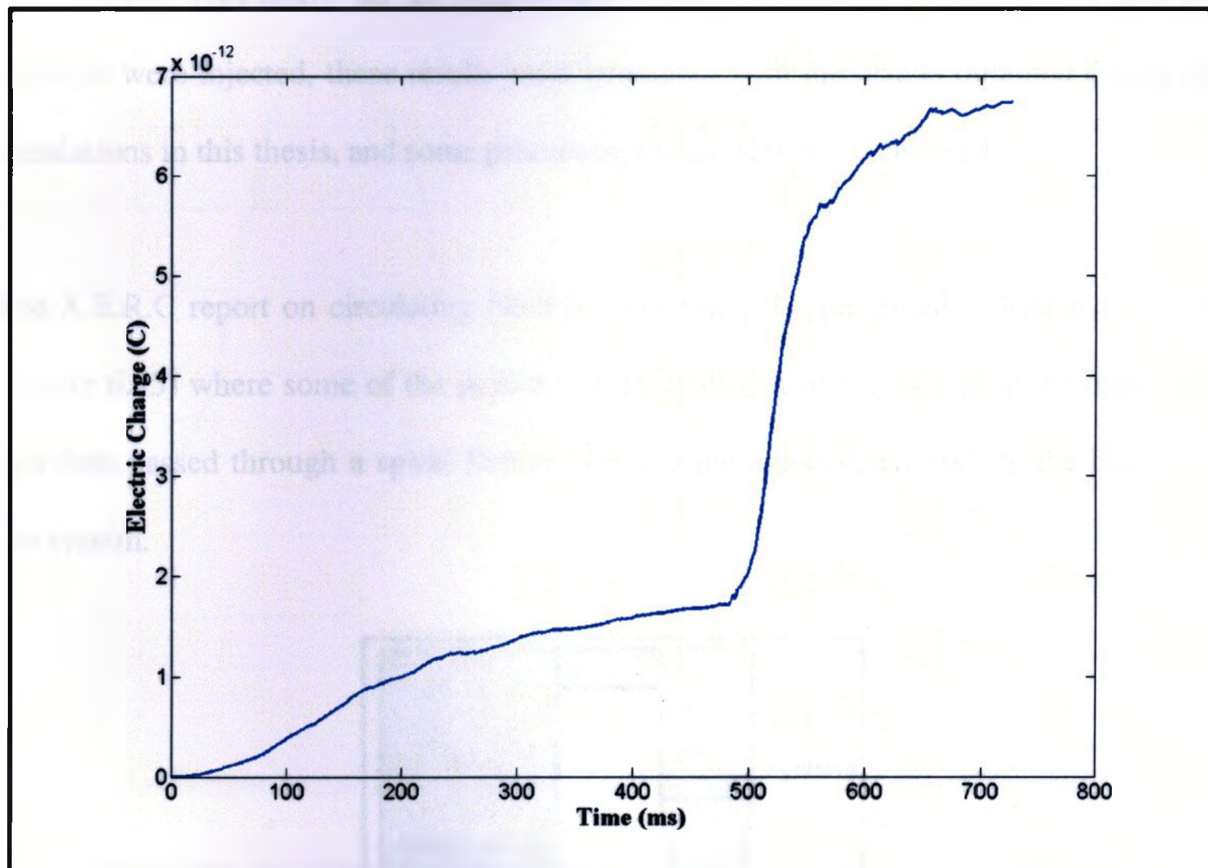
Figure 6.14 Total Discharge of the System into the Earthed Walls

Well after injection is done, the injected particles flow slowly in the middle of the system (laminar flow). The electric field intensity near the walls still has a considerable value (Figures in Appendix 1). Due to this strong electric field near the walls and the high

interaction between these injected particles and the fluid, the injected charged particles are attracted and pushed into the solid walls of the system (z axis). They will accumulate there on top of the fluidized particles until attaining critical thickness and then reach air breakdown level.

6.2 Past Experimental Results

A team led by Dr. I.I. Inculet from the Applied Electrostatic Research Center (A.E.R.C.) [71] worked previously on an experimental fluidized system where highly charged particles were injected, these results were compared with the results obtained during the simulations in this thesis, and some promising similarities were observed.

The A.E.R.C report on circulating fluidized systems [71], presented a fluidized system, (Figure 6.15) where some of the particles were taken out of the system in the upper part and then passed through a spiral Teflon tube and then re-injected back to the bottom of the system.
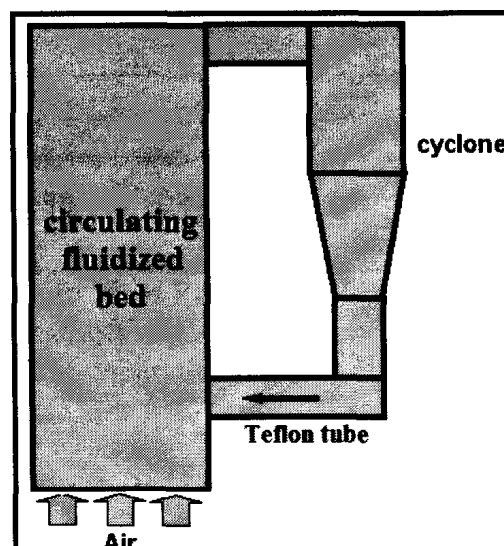
Figure 6.15 Sketch of the Re-Circulating Fluidized System Employed in the A.E.R.C.

The recirculation of the particles through a Teflon tube charged them positively due to the difference of work functions [13]. Consequently the injected particles at the bottom have a high positive charge compared to the value they had when they were taken out of the system. This means that after injection, an increase on the total net charge is expected in the system. A resultant graph of this experiment presents the charge to mass ratio plotted as time evolves (Figure 6.16).
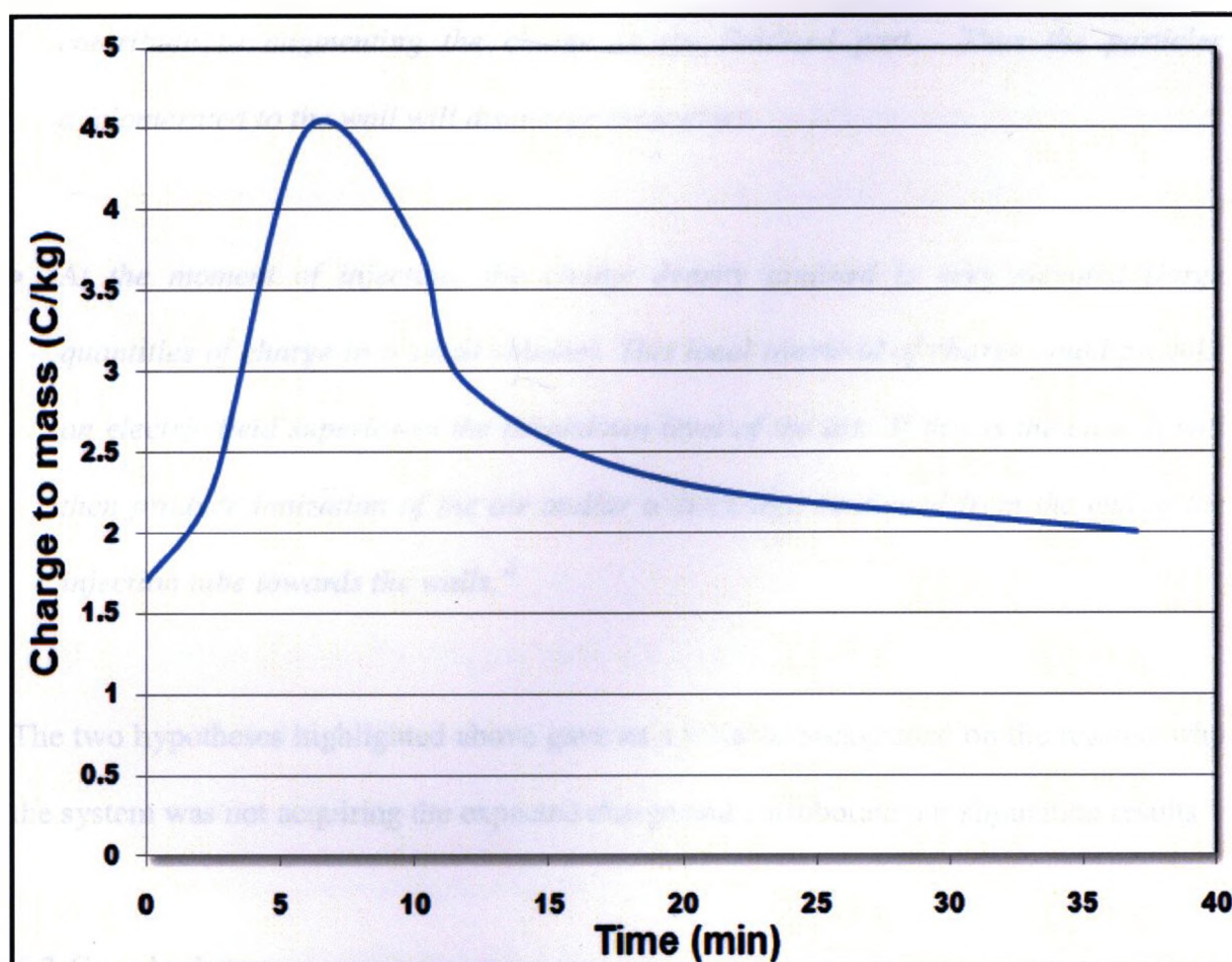
Figure 6.16 Charge to Mass Ratio of the System Evolving in Time [71]
(Taken from "Study of the fall-off of electrically charged Rilsan powder coatings during the curing operations", By A.E.R.C. , (2004))

According to the Figure 6.16, the charge to mass ratio increases, reaches a maximum and then gradually starts fading away. The authors of this report presented possible

explanations to this phenomenon:

"To explain why the bed does not obtain more elevated levels of net charge, two hypotheses have been proposed:

- *Charged particles under the effect of the electric field, will glue themselves to the walls of the bed. These particles therefore do not stay in fluidization, nor do they contribute to augmenting the charge in the fluidized part. Thus the particles agglomerated to the wall will discharge themselves.*

- *At the moment of injection, the charge density attained is very elevated (large quantities of charge in a small volume). This local overload of charge could provoke an electric field superior to the breakdown level of the air. If this is the case, it will then produce ionization of the air and/or a discharge continued from the end of the injection tube towards the walls."*

The two hypotheses highlighted above gave us a reliable background on the reasons why the system was not acquiring the expected charge and corroborate our simulation results.

6.3 Conclusions

The simulation of a fluidized system taking into account the Aerodynamic and electrostatic effects has uncovered some of the key phenomena that take place in such a system. As it was stated in the first chapter, the main objective of this work was to

simulate a fluidized system where charged particles are injected at a specific time after fluidization. Once the particles were injected the overall charge was expected to increase; to explain the missing charge after injection, two hypotheses have been developed from the results obtained.

I.   Once the system has been fully fluidized and tribocharging stabilizes, a majority of the larger particles tend to circulate closer to the walls; this can easily be understood under the principles of sedimentation, which state that different size particles that are in suspension tend to get close to the solid walls of the container as the particles are heavier. This basic principle is well observed in these simulations, where larger diameter particles get closer to the solid walls (z axis), conversely to the smaller particles which are flowing linearly at the center of the system (Figure 6.10). Some of these large particles come in contact with the earthed walls where they get gradually discharged.

II. When electrically charged particles are injected into the system, the electric field in the whole container increases, since the walls have potential zero, the electric field close to the walls is very high, therefore the tribocharged particles (mostly large positively charge particles) that were wandering close to the solid walls (z axis), get strongly attracted by them due to the electric force (Equation 5.17). Also the injection inflow starts a vortex which is perpendicular to the solid walls (z axis), generating a drag force that influences the trajectory of the particles.

III.   Once the injected particles are in the system, the electric field remains high

near the walls, hence the electric force between the walls and the injected

charged particles is strong, and consequentially some of the injected particles

(the ones closer to the walls) are attracted by both solid walls (z axis). Once

attached, the discharging process continues.

These three events contributed to elaborate the hypothesis of why the total net charge

fades away and does not reach the desired values, and it can be graphically explained

as seen in Figure 6.17. It can be seen that as injection occurs (480 - 510 ms), the total

net charge of the system increases, but according to Figure 6.17, the total net charge

of the system does not increase up to the injection level. The second point of this

section states that larger particles get attached and discharged in the walls at the same

time that injection occurs, this explains where the disappearing charge goes. After

injection (510 - 720 ms), the remaining injected particles get pushed into the solid

walls (z axis) by the flow as the walls attract them.
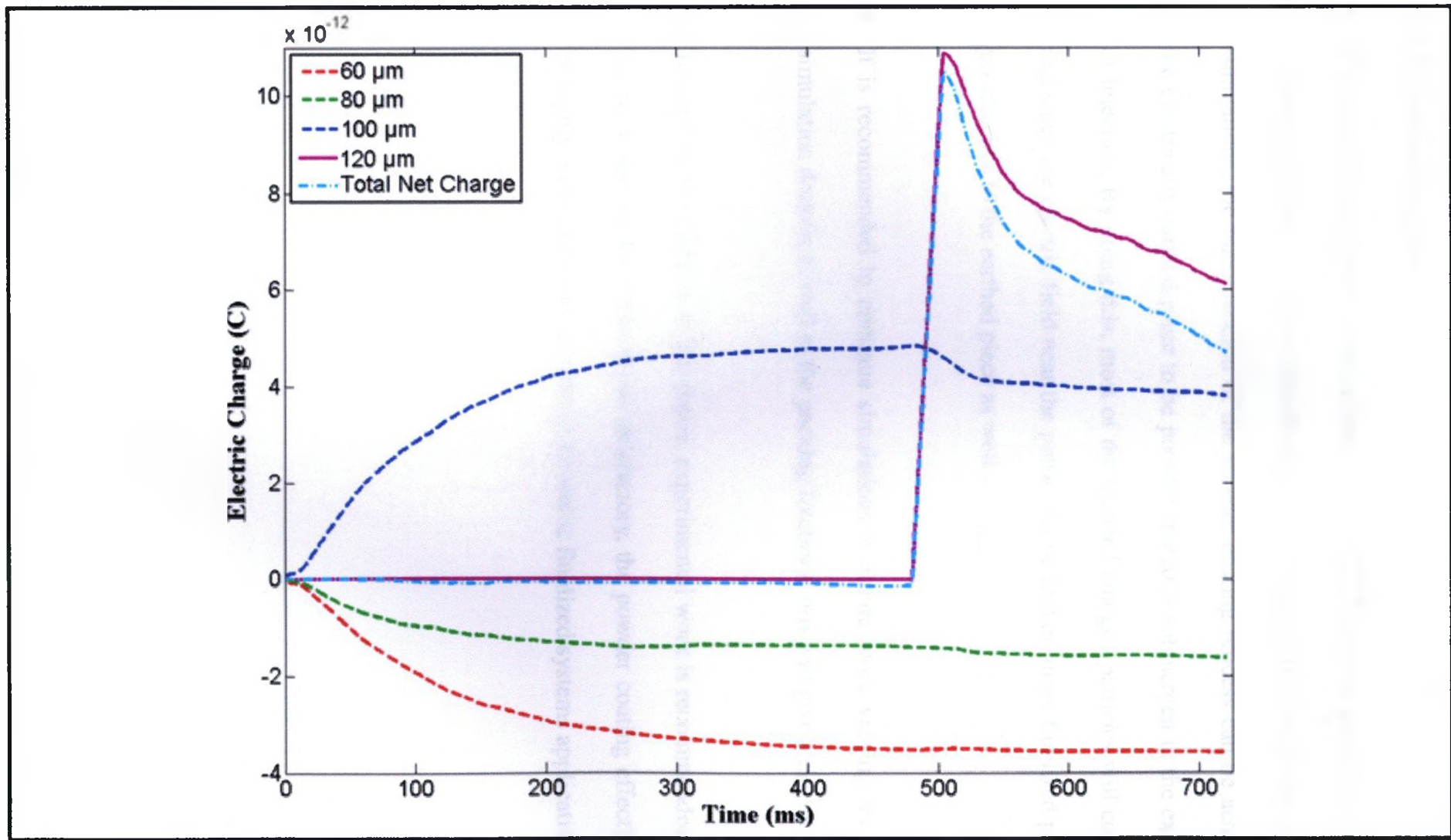
Figure 6.17 Average Total Net Charge per Group of Particles and Average Total Net Charge of the System

6.4 Recommendations

- The current project was aimed to find a way to obtain a better powder coating and the proper conditions to achieve this objective. According to the results obtained in these simulations, the maximization of the powder coating process can be achieved when the electrically earthed piece to be powder-coated is submerged in the exact moment of injection. By doing this, most of the injected charged particles will coat the piece and since the electric field near the piece will be higher, more fluidized particles will get attached to the earthed piece as well.

- It is recommended to continue simulations in future work varying the size of the simulation domain as well as the packing fractions; this will give a clearer insight.

- To confirm the findings in this thesis, experimental work is recommended in the near future. If the results obtained are satisfactory, the powder coating effectiveness may be highly increased in most of the electrostatic fluidized systems applications.

Appendix 1

Simulations Graphs

The next few pages present 3-D snapshots of the particles' trajectories visualization, and 2-D (y-z axis, cross-section in axis x=15) contour plots of the electric potential and electric field intensity for a particulate system with packing fraction 0.18, starting at 0 time step up to 15,000 time step (0 - 720 ms). The snapshots were taken every 24 ms, with a total of 30 snapshots. Table 3.2 in Section 3, indicates the particles' quantity and color during simulations.

0 ms:

24 ms:

Electric Potential   V

Electric Potential   V

Electric Field Intensity V/m

Electric Field Intensity V/m
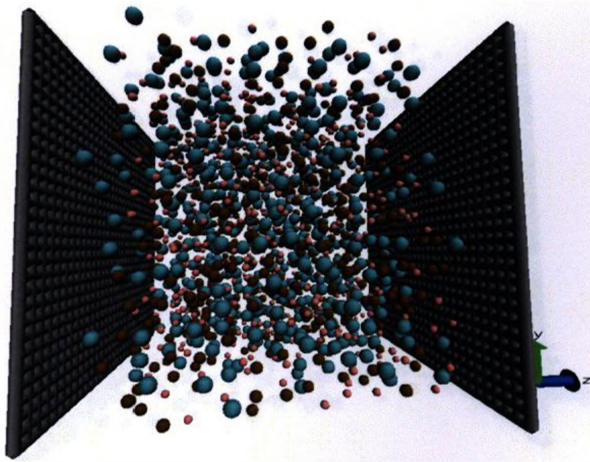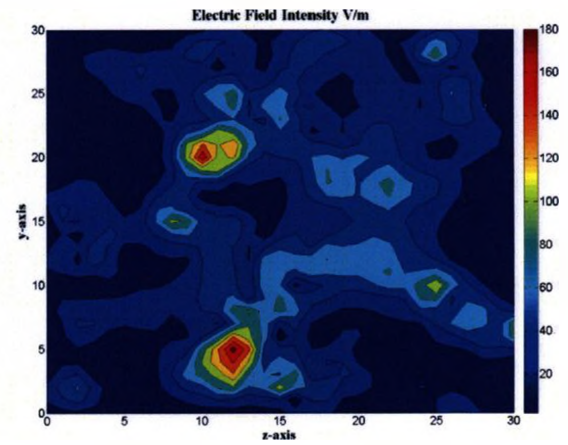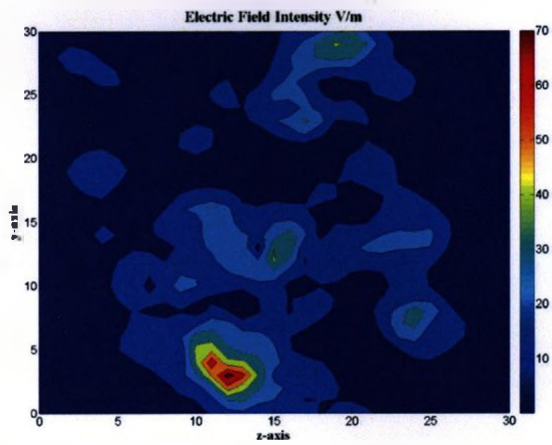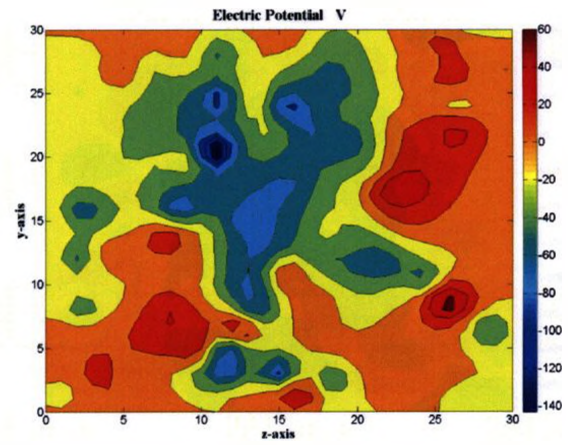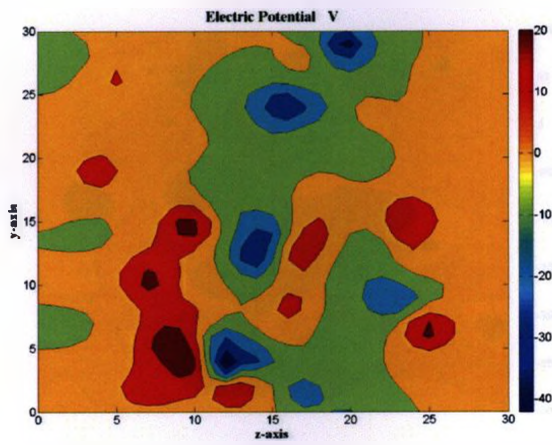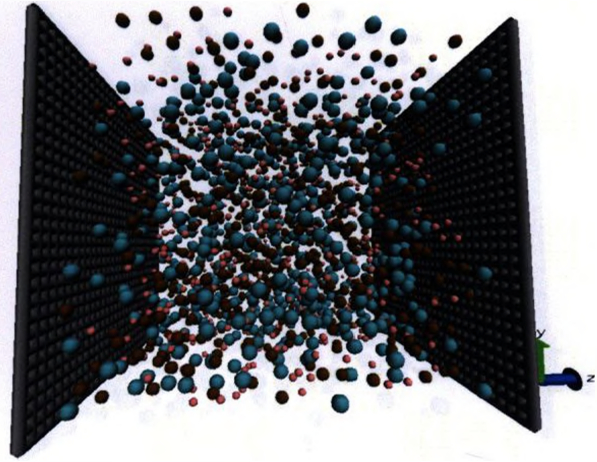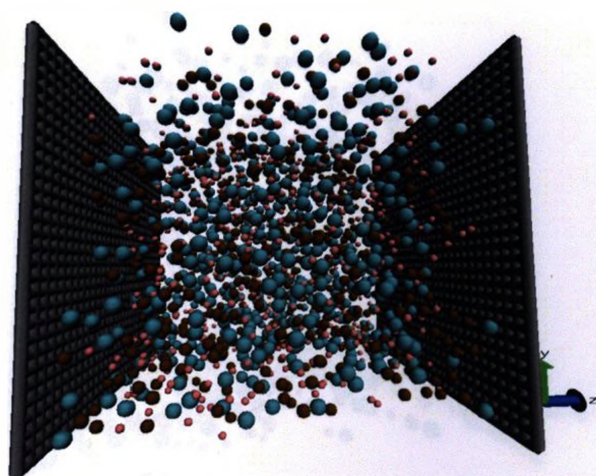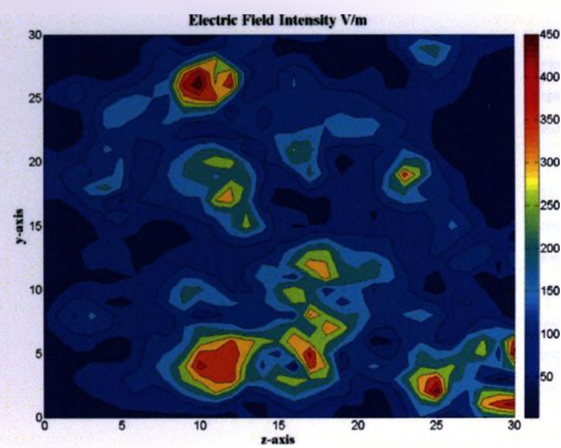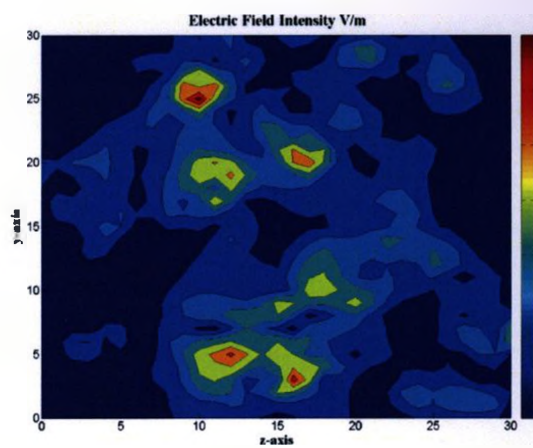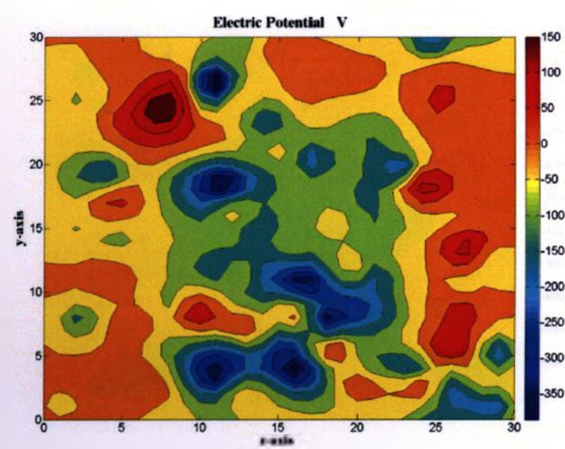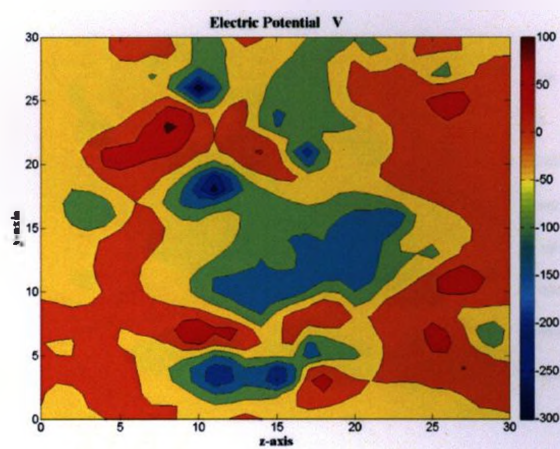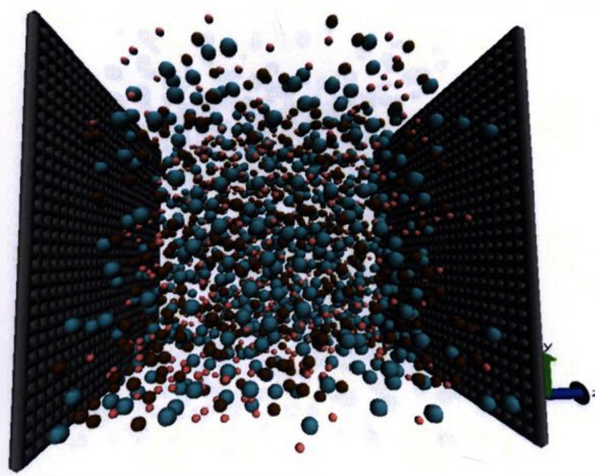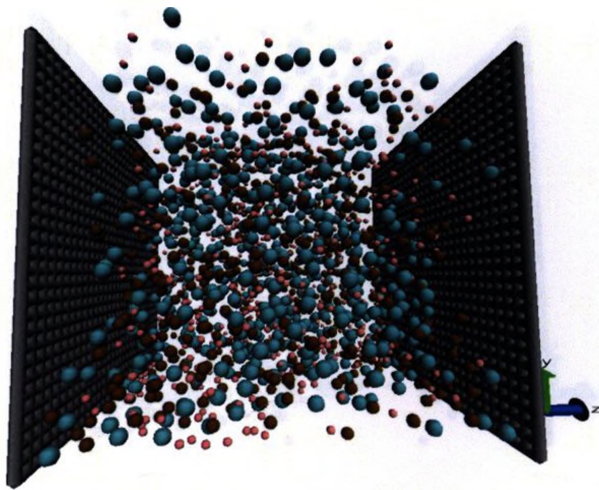
48 ms:

72 ms:

96 ms:

120 ms:
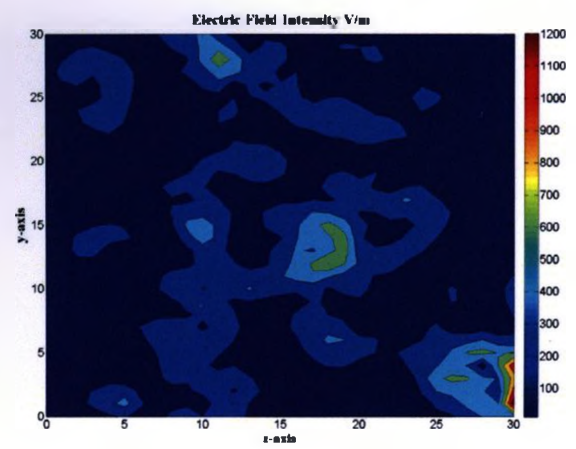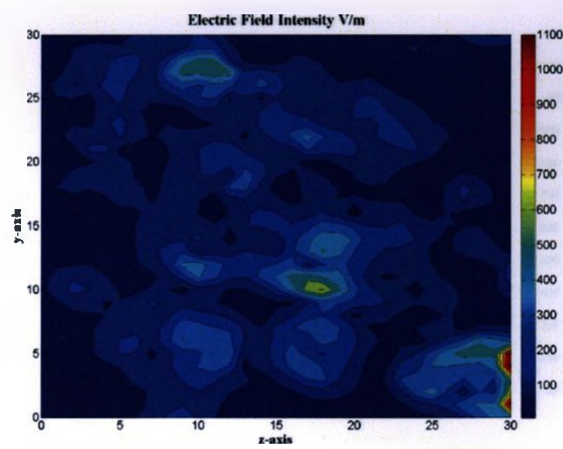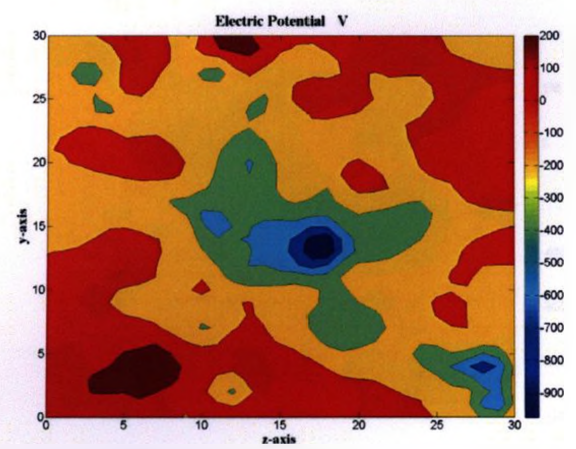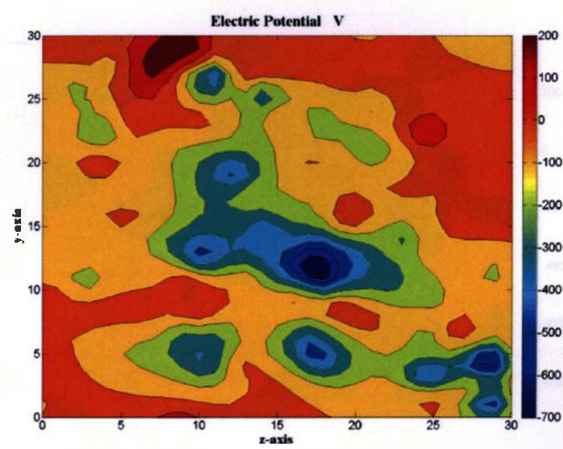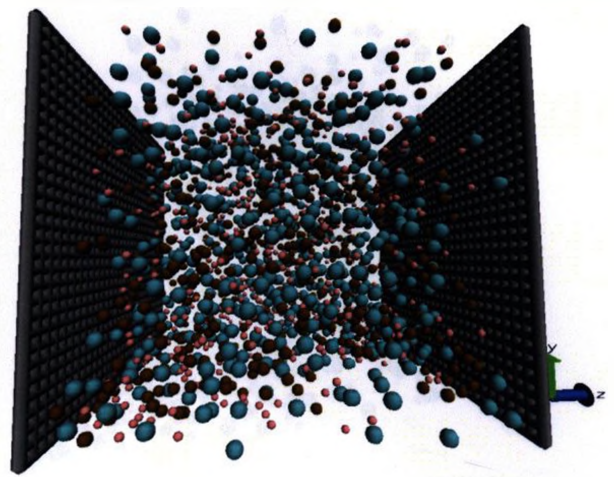
144 ms:
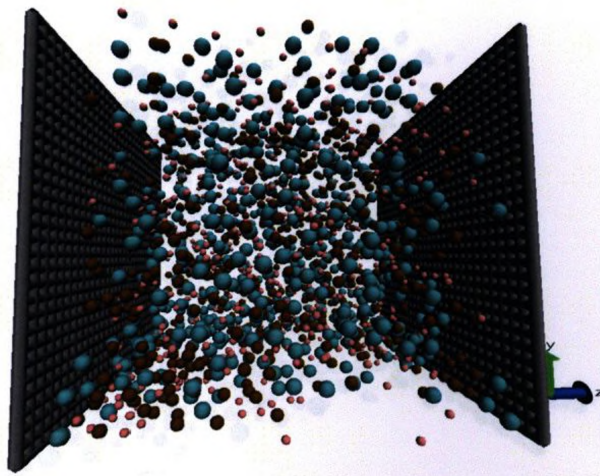
168 ms:
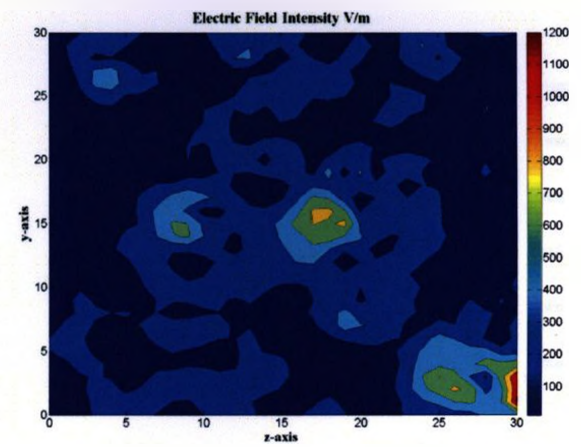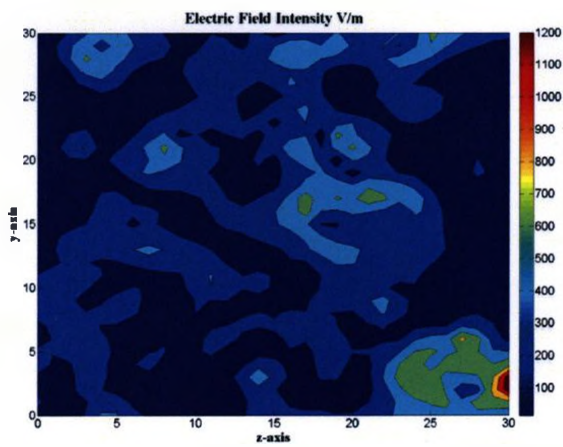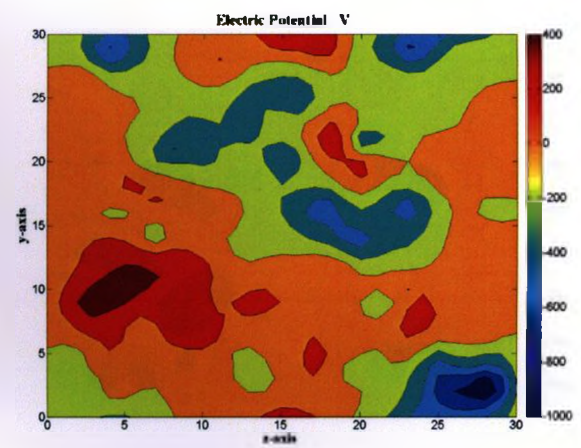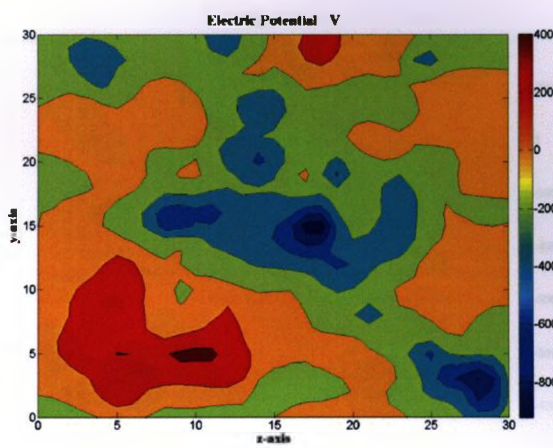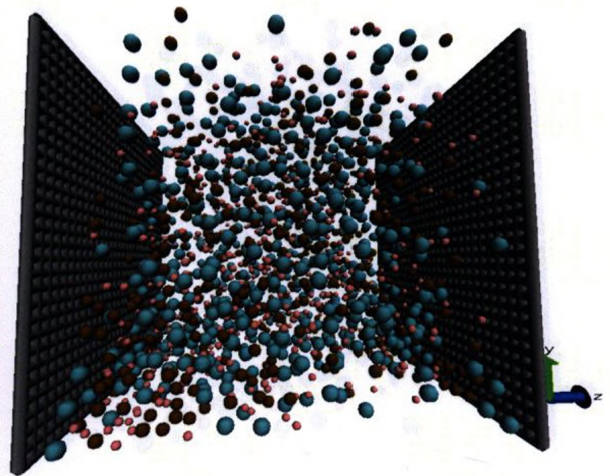
192 ms: **216 ms:**
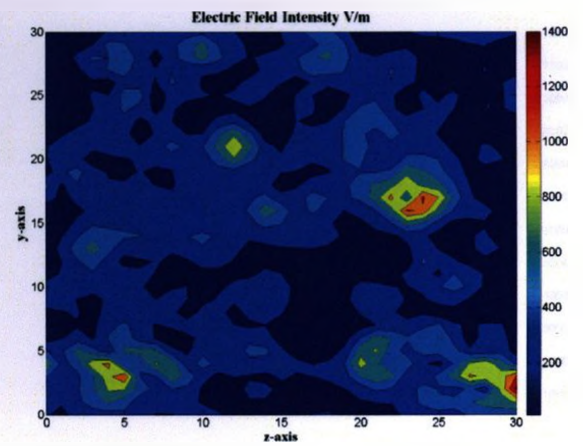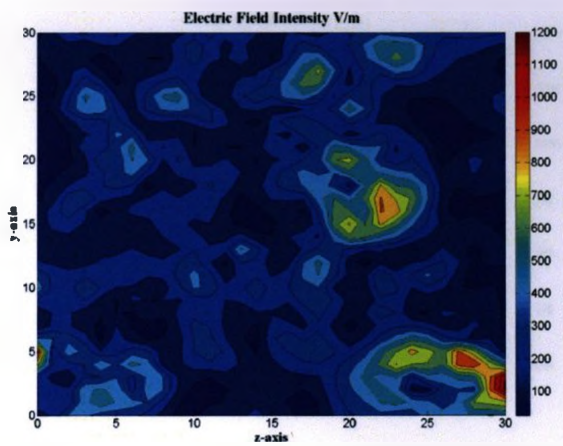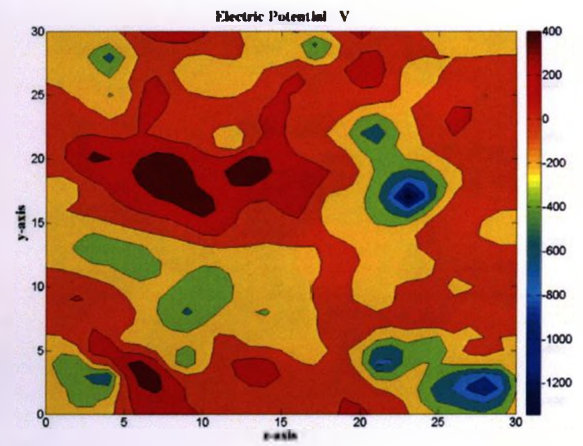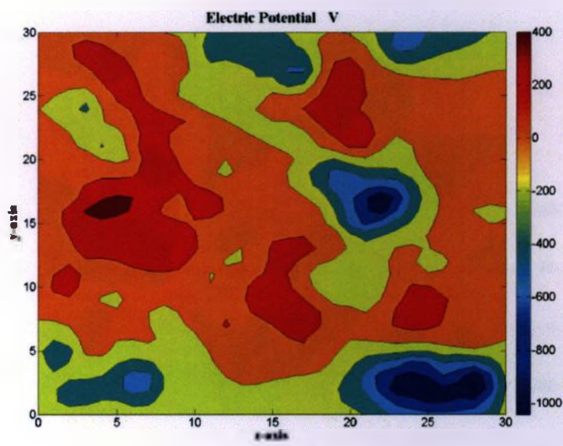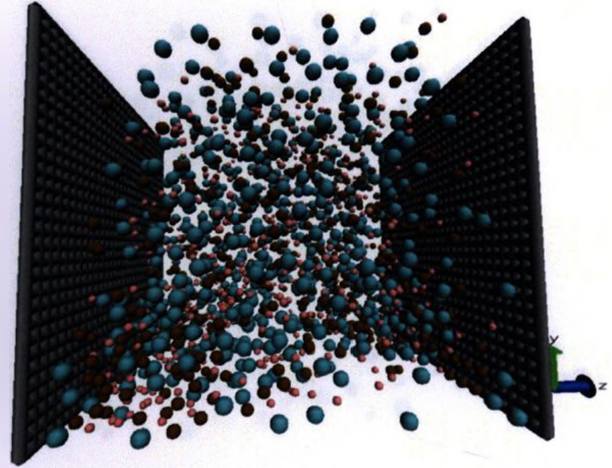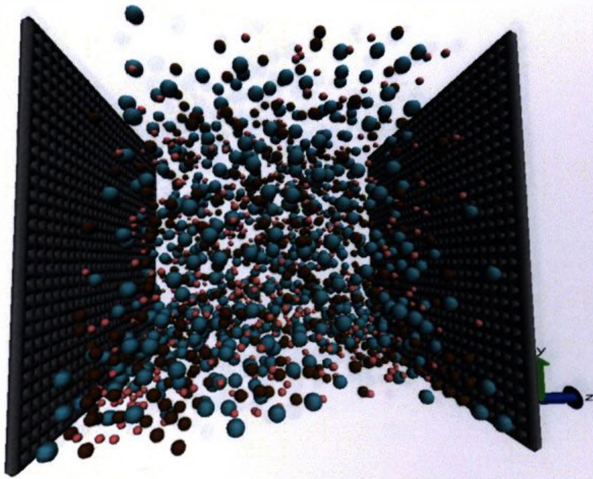
240 ms:
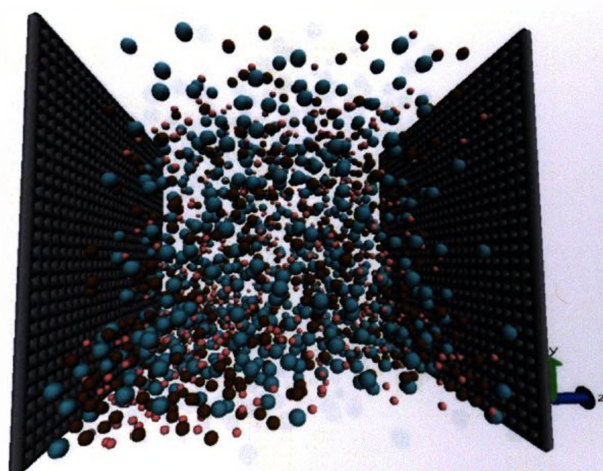
264 ms:

288 ms:

312 ms:

336 ms:

360 ms:

Electric Potential V

Electric Potential V

Electric Field Intensity V/m

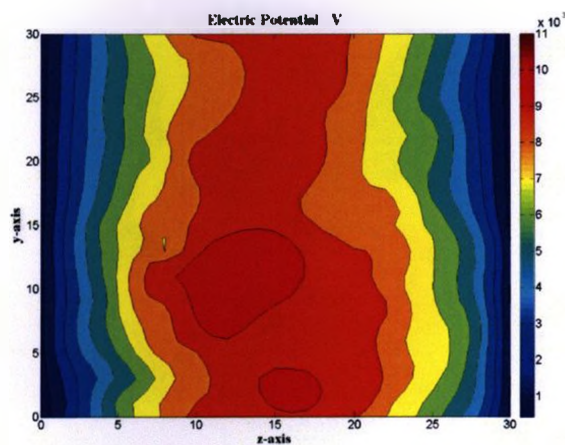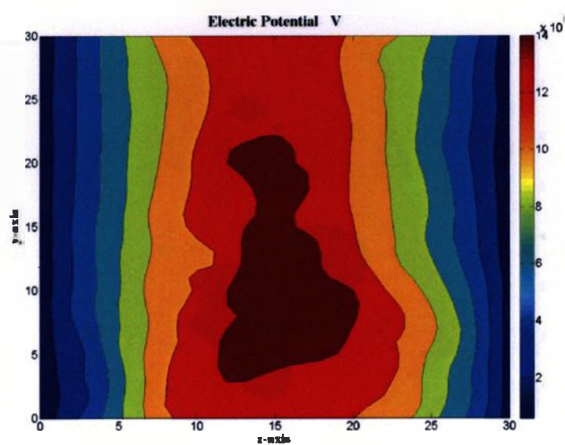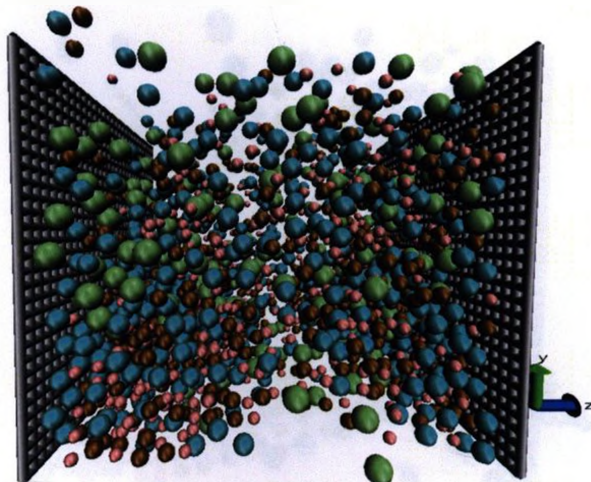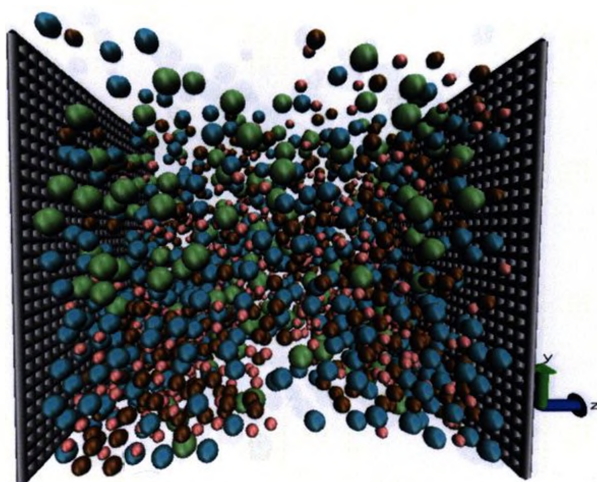Electric Field Intensity V/m
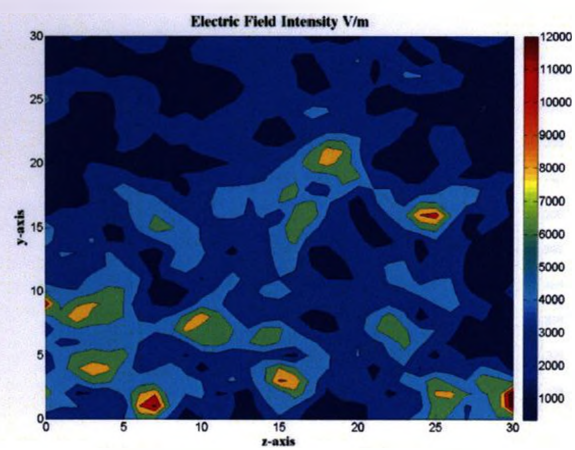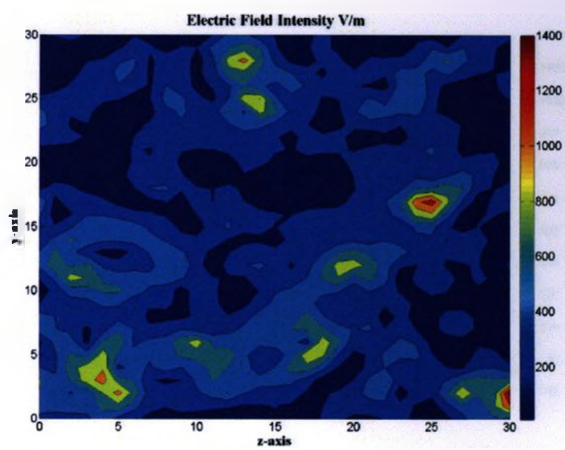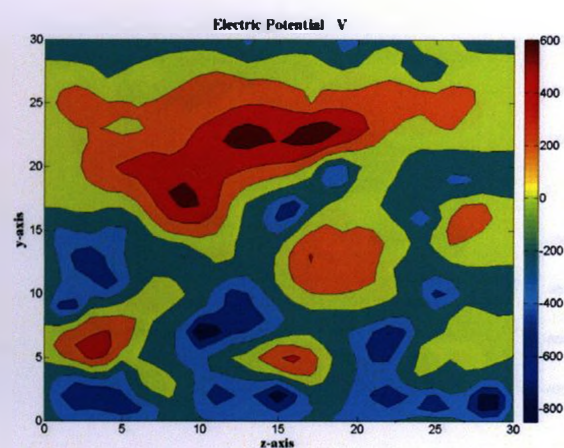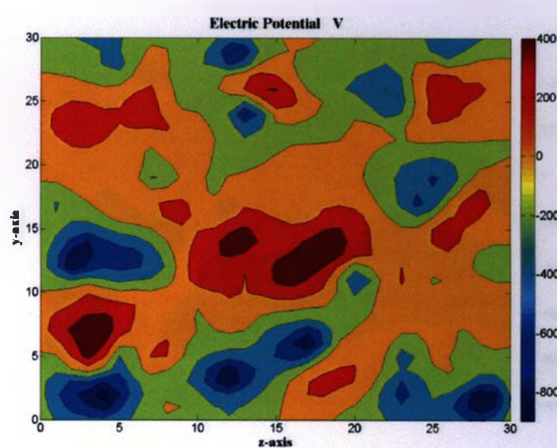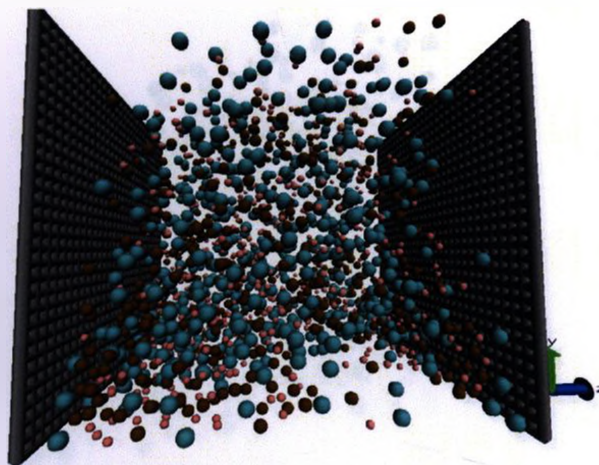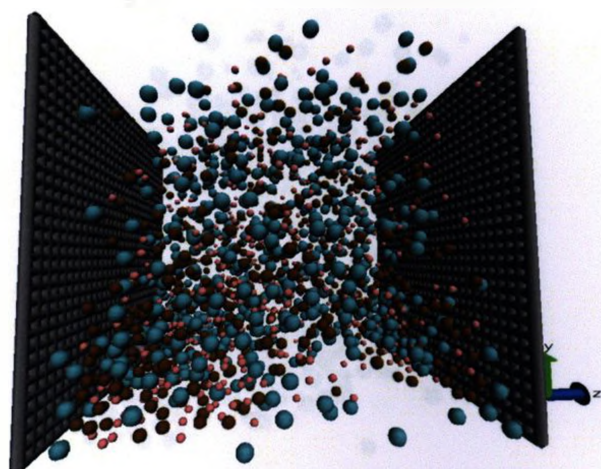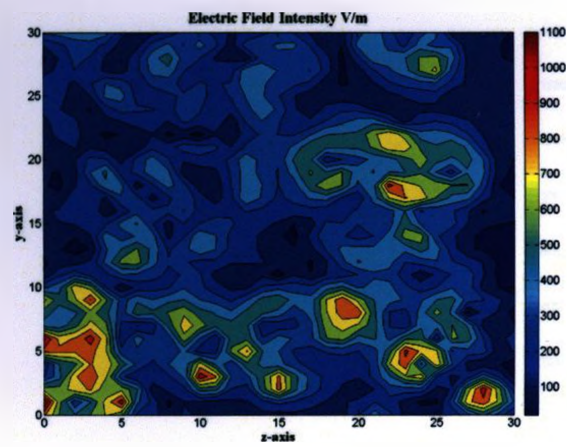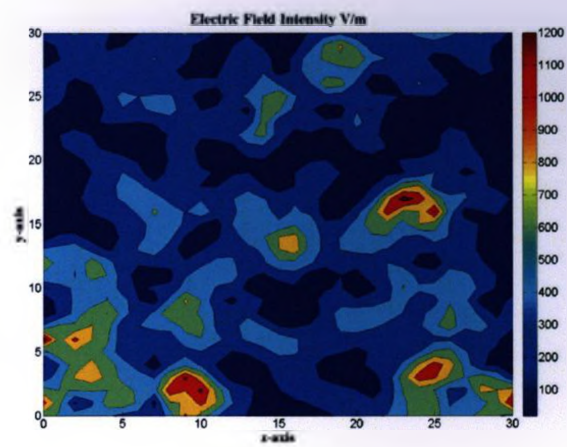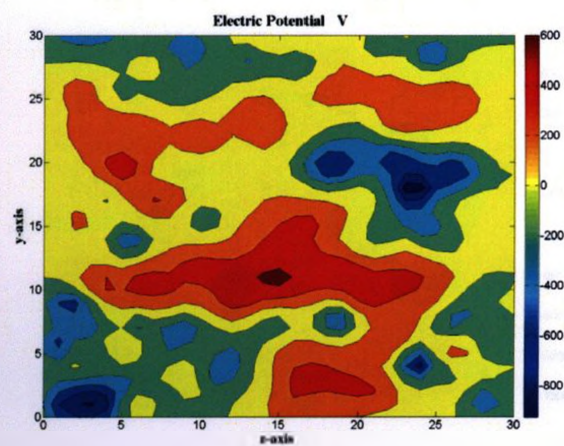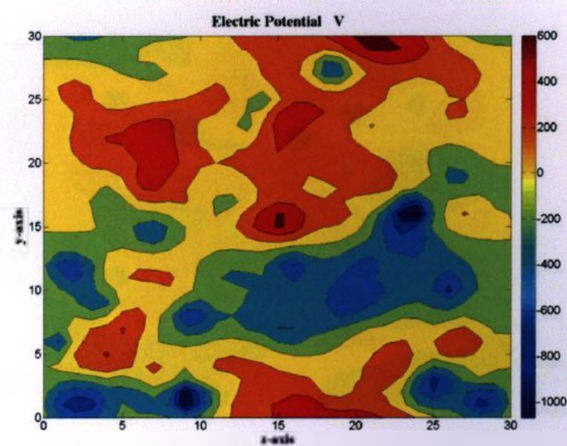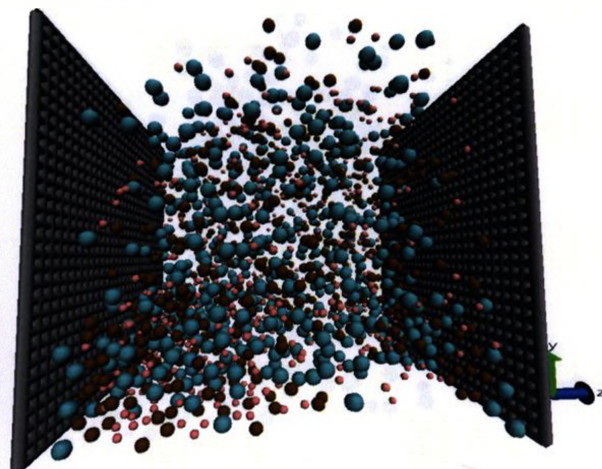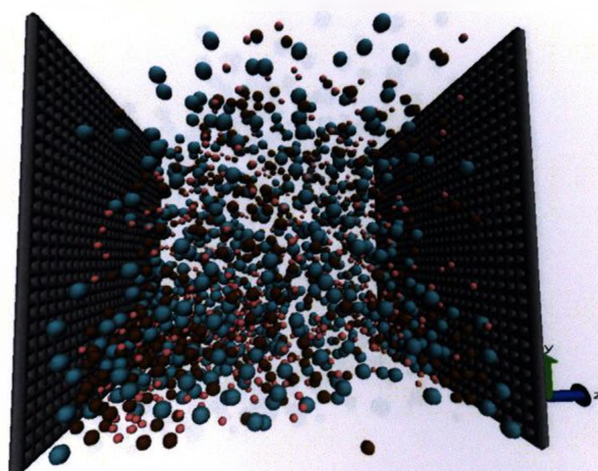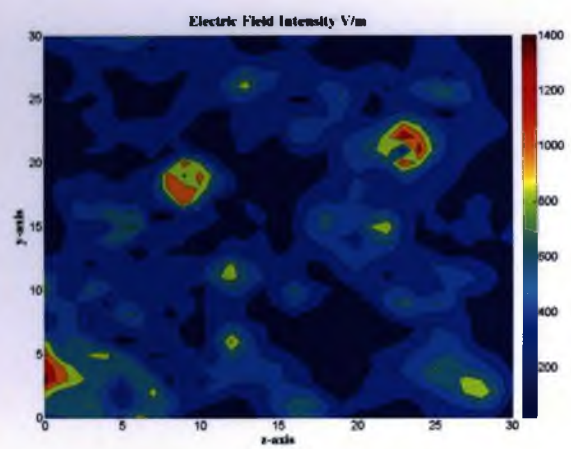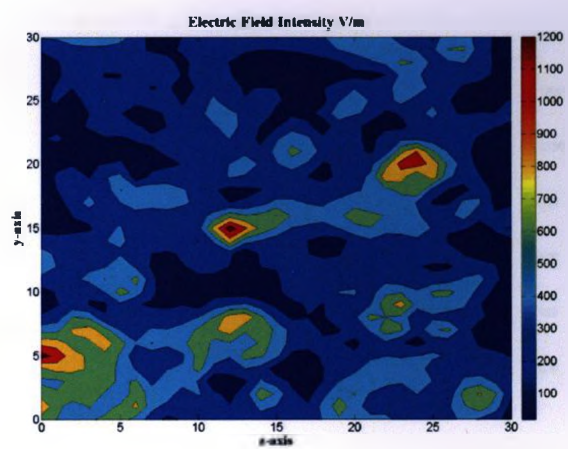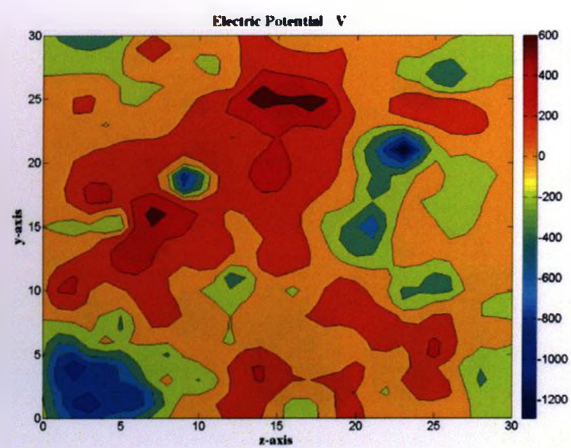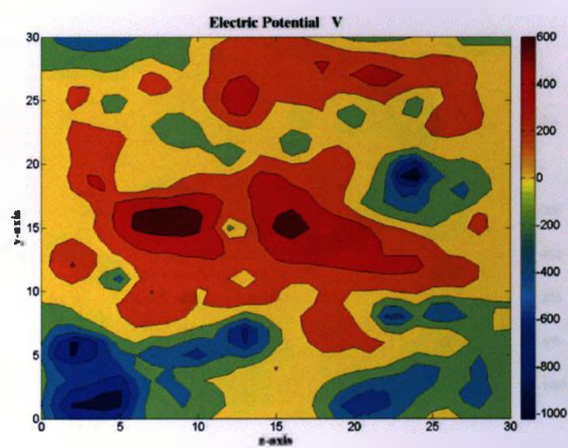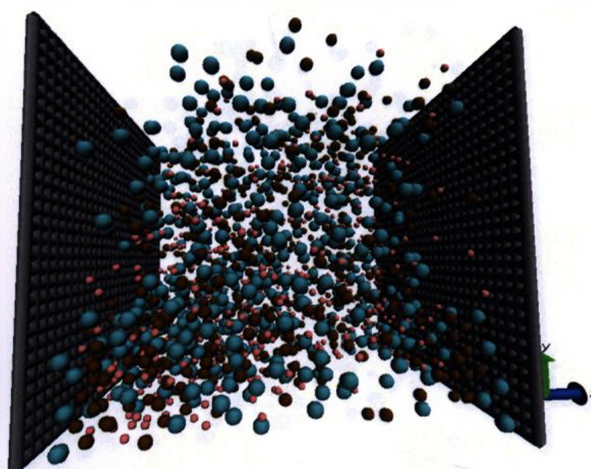
384 ms:
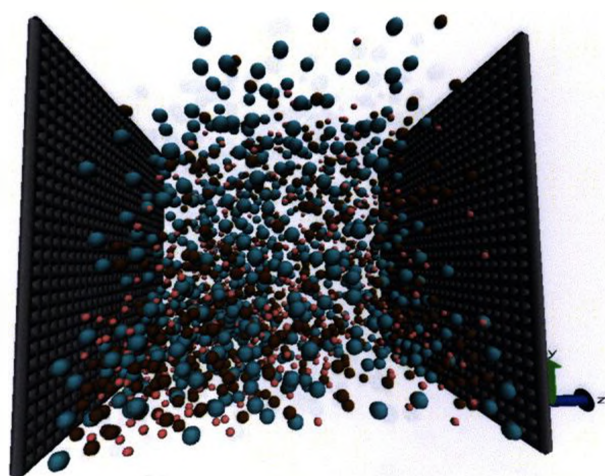
408 ms:
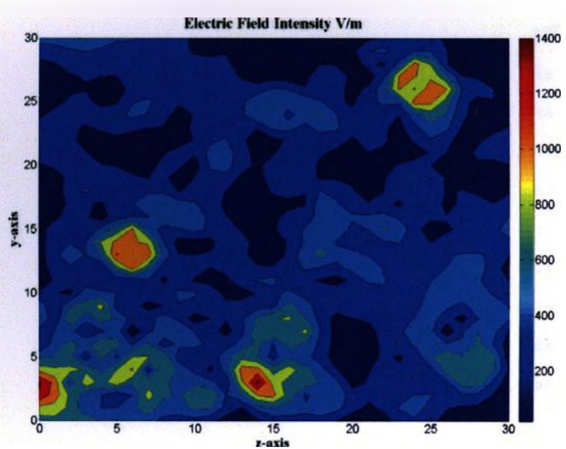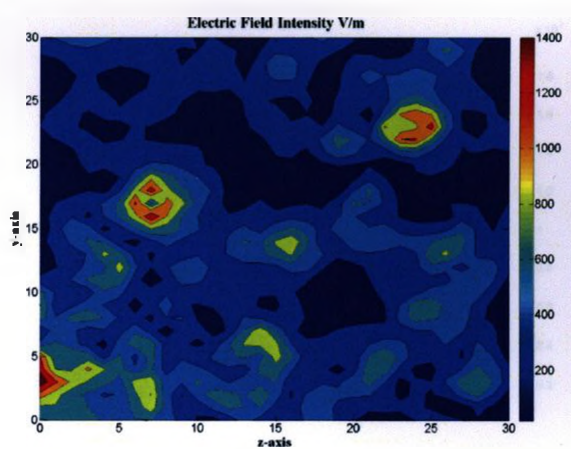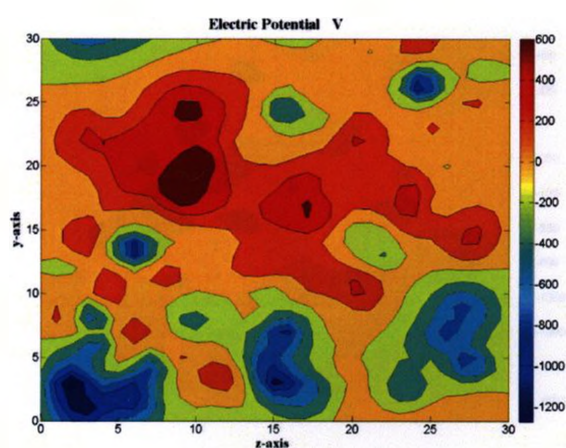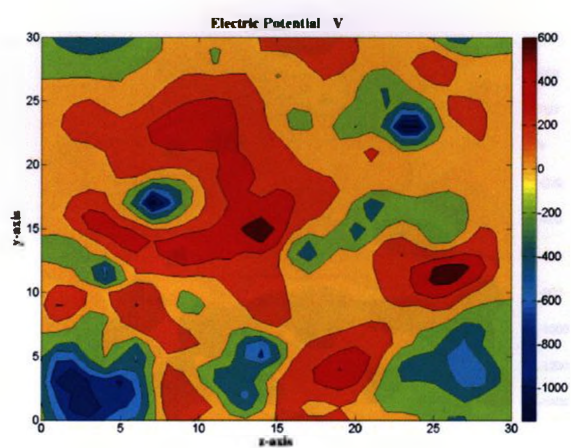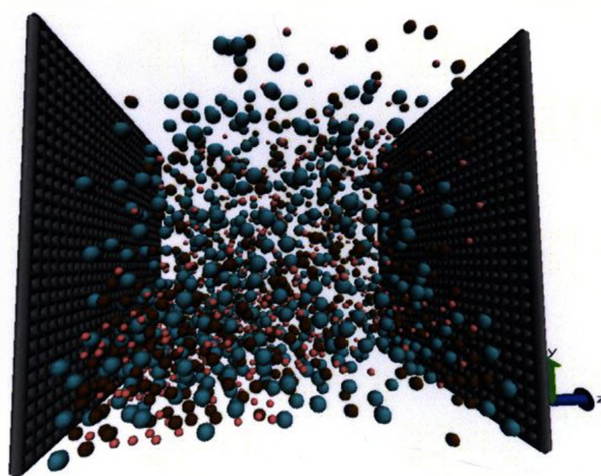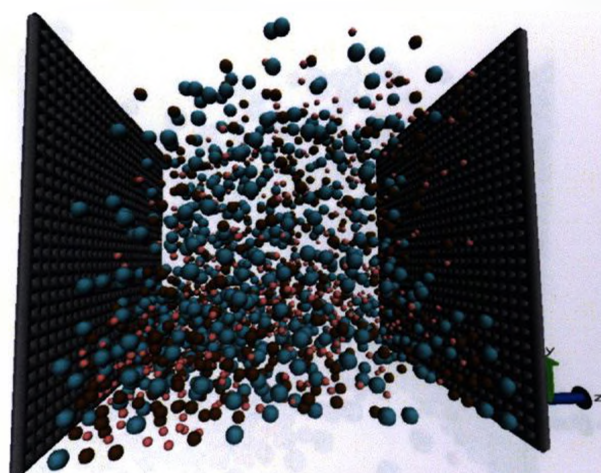
432 ms: **456 ms:**
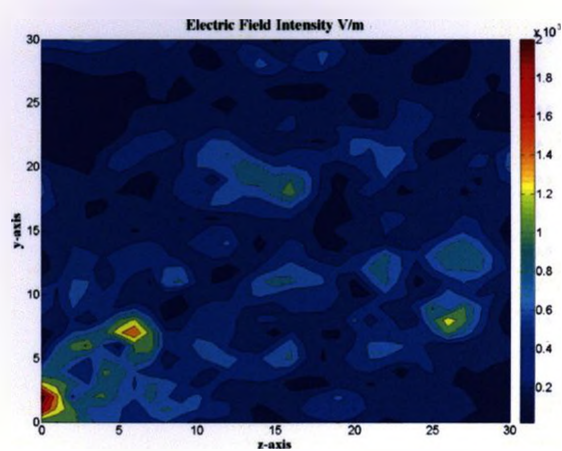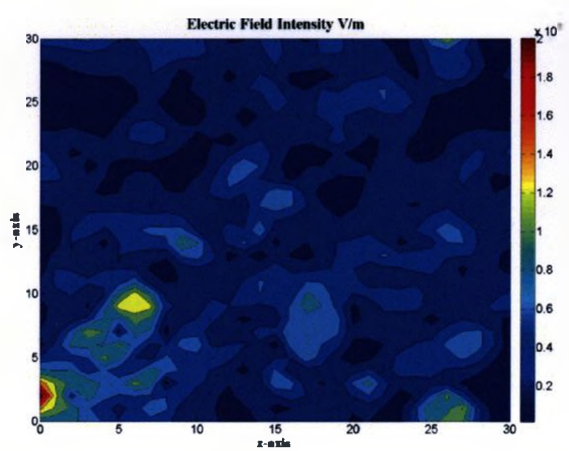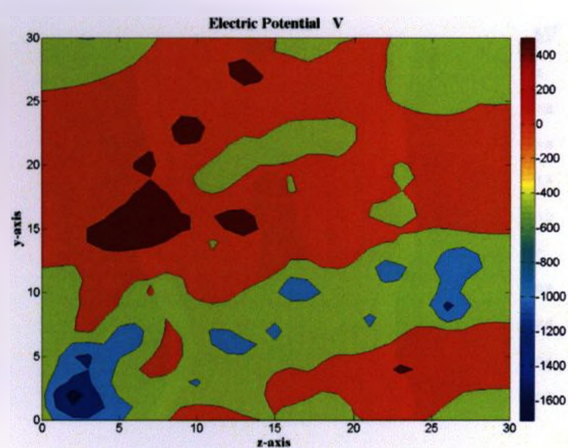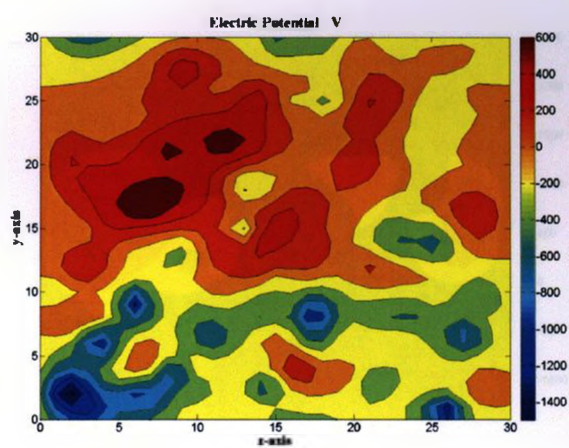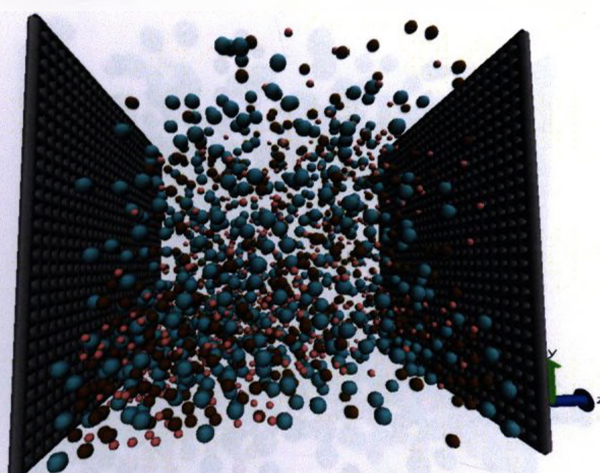
480 ms (particle injection): **504 ms:**
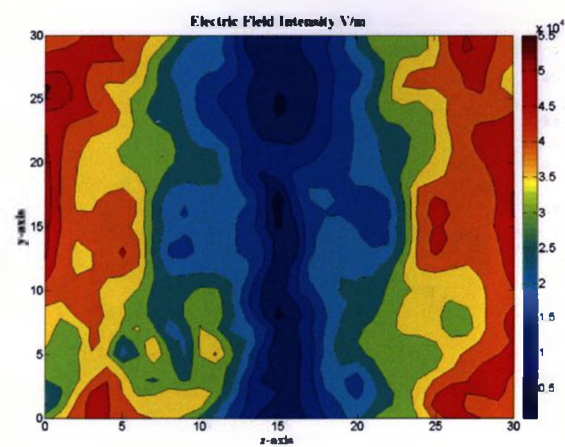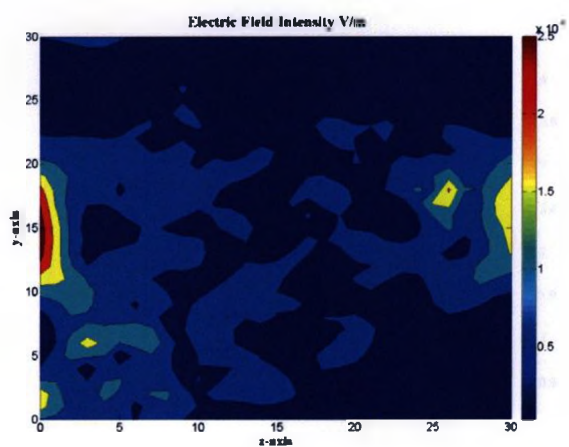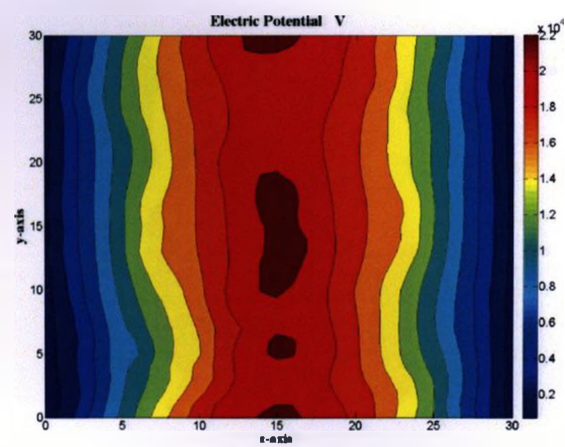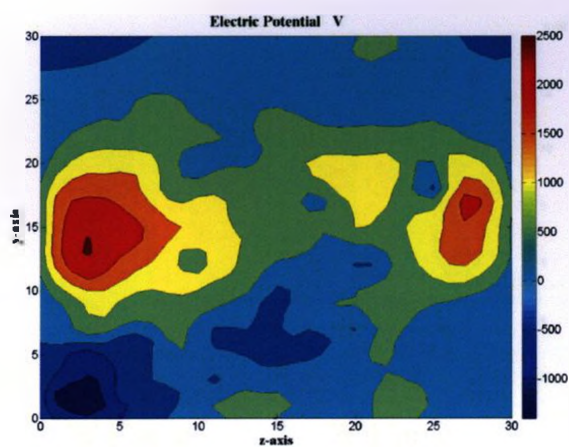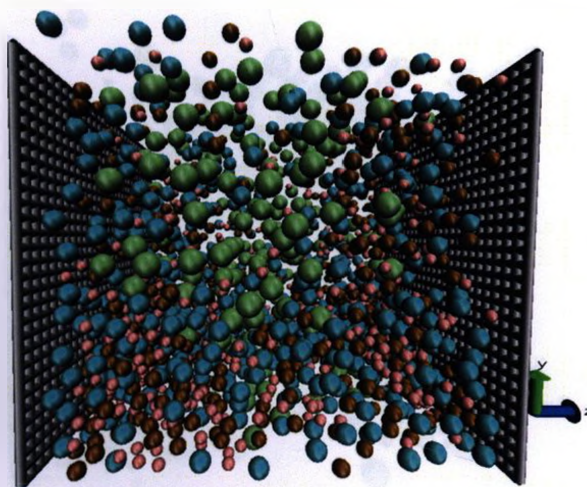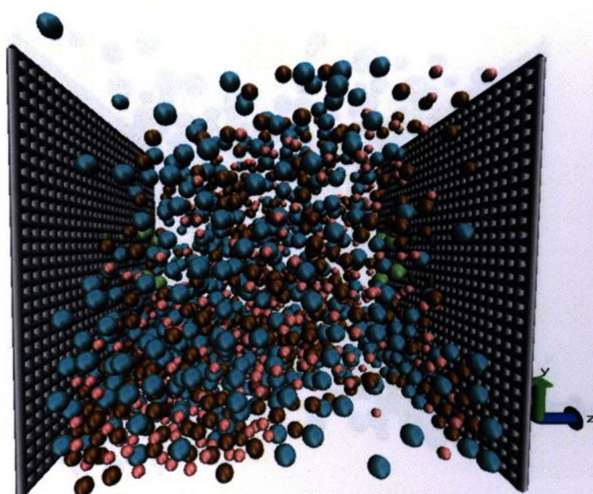
528 ms:

552 ms:
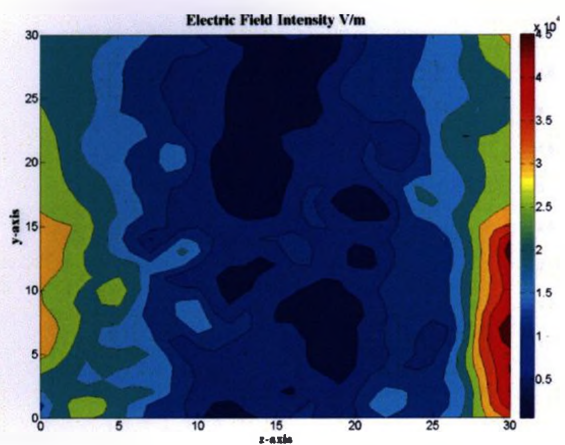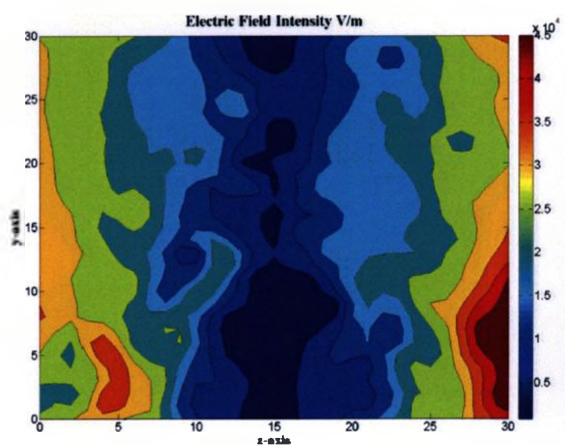
576 ms:

600 ms:

624 ms:

648 ms:

672 ms:

696 ms:

Electric Potential V

Electric Potential V

Electric Field Intensity V/m

Electric Field Intensity V/m
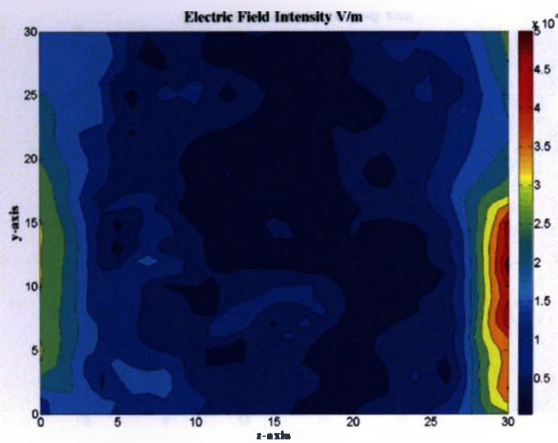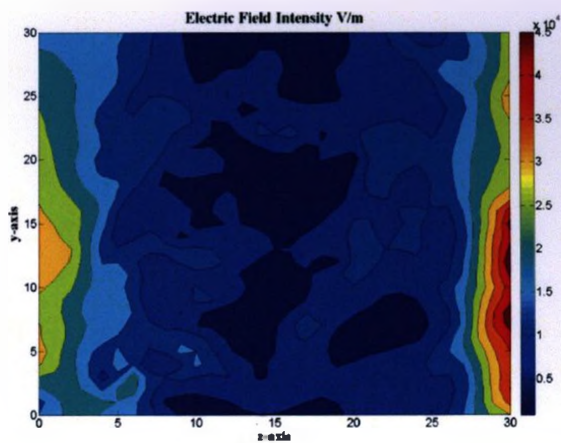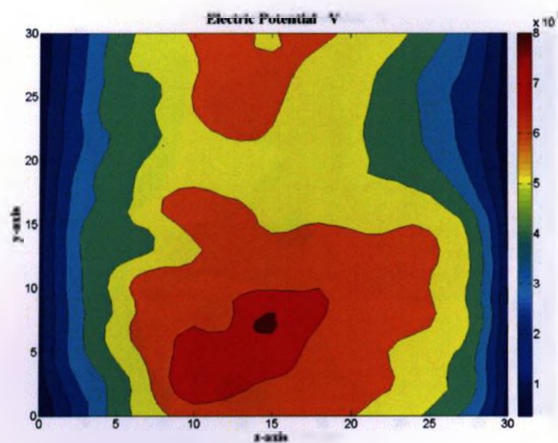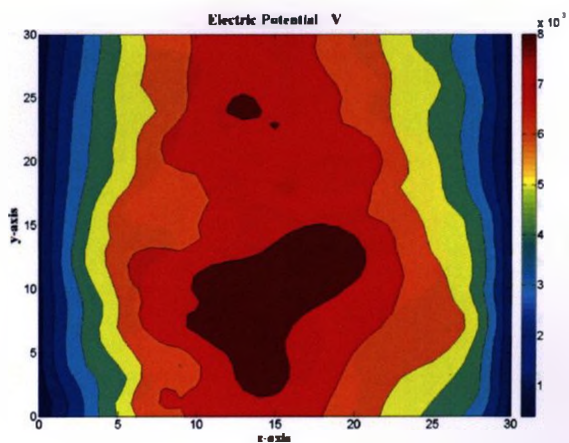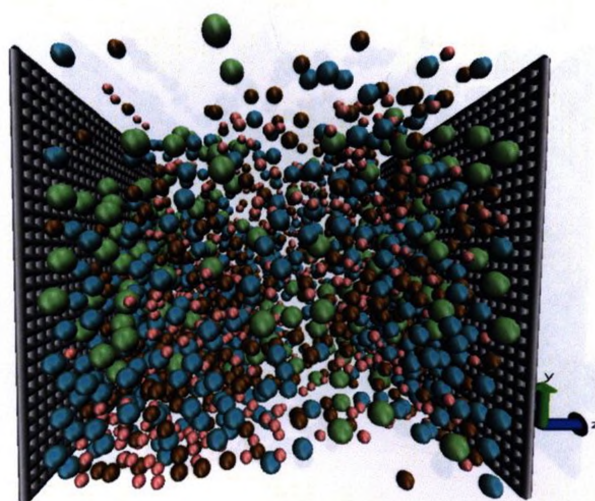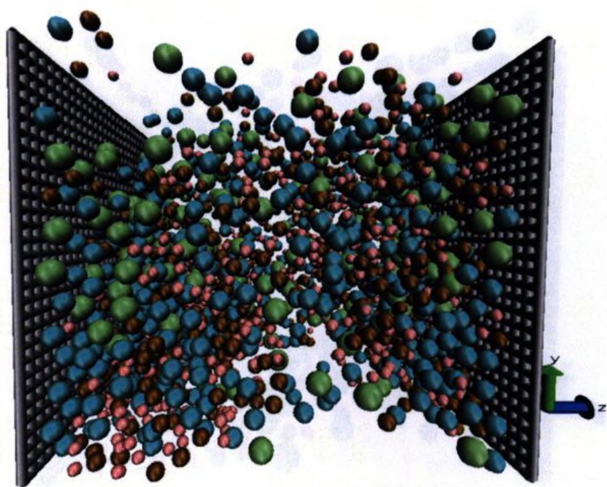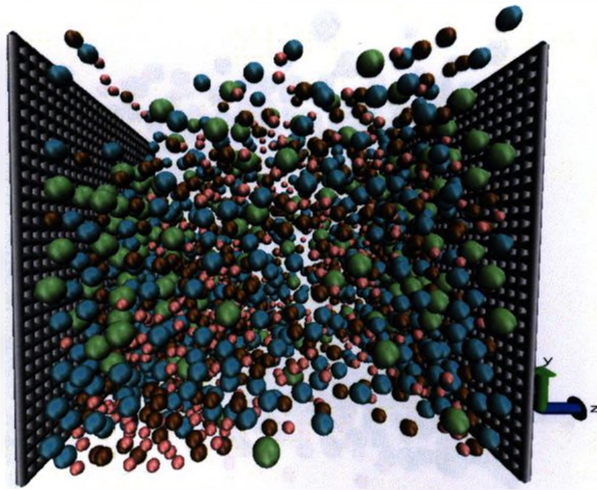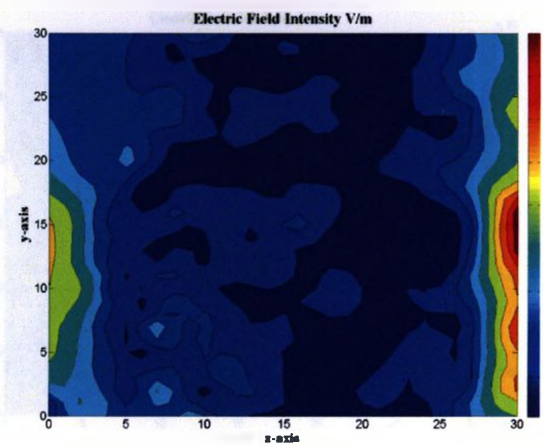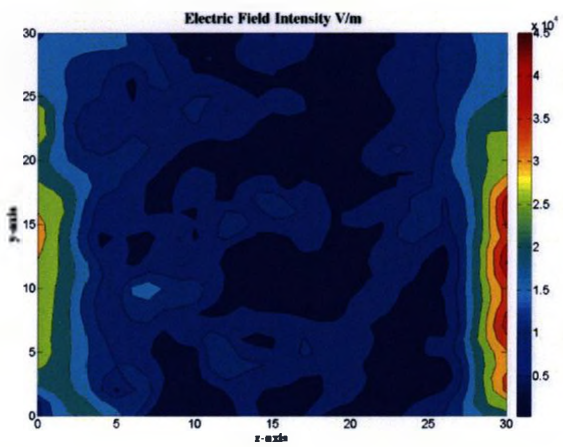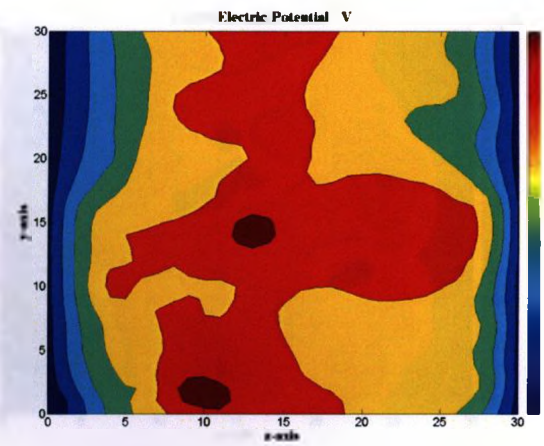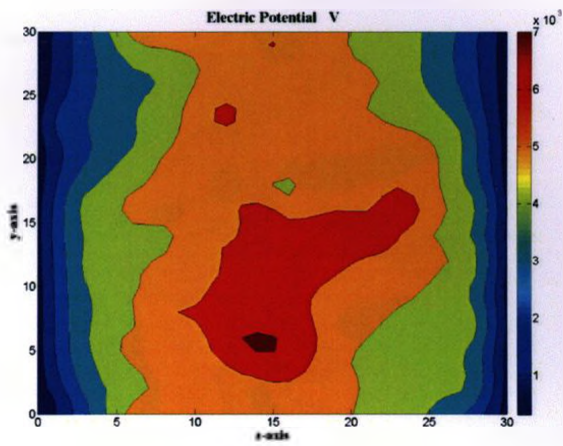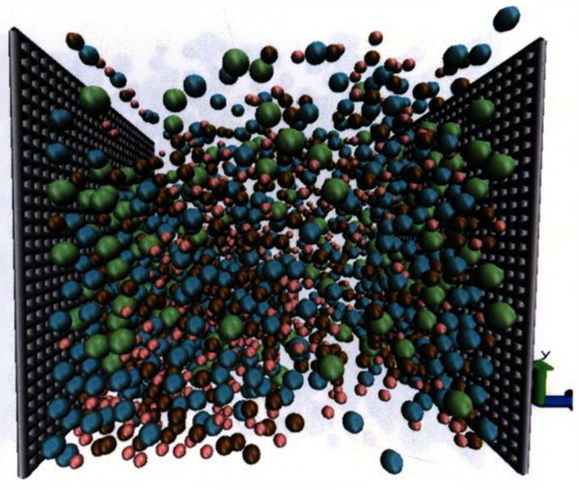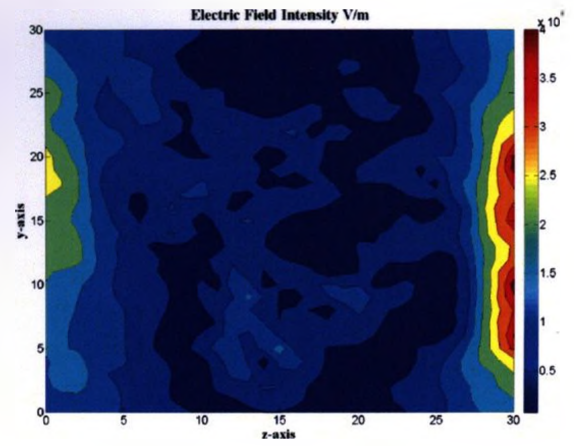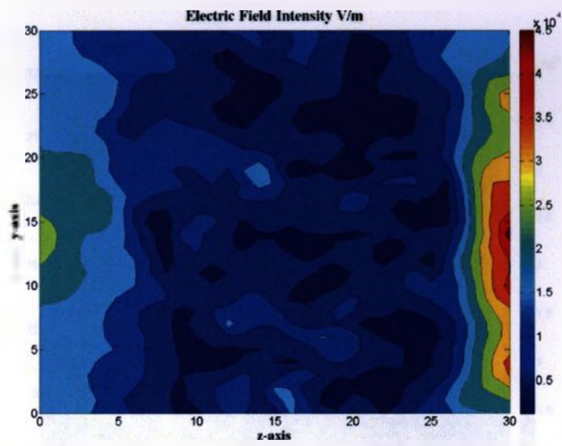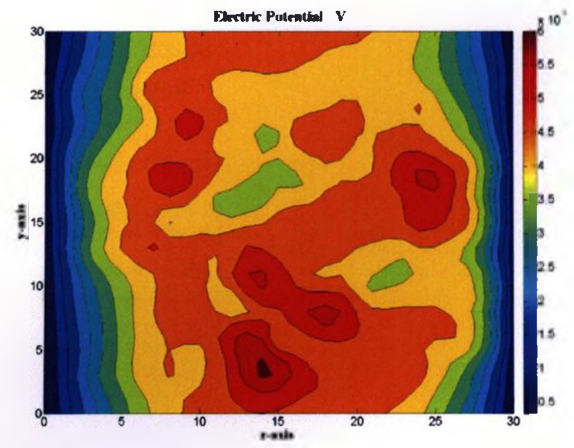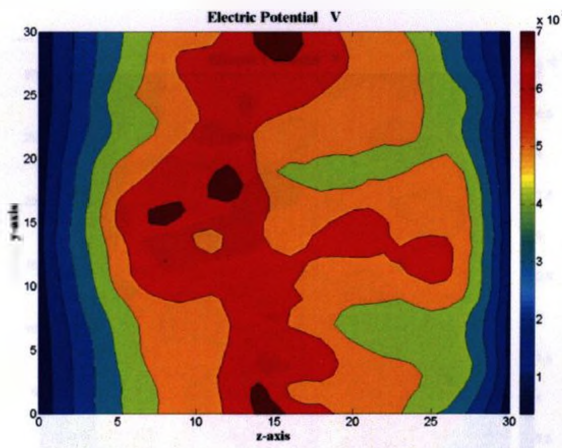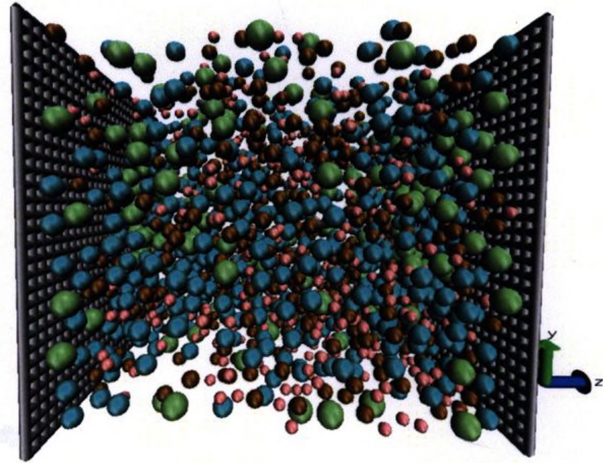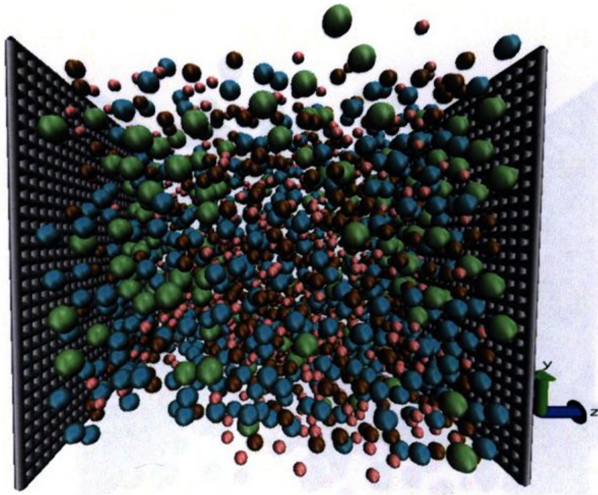
720 ms:
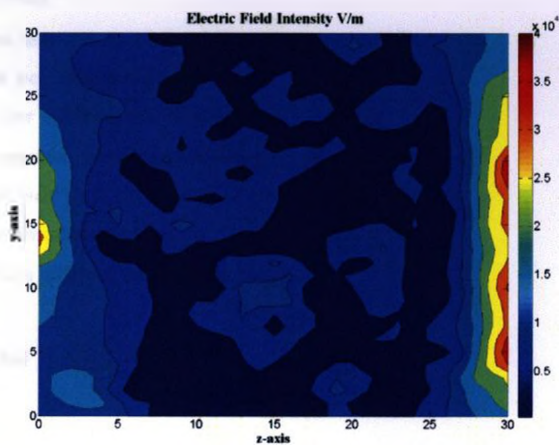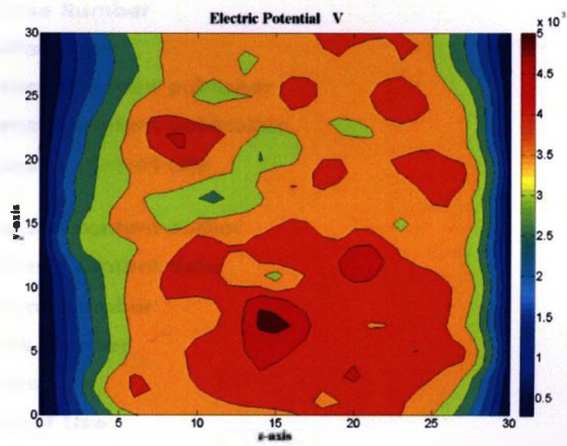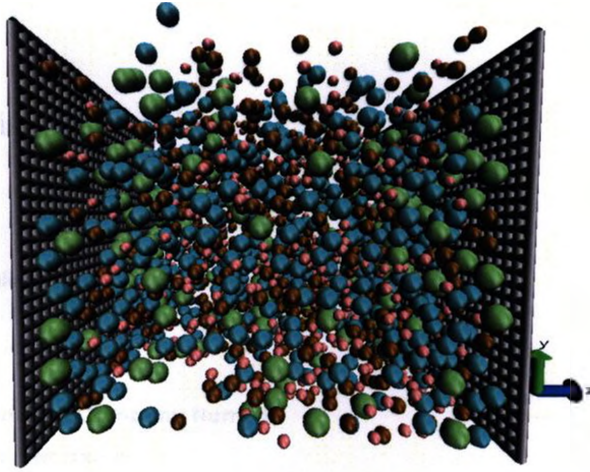
Appendix 2

Permissions

Permission to use Figure 2.1:

Supplier	Elsevier Limited The Boulevard, Langford Lane Kidlington, Oxford, OX5 1GB, UK
Registered Company Number	1982084
Customer name	mario a Nunez
Customer address	552 Plattès Lane apt.21 london, ON N6G 3A9
License Number	2312690570812
License date	Nov 19, 2009
Licensed content publisher	Elsevier
Licensed content publication	Journal of Electrostatics
Licensed content title	Contact charging between insulators
Licensed content author	G. S. P. Castle
Licensed content date	June 1997
Volume number	40-41
Issue number	
Pages	8
Type of Use	Thesis / Dissertation
Portion	Figures/table/illustration /abstracts
Portion Quantity	1
Format	Print
You are an author of the Elsevier article	No
Are you translating?	No
Order Reference Number	
Expected publication date	Dec 2009
Elsevier VAT number	GB 494 6272 12
Permissions price	0.00 USD
Value added tax 0.0%	0.00 USD
Total	0.00 USD

Permission to use Figure 5.3 and Figure 5.4 [37]:

Supplier	Elsevier Limited The Boulevard, Langford Lane Kidlington, Oxford, OX5 1GB, UK
Registered Company Number	1982084
Customer name	mario a Nunez
Customer address	552 Plattès Lane apt.21 london, ON N6G 3A9
License Number	2312630418543
License date	Nov 19, 2009
Licensed content publisher	Elsevier
Licensed content publication	Journal of Electrostatics
Licensed content title	Particle dynamics simulations of triboelectric charging in granular insulator systems
Licensed content author	Nathan Duff and Daniel J. Lacks
Licensed content date	January 2008
Volume number	66
Issue number	1-2
Pages	7
Type of Use	Thesis / Dissertation
Portion	Figures/table/illustration /abstracts
Portion Quantity	2
Format	Print
You are an author of the Elsevier article	No
Are you translating?	No
Order Reference Number	
Expected publication date	Dec 2009
Elsevier VAT number	GB 494 6272 12
Permissions price	0.00 USD

References

[1] D.S. Schmidt, A.S. Schmidt, J.D. Dent,"Electrostatic force on saltating sand", Journal of Geophysical Research-Atmospheres, vol. 103, p. 8997, (1998)

[2] W.M. Farrell, M.L. Kaiser, M.D. Desch, J.G. Houser, and S.A. Cummer, "Detecting electrical activity from Martian dust storms", Journal of Geophysical, vol. 104, No. 2, pp. 3795-3801, (1999)

[3] J. Latham, "The electrification of snowstorms and sandstorms", Quarterly Journal of the Royal Meteorological Society, vol. 90, p. 91, (1964)

[4] R. Greeley, J.D. Iversen, "Wind as a geological proceedings on Earth, Mars, Venus and Titan", (Cambridge University Press, London), (1985)

[5] R. S. Anderson, and B. Hallet, "Sediment transport by wind: toward a general model", Bulletin of the Geological Society of America, vol. 97, p. 523, (1986)

[6] G.D. Freier, "The electric field of a large dust devil", Journal of Geophysical Research, vol. 65, p. 3504, (1960)

[7] R. Greeley, R.A. Leach, "A preliminary assessment of the effects of electrostatics on aeolian process", Rep. Planet Geo. Program, NASA TM 79729, pp. 236-237, (1978)

[8] J.D. Iversen, "Drifting-snow similitude-transport-rate and roughness modeling",

Journal of Glaciology, vol. 26, Issue 94, pp. 393-403, (1980)

[9] D. D. Sentman, "Electrostatic fields in a dusty Martian environment", Ames Research

Center, Sand and Dust on Mars, pp. 53, (1991)

[10] M.R. James, L. Wilson, S.J. Lane, J.S. Gilbert, T.A. Mather, R.G. Harrison and R.S.

Martin, "Electrical charging of volcanic plumes", Space Science Review, vol. 137,

pp. 399-418, (2008)

[11] J. Lowell, A.C. Rose-Innes, "Contact Electrification", Advances in Physics, vol.

29, issue 6, pp. 947-1023, (1980)

[12] J.A. Medley, "The electrostatic charging of some polymers by mercury", British

Journal of Applied Physics, vol. 4, pp. S28-S29, (1953)

[13] J.A. Cross, "Electrostatics Principles, Problems and Applications", Bristol, England,

Adam Hilger, (1987)

[14] D.K. Davies, D.K., "Static Electrification", Institute of Physics Conference Series

No.4, p. 29, (1967)

[15] J. Latham, "The electrification of snowstorms and sandstorms", Journal of

Meteorology, vol. 90, Issue 383, pp 91-95, (2006)

[16] H.F. Eden, B. Vonnegut, "Electrical breakdown caused by dust motion in low-pressure atmospheres: Considerations for Mars", Journal of Science, vol. 180, No. 4089, pp. 962-963, (1973)

[17] A.S. Mills, "Dust clouds and frictional generation of glow discharges on Mars", Nature, vol. 268, p. 614, (1977)

[18] D. Boland, Q.A.W. Al-Salim, D. Geldart, "Static electrification of fluidized beds" , Chemical Engineering Science, vol. 24, p. 1389, (1969)

[19] C.E. Krauss, M. Horanyi, S. Robertson, "Experimental evidence for electrostatic discharging of dust near the surface of Mars", New Journal of Physics, vol. 5, p. 70, (2003)

[20] W.D. Crozier, "The electric field of a New Mexico dust devil", Journal of Geophysical Research, vol. 69, pp. 5427-5429, (1964)

[21] C.D. Stow, "Dust and sand storm electrification", Rep. Program of Physics, vol. 32, p. 1, (1969)

[22] A.I.I. Ette, "The effect of the Harmattan dust on atmospheric electric parameters", Journal of Atmospheric and Terrestrial Physics, vol. 33, p. 295, (1971)

[23] W.M. Farrell, P.H. Smith, G.T. Delory, G.B. Hillard, J.R. Marshall, D. Catling, M.

Hecht, D.M. Tratt, N. Renno, M.D. Desch, S.A. Cummer, J.G. Houser, B. Johnson, "Electric and magnetic signatures of dust devils from the 2000-2001 MATADOR desert tests", Journal of Geophysical Research, vol. 109, E03004, (2004)

[24] T. Miura, T. Koyaguchi, Y. Tanaka, "Measurements of electric charge distribution in volcanic plumes at Sakurajima Volcano, Japan" Bulletin of Volcanology, vol. 64, pp. 75-93, (2002)

[25] P. Cartwright, S. Singh, A.G. Bailey, L.J. Rose, "Electrostatic charging characteristics of polyethylene powder during pneumatic conveying", IEEE Transactions Industrial Applications, vol. IA–21 , pp. 541-546, (1985)

[26] F.S. Ali, I.I. Inculet, "Charge exchange model of a disperse system of spherical powder particles", Journal of Electrostatics, vol. 45, p.139, (1998)

[27] H. Zhao, G.S.P. Castle, I.I. Inculet, "The measurement of bipolar charge in polydisperse powders using a vertical array of Faraday pail sensors", Journal of Electrostatics, vol. 55, issue 3-4, pp. 261-278, (2002)

[28] H. Zhao, G.S.P. Castle, I.I. Inculet, A.G. Bailey, "Bipolar charging of poly-disperse polymer powders in fluidized beds", IEEE Transactions Industrial Applications, vol. 39, issue 3, pp. 612-618, (2003)

[29] S. Trigwell, N. Grable, C.U. Yurteri, R. Sharma, M.K. Mazumder, "Effects of surface

properties on the tribocharging characteristics of polymer powder as applied to industrial processes", IEEE Transactions Industrial Applications, vol. 39, pp.79-86, (2003)

[30] I.I. Inculet, G.S.P. Castle, G. Aartsen, "Generation of bipolar electric fields during industrial handling of powders", Chemical Engineering Science, vol. 61, issue. 7, pp. 2249-2253 (2006)

[31] A.A. Sickafoose, J.E. Colwell, M. Horanyi, S. Robertson, "Experimental investigations on photoelectric and triboelectric charging of dust", Journal of Geophysical Research., vol. 106, NO. A5, pp. 8343-8356, (2001)

[32] X.J. Zheng, N. Huang, Y.-H Zhou, "Laboratory measurement of electrification of wind-blown sands and simulation of its effect on sand saltation movement", Journal of Geophysical Research, vol. 108, pp. 4322, (2003)

[33] L.B. Schein, LaHa., D. Novotny, "Theory of insulator charging", Physics Letters A, vol. 167, pp. 7983, (1992)

[34] L.B. Schein, "Theory of Toner Charging", Journal of Imaging Science and Technology, vol. 37, pp. 1-4, (1993)

[35] L.B. Schein, "Electrophotography and development physics", Germany, Springer-Verlag, Berlin Heidelberg, pp. 63-92, (1988)

[36] S.L. Soo, "Direct Energy Conversion", New Jersey, USA , Prentice-Hall Inc.,

pp.75-77, (1968)

[37] N. Duff, D.J. Lacks, J., "Particle dynamics simulations of triboelectric charging in

granular insulator systems" Journal of Electrostatics, vol. 66, pp.51-57, (2008)

[38] William J. Kaufmann y Larry L. Smarr, "Supercomputing and the Transformation of

Science", Scientific American Library, New York, (1993)

[39] R.W. Hockney, J.W. Eastwood, "Computer simulation using particles", Taylor &

Francis publishers, (1998)

[40] N. Metropolis, A. W. Rosenbluth, M. N. Rosenbluth, A. H. Teller, and E. Teller,

"Equation of state calculations by fast computing machines", Journal of Chemical

Physics, vol. 21, No. 6, (1953)

[41] J. Kuipers, F. Van Beckum , W. Van Swaaij, "A numerical model of gas-fluidized

beds", Chemical Engineering Science, vol. 47, pp. 1913-1924, (1992)

[42] T.E. Tezduyar, "Finite element methods for flow problems with moving boundaries

and interfaces", Archives of Computational Methods in Engineering, vol. 8, pp. 83-

130, (2001)

[43] K.-J. Bathe, H. Zhang, "Finite element developments for general fluid flows with structural interactions", International Journal for Numerical Methods in Engineering, vol.60, pp. 213-232, (2004)

[44] S. Chen, G. Doolen, "Lattice-Boltzmann method for fluid flows", Annual Review Fluid Mechanics, vol. 30, pp. 329-364, (1998)

[45] A. Ladd, R. Verberg, "Lattice-Boltzmann simulations of particle-fluid suspensions", Journal of Statistical Physics, vol. 104(5/6), pp. 1189-1201, (2001)

[46] A. Ladd, "Numerical simulations of fluid particulate suspensions via a discretized Boltzmann equation(Parts I & II)", Journal of Fluid Mechanics, vol. 271, pp. 285-339, (1994)

[47] Z. Chen, G. Huan, Y. Ma, "Computational Methods for Multiphase Flows in Porous Media", Society for Industrial and Applied Mathematics publisher, Texas, USA, (2006)

[48] G. Makov, M.C. Payne, "Periodic boundary conditions in ab initio calculations", Physics Review B, vol. 51, pp. 4014-4022, (1995)

[49] S. Succi, "The Lattice Boltzmann equation for fluid dynamics and beyond", Clarendon Press, Oxford, (2001)

[50] S. Chen, D. Martinez, R. Mei, "On boundary conditions in lattice Boltzmann methods", Physics of Fluids, vol. 8, pp. 2527-2536, (1996)

[51] F.J. Higuera, J. Jimenez, "Boltzmann Approach to Lattice Gas Simulations", Europhysics Letters, vol. 9, pp. 663-668, (1989)

[52] Y. H. Qian, D. D'Humieres, P. Lallemand, "Lattice BGK Models for Navier-Stokes Equation", Europhysics Letters, vol. 17(6), pp. 479-484, (1992)

[53] P.L. Bhatnagar, E.P. Gross, M. Krook, "A model for Collision Processes in Gases. I. Small Amplitude Processes in Charged and Neutral One-Component systems", Physical Review, vol. 94, pp. 511-525, (1954)

[54] X. He, L. Luo, "Theory of lattice Boltzmann method: From the Boltzmann equation to the lattice Boltzmann", Physical Review E, vol. 56, pp. 6811-6817, (1997)

[55] D.A. Wolf-Gladrov, "Lattice-gas cellular automata and lattice Boltzmann models: an introduction", Springer publisher, Berlin, (2000)

[56] B.J. Alder, T.E. Wainwright, "Phase Transition for a Hard Sphere System", Journal of Chemical Physics, vol. 27, p. 1208, (1957)

[57] S.J. Zhou, D.M. Beazley, P.S. Lomdahl, B.L. Holian, "Large-Scale Molecular Dynamics Simulations of three-Dimensional Ductile Failure", Journal of Physics.

Review Letter, vol. 78, pp. 479-482, (1997)

[58] J. K. Johnson, J.A. Zollweg, K.E. Gubbins, "The Lennard-Jones equation of state

Revisited", Molecular Physics, vol. 78, Issue 3, pp. 591-618, (1993)

[59] J.J. Nicolas, K.E. Gubbins, W.B. Streett, D.J. Tildesley, "Equation of state for the

Lennard-Jones fluid", Molecular Physics, vol. 37, Issue 5, pp. 1429-

1454, (1979)

[60] C. J. Smith, C Denniston, "Lattice Boltzmann simulations of colloidal

Aerodynamics", Under consideration for publication in Journal Fluid Mechanics,

(2007)

[61] Q. Ye, T. Streingleder, A. Scheibe and J. Domnick, "Numerical simulation of the

electrostatic powder coating process with a corona spray gun", Journal of

Electrostatics, vol. 54, issue 2, pp. 189-205, (2002)

[62] U. Shah, C. Zhang, J. Zhu, F. Wang, R. Martinuzzi, "Validation of a numerical model

for the simulation of an electrostatic powder coating process", International Journal

of Multiphase Flow , vol. 33, issue 5, pp. 557-573, (2007)

[63] S. Zhao, G.S.P. Castle and K. Adamiak, "Factors affecting deposition in electrostatic

pesticide spraying", Journal of Electrostatics, vol. 66, issues 11-12, pp. 594-601,

(2008)

[64] S. Yousuf, S.A. Barringer, "Modeling non-electrostatic and electrostatic powder coating", Journal of Food Engineering, vol. 83, pp. 550-561, (2007)

[65] H. Watanabe, M. Ghadiri, T. Matsuyama, Yu. Long, K. G. Pitt, H. Maruyama, S. Matsukasa, H.Masuda, "Triboelectrification of pharmaceutical powders by particle Impact", International Journal of Pharmaceutics, vol. 334, pp. 149-155, (2007)

[66] J. Lowell, W.S. Truscott, "Triboelectrification of identical insulators: II Theory and further experiments", Journal of Physics D: Applied Physics, vol. 19, pp. 1281-1298, (1986)

[67] B.L. Buzbee, G.H. Golub, C.W. Nielson, "On direct methods for solving poisson's equations", Journal of Numerical Analysis, vol. 7, No. 4, pp. 627-656, (1970)

[68] R.W. Hockney , "A fast solution of Poisson's equation using Fourier analysis", Journal of the Association for Computing Machinery, vol. 12, No. 1, pp. 95-113, (1965)

[69] M. Frigo, S. G. Jhonson, "The design and implementation of FFTW3", IEEE Transactions, vol. 93, No. 2, pp. 216-231, (2005)

[70] G. Mesa, E. Dobado-Fuentes, J.J. Saenz, "Image charge method for electrostatic calculations in field-emission diodes", Journal of Applied Physics, vol. 79, No. 1, pp. 38-44, (1996)

[71] G. Filou, I.I Inculet, M.A. Bergougnou, "Study of the fall off of electrically

charged Rilsan powder coatings during the curing operations", Applied Electrostatic

Research Centre, (2004)